Biophysical cues to enhance neuronal differentiation

by

Sabrina Mattiassi

A thesis
presented to the University of Waterloo
in the fulfillment of the
thesis requirements for the degree of
Master of Applied Science
in
Chemical Engineering

Waterloo, Ontario, Canada, 2021

AUTHOR'S DECLARATION

This thesis consists of material all of which I authored or co-authored: see Statement of Contributions included in the thesis. This is a true copy of the thesis, including any required final revisions, as accepted by my examiners.

I understand that my thesis may be made electronically available to the public.

STATEMENT OF CONTRIBUTIONS

Sections 1.1 and 1.2 are from a review paper I co-authored with Deepak Jain.[1] Chapter 2 is co-authored with Dr. Mohammed Rizwan and Dr. Aung Moe Zaw from the Department of Chemical Engineering, University of Waterloo, and Dr. Chris Grigsby from the Department of Biomedical Engineering, Columbia University. Dr. Rizwan and Dr. Grigbsy helped to prepare samples, culture cells and collect data regarding the effect of topography on pABOL polyplex GFP transfection efficiency (Figure 2.2), and screening of topographies to determine if any can enhance neuronal reprogramming (Figure 2.3). Dr. Zaw helped to perform patch clamp recording (Figure 2.6). The mouse neural progenitor cells and human neural progenitor cells used in Chapters 3 and 4 were derived from a gift from Dr. Eyleen Goh from The National Neuroscience Institute, Tan Tock Seng Hospital, Singapore.

ABSTRACT

Biophysical cues are an important tool for neuronal tissue engineering and regenerative medicine. Cues such as topography and stiffness have been shown to enhance lineage and non-lineage based neuronal differentiation by increasing the rates of differentiation and maturation and by increasing the fraction of cells that commit to the neuronal lineage. Despite the breadth of studies showing their effectiveness, there is a paucity of information regarding how they affect new neuronal generation techniques and how these cues may interact with one another. The aim of this thesis is to investigate these gaps. Doing so, it has been found that hierarchical topographies can significantly enhance non-viral direct neuronal reprogramming of fibroblast. Synergistic effects observed on hierarchical patterns show that they can both increase the fraction of cells that commit to the neuronal lineage and improve subsequent maturation. Second, we have developed a platform to study the combined effects of stiffness and topography on lineage-based differentiation over an extended period. Using an existing polyacrylamide-based platform we have used carbodiimide crosslinking with charged polypeptide-intermediates to stably bound laminin to the surface. Both mouse and human neural progenitor cells and their derived neurons can adhere to these surfaces for extended periods of time. Third, using this developed platform we found that the effects of stiffness and topography on neuronal differentiation are intertwined. Their interaction seems to provide a moderating effect for each of the cues and suggests that the effect of topography on lineage commitment and maturation varies depending on the stiffness of the substrate.

ACKNOWLEDGMENTS

I would like to thank my supervisor, Associate Professor Evelyn K.F. Yim, for her guidance, support and patience. Prof. Yim afforded me great freedom for self-discovery and development and also always helped to guide my problem solving with her expert insight. Her positive attitude and ceaseless encouragement helped carry me through even the most difficult research challenges and gave me the confidence to try new things. I am very grateful for all that I have learned and all the opportunities I have been afforded in the Yim Lab.

I would like to thank Assistant Professor Valerie Ward and Assistant Professor Hamed Shahsavan for their indispensable feedback and insight which helped to improve the contents of this thesis.

I would like to thank all my fellow members of the Yim Lab: Ms. Sarah W. Chan, Ms. YeJin Jeong, Ms. Yuan Yao, Mr. Deepak Jain, Ms. Linan Cui, Ms. Fan Feng, Mr. Wesley Luu, Ms. Laura Edmonds, Mr. John Tse, Dr. Rizwan Muhammed, and Dr. Aung Moe Zaw. Special thanks to Ms. Grace Pohan, who was my mentor when I started in the Yim Lab. You have all been a pleasure to work alongside. Your help and friendship have made the many hours I spent in the lab more enjoyable. I wish you all the best in all your endeavours.

Lastly, I would like to thank my parents, my grandmother, family, Carol, Virgina, Fred, and Mary, and my wonderful friends, for your tireless support. In times of joy, hardship, and everything in between, you have always been there for me. I could not have done this without you!

For my mom and dad who have always encouraged me,

“A provà no l’e peciat.”

TABLE OF CONTENTS

LIST OF FIGURES

LIST OF TABLES

LIST OF ABBREVIATIONS

ACA – N-acryloyl-6-aminocaproic acid

AFM – atomic force microscopy

ANOVA – analysis of variance

AP – action potential

BAM – Brn2, Ascl1, Myt1l transfection factors

CNS – central nervous system

DPSC – dental pulp stem cell

EDC – 1-Ethyl-3-(3-dimethylaminopropyl)carbodiimide

ECM – extracellular matrix

ESC – embryonic stem cell

FGF – fibroblastic growth factor

EGF – epidermal growth factor

GFAP – glial fibrillary acidic protein

GFP – green fluorescent protein

hNPC – human neural progenitor cell

iN – induced neuron

iPSC – induced pluripotent stem cell

MAP2 – microtubule-associated protein 2

MARC – multiarchitecture array

mNPC – mouse primary neural progenitor cell

MSC – mesenchymal stem cell

NHS – N-Hydroxysuccinimide

NSC/NPC – neural stem cell/neural progenitor cell

PAA – polyacrylamide

pABOL – poly(N,N-cystaminebisacrylamide- 4-amino-1-butanol)

PCR – polymerase chain reaction

PDMS – polydimethylsiloxane

PET – polyethylene terephthalate

PLL – poly-l-lysine

PLO – poly-l-ornithine

PMEF – primary mouse embryonic fibroblasts

PNS – peripheral nervous system

SD – standard deviation

Syn1 – synapsin I

TUJ1 – beta III tubulin

Unp – unpatterened

LIST OF SYMBOLS

2uG – 2 x 2 x 2 μm gratings

5uG – 5 x 5 x 5 μm gratings

2uG – 10 x 10 x 10 μm gratings

N_i – fraction of all cells induced to the neuronal lineage, measured using TUJ1, on pattern i

r – Spearman correlation coefficient

R_i – reprogramming efficiency, fraction of transfected cells that express BAM, on pattern i

T_i – transfection efficiency, measured using GFP, on pattern i

T*S – interaction of stiffness and topography

CHAPTER

1 Introduction and Literature Review

1.1. Cell Types of the Nervous System

The human nervous system can be broadly separated into two principal components called the central nervous system (CNS) and the peripheral nervous system (PNS). The central nervous system is the integrative control center comprised of the brain and the spinal cord. The peripheral nervous system links the CNS and all the other tissues of the body allowing them to communicate. The nervous system is made up of two broad categories of cells: neurons and glial cells. Neurons are primary cells of the nervous system as they are responsible for the main functions of the nervous system. They respond to stimuli and transmit electrical signals via synapses. Glial cells are support cells, helping to anchor, nourish, and insulate neurons, control the chemical environment, influence neuronal functioning, remove debris, and protect neurons from pathogens. The glial cells of the CNS include astrocytes, oligodendrocytes, ependymal cells and microglia. They constitute the majority of the cells in the CNS.[2, 3] The glial cells of the PNS include Schwann cells which perform similar functions to oligodendrocytes and satellite cells, which perform similar functions to astrocytes. [2]

Morphologically glial cells and neurons are similar in that they both tend to have a central cell body from which thin, branched processes extend. The exception being ependymal cells which are more squamous in shape. Glial cells' processes also tend to be more isotropic than neuronal processes with their processes extending outward in all directions. Astrocytes are dense with processes that radiate out of their star-shaped cell body. Microglial cells have an oval-shaped cell body with many long, thin, highly-branched processes extending. Oligodendrocytes have fewer processes with less branching and very round central cell body.[2, 3] Neuron morphology varies widely depending on the specialization of the neuron. In general, all neurons have a spherical cell body with diameters ranging from 5 to 140 μm. From this cell body extends an axon and, depending on the neuronal type, one or more dendrites may also extend. [2]

In cell culture, or histology of neural tissue, antibody staining is often used to distinguish glial cells from neurons, and classify neurons based on maturity, morphology and function. The most commonly used astrocyte marker is glial fibrillary acidic protein (GFAP).[4] For oligodendrocytes, the marker O4 and RIP are often used.[3] For microglial cells, ionized calcium binding adaptor molecule 1 (Iba1) is often used.[5] For distinguishing neurons based on maturity a wide variety of markers can be used. Doublecortin (DCX) and neuronal differentiation factor 1 (NeuroD1) can be used to identify immature neurons. A common pan neuronal marker is beta tubulin III (TUJ1) which is commonly used to identify cells that have committed to the neuronal lineage.[6, 7] Microtubule associate protein 2 (MAP2) can be used to identify mature neurons and Hexaribonucleotide Binding Protein-3 (NeuN) and postsynaptic density protein 95 can be used to stain for even more mature neurons. Synapsin-I (Syn1) is an important maturity marker as well, indicating neurons have mature synapses and may be able to transmit electrical signals. Neuronal subtype markers for neurons that produce specific neurotransmitters such as glutamate, gamma aminobutyric acid (GABA), dopamine, serotonin, and choline can also be used to further classify mature neurons based on function.

1.2. Regenerative Capability of the Nervous System

Beyond their functions, a very important difference between neurons and glial cells is that neurons are amitotic whereas glial cells are capable of mitosis. While there are a few regions of the brain that have cells that can give rise to neurons (see section 1.3), for the most part, neurons cannot be replaced once damaged or destroyed. Damage and destruction of neurons leading to improper, or lack of neural tissue functioning has many causes. Trauma such as traumatic brain injury, peripheral nerve injury, spinal cord injury or stroke can be a cause. Neurodegeneration due to diseases such as Parkinson’s disease, amyotrophic lateral sclerosis, Alzheimer’s disease and

Huntington's disease can be a cause. Neurodevelopmental disorders, such as schizophrenia, cerebral palsy, and Rett Syndrome, can also be causes. [8-10]

In the peripheral nervous system, neurons can repair themselves if axonal damage is not too significant and their cell bodies remain intact. PNS neurons that undergo damage to their axons or severing of their axons, can repair their axons if the gap and/or damage between segments is less than the critical nerve gap, beyond which no recovery will occur. [11-13] The critical nerve gap is about 4 cm for humans, about 1.5 cm for rats and about 3 cm for rabbits. [12] Damage or gaps beyond this length, require interventional nerve repair such as autologous nerve grafting (current gold standard) or the use of biomaterial nerve guidance conduits, conduits with support cells and growth factors, or even gene therapy. [11, 14]

The CNS has significantly less regenerative capacity. It CNS is a much less supportive environment for neuronal regeneration and tends to impede neuronal regeneration. After damage has been incurred in the CNS, scar tissue called the glial scar forms to stabilize the damaged tissue by preventing inflammation and cellular degeneration. It is comprised of mostly reactive astrocytes. The astrocytes entangle with one another at the end of the damaged neuron process but over time become a thick membrane that blocks growth of the neuronal process.[15-17] These reactive astrocytes also release inhibitory chondroitin sulphate proteoglycans preventing axon regeneration. Debris of damaged myelinated neurons at the injury site also release myelin-associated inhibitors. Further neurons of the CNS are intrinsically less capable of regeneration as they do not upregulate the genes required for axonal growth as much as neurons of the PNS. [18, 19]

1.3. Cell Sources for Neuronal Regenerative Medicine and Tissue Engineering

Because the nervous system has little to no capacity to effectively repair itself, neural regenerative medicine and tissue engineering has become a very active field of investigation. Cell-based therapies for neurodegenerative diseases, neurodevelopmental disorders, neuronal regeneration, and *in vitro* platforms for fundamental neurological studies, drug-screening platforms, disease modelling and precision medicine platforms have all been investigated. [20-22] These therapies and study platforms are largely possible due to the development of methods to derive neurons from pluripotent and multipotent stem cells and, more recently, even other adult somatic cell types.

Pluripotent stem cells are cells that can give rise to any type of cell in the body. During gestation, the pluripotent embryonic stem cells (ESC) in early-stage embryos differentiate and give rise to all the cells that make up our bodily tissues. In 1994, Bain *et al*. showed that when cultured *in vitro*, embryonic stem cells could be guided to differentiate into the neuronal lineage. Since then, they have been a very useful tool for neuronal tissue engineering.[23] Their pluripotency allows them to differentiate indefinitely allowing for expansion and generation of sizeable populations of amitotic cells such as neurons. Their immaturity allows them to be excellent models for in vitro study of neurodevelopment and neurodevelopmental disorders. Indeed, most methods of differentiating ESC into neural cells rely on mimicking the development of the nervous system during gestation. However, in vivo uses for ESC derived neurons are limited by the fact that only allogenic transplants would be possible. [24] Further, there are some ethical concerns regarding the use of human embryonic stem cells.

In 2006, Takahashi and Yamanaka, developed a method to induce a pluripotent stem cell state in adult somatic cells using transcription factors, thus developing induced pluripotent stem cells (iPSC).[25, 26] This was a major development in the field, as iPSC have all the benefits of ESC

but can be generated from easy-to-acquire cells from living patients. This side steps the ethical concerns of ESC and allows for patient-specific cells to be derived which can be used for precision medicine and autologous or allogenic cell-based therapies. Further, because iPSC can be generated from human cells, iPSC disease modelling platforms offer great promise for drug discovery and disease modelling for neurological diseases as they can complement animal models and offer insight into human pathology.[25] Despite their benefits, there are still some concerns associated with the use of ESC that persist with the use of iPSC. Both iPSC and ESC cells have a risk of tumorgenicity and the formation of teratomas.[25, 27] Generation, expansion and differentiation of iPSC and ESC are very expensive (800,000 USD to generate iPSC-derived tissue suitable for clinical use in 2015). [25] Generation of iSPC and iPSC-derived cells is also currently very time consuming and inefficient. It takes about 3 – 4 weeks to generate iPSC and efficiencies are in the range of 0.01 – 0.1%. [28] After that cells have to be further expanded (2 – 3 months) and differentiated into neurons (about 4 weeks) and then differentiated into specialized neurons.

Multipotent stem cells that can be used to generate neurons include neural stem cells (NSC), and mesenchymal stem cells (MSC). Despite the nervous system having minimal regeneration capacity, it does have neural stem cells that can give rise to new neurons and glial cells. These NSC, and their slightly more specialized neural progenitor cells (NPC), also secrete factors that promote regeneration, direct differentiation in to neuronal subtypes, and help form neuronal networks.[29] They are present during neurogenesis of embryos and in the adult nervous system. In the adult nervous system, neural stem cell niches have been found the sub granular zone and the subventricular zone of the brain. NSC and NPC have also been isolated from the spinal cord and neural retina.[27] NSC and NPC can be isolated from deceased primary donor tissue or generated from other stem cells such as pluripotent stem cells.[27] NSC/NPC are promising cell sources for allogenic or autologous transplantation, depending on the cell source.

Another advantage is that they have low tumorigenicity.[30] Some groups have also investigated methods to modify endogenous NSC and NPC in situ for neural repair. [19, 29, 31] For in vitro study, NSC/NPC offer important into neurodevelopmental/degenerative disorders, neurogenesis, and cancers of the nervous system. [32-35]

MSC are adult stem cells that can be found in various places throughout the body including adipose tissue, amniotic fluid, endometrium, dental tissue, umbilical cord blood and bone marrow. Interestingly, while in the body they only differentiate into mesodermal cell types, it has been shown they can be transdifferentiated into neurons (a non-mesodermal cell type) both *in vitro* and *in vivo*. As with NSC, they have a low tumorgenicity. MSC also tend to migrate towards sites of inflammation and have immunosuppressive activity. [36, 37] MSC can also be harvested from living patients. Their clinical as autologous cell-based therapies, like other stem cells, are hindered by the time it takes to generate large volumes required for therapy and the high associated cost of generation, processing and storage. [36]

Recently it has been shown that neurons can be derived from non-stem cells. In 2010, Vierbuchen *et al.* showed that fibroblasts can be directly converted to neurons with an intermediary stem cell state (Figure 1.1). [38] Since then direct neuronal reprogramming has been achieved with hepatocytes, peripheral T cells, and astrocytes, amongst other cells. [39-45] Using this method, autologous cell sources for cell-based therapies can be generated in situ without a proliferative stem cell-like stage. Because cells do not have to transit a pluripotent state, expansion and subsequent differentiation, this technique is significantly faster as well.[46] Further, it is speculated that the induced neuronal (iN) cells generated by direct neuronal reprogramming, can maintain aging and epigenetic signatures of the patient.[47-51] Thus, iN cells also have potential as a cell source for *in vitro* disease modelling. Due to the novelty of the direct neuronal reprogramming field, there are still many outstanding questions currently being investigated. It is unknown whether an intermediate neural progenitor cell state is involved, how similar iN are to

native neurons, and whether they can be integrated into the brain. Additionally effective non-viral transfection methods, and improved reprogramming efficiency are still under investigation. [52]

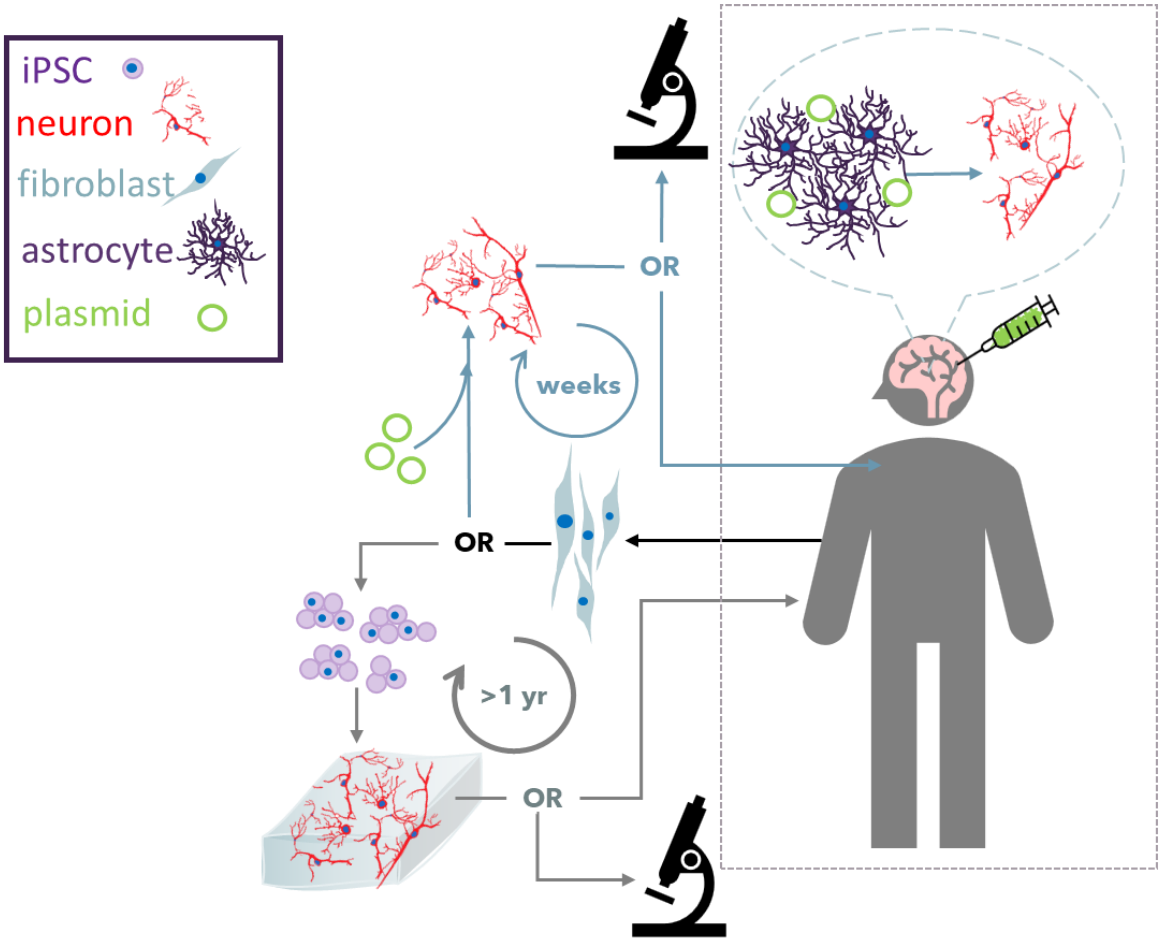

Figure 1.1 – Schematic illustrating the differences between neuron regeneration using direct neuronal reprogramming and neuronal regeneration using stem cells. Prepared using PowerPoint® a registered trademark of Microsoft Corporation.

1.4. The Use of Biophysical Cues to Enhance Neuronal Differentiation for Tissue Engineering and Regenerative Medicine

Since contact guidance plays a major role in many neural processes, there is interest in developing technologies that mimic the biophysical cues of the native neural extracellular matrix (ECM) to help enhance neuronal processes on synthetic platforms. Of particular interest is the use of these platforms to improve the efficiency neuronal differentiation of stem cells.

Conventional methods of neural differentiation rely primarily on the use of biochemical factors as a means of process regulation; however this method alone has proven to be expensive, result in long differentiation periods, and provide minimal control over lineage-commitment. [53-55] Incorporation of biophysical cues, such as topography, stiffness, electrical stimulation or viscoelasticity, in synthetic substrates has been shown to significantly enhance neuronal differentiation. These platforms increase differentiation rate, reduce cost, and promote lineage specific differentiation improving neuronal yield.[53-60] This section will focus on the key parameters that need to be considered when designing biomaterials that incorporate the biophysical cues of stiffness or topography, provide a brief overview of the efforts to optimize these parameters, and identify parameters that still need further study and optimization.

1.4.1. Optimization of Topography Alignment and Dimensions

Inspired by the phenomenon of neuronal contact guidance and fiber structures in the native ECM, topographical studies have mostly focused on anisotropic topographies. Indeed, these patterns have been shown to enhance neuronal differentiation induction, reducing differentiation times, and decreasing the dependence on soluble biochemical cues required to induce differentiation. Further, this enhancement by anisotropic patterns is not only limited to a certain cell type or differentiation pathway, but also in both pluripotent and multipotent cells undergoing either direct differentiation or trans-differentiation. The effects of anisotropic patterns stems largely from their ability to provide contact guidance, which can influence cell morphology and gene expression. The anisotropic patterns cause cells to elongate, altering focal adhesions and promoting cytoskeletal reorganization (Figure 1.2).[57, 61-67] Isotropic patterns have been shown to promote the induction of glial differentiation.[61, 68, 69] The reason this occurs is not well understood, but it is suggested that it may be due to isotropic patterns' inability to induce cell morphologies that encourage focal adhesion formation and cytoskeletal changes required for

inducing neuronal lineage.[57, 61] Thus, in this review, anisotropic patterns used to enhance neuronal differentiation, with the most commonly studied gratings and fibers will be discussed. A summary can be found in Table 1.1.

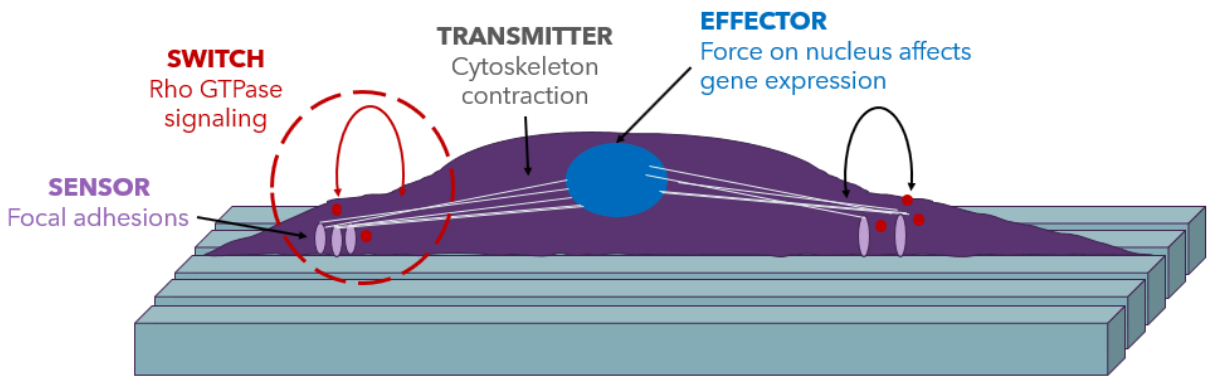

Exact relations are still not well understood

	Feature	Rho GTPase activation	Focal adhesion formation	Contractility
Topography	↓	↓	↑ or ↓	↑ or ↓
Stiffness	↓	↓	↓	↓

Figure 1.2 – Overview of key components involved in mechanotransduction. A simplified view of the relation between focal adhesions which act as sensors, the cytoskeleton which acts to transmit signals via contraction, the nucleus whose shape changes from the force of the cytoskeletal contraction affecting gene expression, and Rho GTPase signaling which acts as a regulating switch for the process. This schematic was drawn based on the information in the review paper by Yim *et al.*[70]

1.4.2. Optimization of Nano- and Micrograting's' Dimensions

Gratings, also commonly referred to as ridges or grooves, are patterns of parallel line channels that can be rectangular, rounded or v-shaped. Methods commonly used for fabrication of micro- and nanoscale grating topographies include, soft lithography, photolithography, thermal lithography, plasma lithography, electron beam lithography, nano-imprinting, and electric field-aided casting. [62, 64, 71] It is recommended that the reader reference Teo *et al*., Jeon *et al*. and James et al. for reviews of topography fabrication techniques.[64, 71, 72] Key parameters that can

determine how gratings will affect cell behaviors include the width, depth, and the aspect ratio of the depth to width. In general, features wider than soma diameter (12 μm ± 3 μm) or the average filopodia extension length do not encourage efficient interaction with cells resulting in differentiation efficiency that is comparable to that of un-patterned substrates.[73-75] In addition, known native ECM topographies are also primarily less than 10 μm in diameter. Therefore, grating widths in the range of 250 nm – 10 μm that have been shown to enhance neuronal differentiation of a variety of cell types are normally considered. [61, 68, 69, 73, 75-79] Using 250 nm, 350 nm and 2 μm wide gratings, direct neuronal differentiation was induced in ESCs and iPSCs without or with minimal use of biochemical factors. In these systems, earlier upregulation of neuronal lineage markers, and increased preference for the neuronal lineage were observed (Figure 2).[61, 75, 76, 79, 80] Furthermore, it was also found that alignment, extension and neurite outgrowth of individual cells and colonies decreased with grating width .[75, 81] For NSCs or NPCs, grating widths in the range of 250 nm – 10 μm have been shown to increase early upregulation of neuronal markers such as TUJ1 and increase preference for the neuronal lineage compared to planar substrates.[68] In this range, an inverse relationship between grating width and neuronal marker upregulation has been observed; however, no similar relationships could be drawn between the preference for neuronal lineage commitment. [69, 82] For MSCs only nano-widths (250 nm and 350 nm) were shown to have a significant impact on the directed neuronal differentiation. Interestingly, the effect was even stronger than that of retinoic acid alone on an un-patterned surface. [63, 77, 83, 84] It has also been proposed that an upper limit on grating width of 1.9 μm may also exist for MSC. In a combination of TEM observation and computational modeling, Zeng et al. proposes a model showing that for grating widths above 1.9 μm, the basal cell membrane tend to bend into the grooves, which correlates with reducing elongation and alignment of MSC on grating surfaces.[85]

In general, grating depths in the range of 250 nm – 4 μm are most commonly studied. [61, 68, 69, 73, 75-77] Not many studies have investigated the effect of grating depth on neuronal differentiation. However, a correlation between grating depth and preferential neuronal

differentiation of NPCs has been observed. Using NPCs on 2 µm wide gratings and media favouring astrocyte differentiation, Chua *et al*.[86] showed that if the 2 µm gratings with depth of 2-4 µm, more cells differentiated into neurons rather than astrocytes. This trend of increased neuron differentiation with increased depth, was maintained up until a saturation point of 2-4 µm in depth. Beyond this point, perpendicular neurite growth was hindered due to the high energy costs of neurites bending in deep grooves. A similar trend was shown using iPSCs, wherein increasing grating depth from 150 nm to 560 nm (using grating widths of 500 nm and 1 µm), significantly increased the fraction of cells committed to the neuronal lineage.[81] It was also shown, that grating depth relative to width, also referred to as aspect ratio, can also impact cell behavior. Chan *et al*. found that ESC on micro gratings with 1:1 aspect ratios has the greatest elongation and alignment.[75] A similar result using MSC was observed by Wong et al., wherein aspect ratio was shown to be better at predicting cell elongation and alignment than either depth or width alone.[66] Thus, depth, width and aspect ratio play a significant role in the topographical modification of cell behavior.

1.4.3. Optimization of Fiber Dimensions and Orientation

Fibrous scaffolds closely resemble the native nervous system ECM fibrils, as they are made of mesh of micro- and/or nanoscale fibers. In these meshes, fibers can either be aligned in parallel or randomly oriented as present in native CNS and PNS ECM structures. There are many methods of fibrous scaffold fabrication, however, the most commonly used for tissue engineering purposes are electrospinning, phase separation and self-assembly.[62, 87] It is recommended that the reader reference Sultana *et al*.[88] for a review on fibrous scaffold fabrication and materials for tissue engineering purposes. Diameter and orientation of fibers are key dimensions that can determine how they will affect cell behavior. Almost all published studies use fibers with diameters in the range of 200 nm – 2 µm similar to collagen fiber bundle thickness observed in PNS

endoneurium and perineurium structures.[89-92] Similar to gratings, there is no consensus on the optimal fiber diameter. However, there seems to be a consensus on the optimal orientation. Early reports indicated that fiber orientation did not impact neuronal differentiation efficiency[93], but subsequent studies overwhelmingly showed the opposite. Fiber alignment was shown to significantly improved neuronal differentiation in a variety of cell types including ESCs, iPSCs,[90, 94, 95] NSCs [89, 92, 96, 97] and MSCs.[91, 98] Embryoid bodies on aligned fibers extended along the fiber axis and had more extensive neurite outgrowth compared to random and planar substrates. On randomly oriented fibers, both ESCs and NSCs tended to extend in multiple directions and became glial-like in morphology. For neuronal differentiation of ESCs, biochemical factors were still required. However, when used in combination with aligned fibers, embryoid bodies showed higher upregulation of neuronal markers, and the neuronal lineage was promoted over the glial (astrocyte) lineage, which was suppressed.[90, 95] Similar results were observed when using NSCs, wherein on aligned fibers, cells had a more elongated morphology compared to random or planar substrates. [89, 92, 93, 97, 99, 100] Upregulation of neuronal markers and increased neuronal yield were observed in NSCs grown on fibers. [89, 92, 96, 97, 99, 100] Similar to what was observed with ESCs, in addition to a bias in neuronal lineage commitment, a negative selection against the glial lineage (oligodendrocytes) was also observed in NSCs.[92] The effect of alignment was even more significant for MSCs. Only MSCs grown on aligned substrates showed improvement in neuronal differentiation, specifically neuronal marker upregulation and a preference to the neuronal lineage over the glial lineage. MSCs grown on random fibers performed equally as well as planar substrates.[91, 98]

The effect of fiber diameter is less clear and optimal fiber diameters widely vary depending on the study design. Early studies using NSCs reported that nanoscale fibers were much more effective that microfibers (300 nm vs 1 µm) for increasing neuronal differentiation rates.[93] Two later studies have shown that while nanofibers outperform microfibers, larger nanofibers are more effective than smaller nanofibers (749 nm vs. 283 nm and 480 nm vs. 260 nm) at increasing

neuronal differentiation rate and yield when using NSC. [89, 92] However, using ESC derived neural progenitors, it was reported that 400 nm fibers performed better than 800 nm fibers, so the optimal fiber diameter may be in the mid-range of the nanoscale.[99] Thus, fiber diameter plays a significant role in the topographical modification of cell behavior. It is of interest for future studies using different cell types than those mentioned here, such as iPSCs or MSCs, to incorporate this parameter into their analysis.

1.4.4. Optimization of Topography Application Sequence and Combination

Previous studies, like those outlined above, tended to focus on early induction and lineage commitment. However, to develop optimal systems resulting in fully functional neurons, enhancement of all differentiation phases is likely required. Interestingly, it has been shown that sequentially applied topographies can further improve neuronal differentiation as cells can "remember" past topographies. [75, 101] Additionally, topographies that were once thought to be of no value to neuronal differentiation, such as isotropic patterns, have recently been shown to improve differentiation, when applied during later phases, such as maturation. Thus, there is potential to create systems where the benefits of certain topographies applied at different stages can be "added" together to improve the overall differentiation process.

It has previously been shown that cells store information from past environments and that this information can continue to influence cell fate in the future. [75, 102, 103] Using ESC and iPSC, Chan *et al*. demonstrated this memory effect for pluripotent cells undergoing neuronal differentiation. They showed that ESCs and iPSCs have a mechanical memory of their past environments and the topographical signals that they were exposed to during different stages of the maintenance and neuronal differentiation. PSCs were exposed to topography during maintenance, and/or during neuronal differentiation. Remarkably, when PSCs were exposed to grating pattern in the maintenance phase, and then PSCs were moved to planar substrate,

enhanced neuronal differentiation was observed. Furthermore, they showed that the effect of topography can indeed be additive. By incorporating a topographical priming step, they were able to decrease the differentiation period and reduce the amount of biochemical cues required. [75] Similarly, Yang *et al*. demonstrated hierarchical pattern-induced cells continued to exhibit enhanced neuronal differentiation even after the topography was removed. [101] In addition, *in vivo* regional priming of primary NPC was also shown to play a major role in cell response to *in vitro* application of topography. [104] Notably, differentiation efficiency and morphological changes depended more on the cell source than on the topography being used. For example, although hippocampal cells were slightly more elongated than cortical cells aligned along the gratings, only hippocampal neurons showed significant elongation on pillars. [104]

Interestingly, optimal topography was found to differ in different phases of differentiation. While gratings enhance the initial stages of neuronal differentiation of iPSCs into dopaminergic neurons, pillars were better at enhancing maturation. Maturation of cells on pillars resulted in increased neurite branching, and enhanced maturation with more cells being capable of repetitive firing, as compared to cells that matured on gratings or planar substrates.[56] This is rather surprising as pillars were previously thought to enhance glial morphologies and have no effects on neuronal differentiation.[61, 68, 69] Using a combination of gratings for the early stages of differentiation and pillars for maturation, it is possible to increase both the yield of mature dopaminergic neurons and differentiation rate (repetitive firing at 4 weeks compared to 55-70 days).[56] Thus, there is great potential to increase control and enhancement of differentiation into functional neurons by optimizing the temporal and sequential parameters of topography.

Table 1.1 - Stem cell behavior on gratings and electrospun fibers. Legend. H = height, W = width, S = spacing, D = diameter, P = pitch.

Type(s) of Topography	Material	Starting Cell Type	Mechanistic Study (Y/N)	Major Findings	Study
Nano- / micropatterning					
Equally space nanogratings (H=150 nm and 560 nm, W=500 and 1000 nm). Hexagonally arranged nanopillars (H=150 or 560 nm, D=500 nm)	Poly(dimethylsiloxane) incubated with 1% Geltrex	iPSC	Y (YAP expression)	Gratings with heights of 560 nm showed the best performance, reducing cell proliferation, enhancing cytoplasmic localization of YAP and promoting neuronal differentiation (compared to the flat control). YAP localizations are critical to induce neural differentiation.	Song *et al*. 2016 [81]
Nanogratings (H=250nm, W=250 nm, 1 µm, 10 µm, S=500nm, 2 µm, 20 µm)	Poly(dimethylsiloxane) coated with bovine fibronectin	MSC	Y (Focal adhesion kinase)	Gratings with 250 nm line widths upregulated neurogenic and myogenic differentiation markers. Focal adhesions on nanogratings were smaller and more elongated than those seem on micro gratings or control.	Teo *et al.* 2013 [63]
Nanogratings (H=300 nm,W=350 nm, 2 µm, and 5 µm)	Poly(dimethylsiloxane) coated with 1:80 diluted Matrigel	iPSC	N	Neuronal marker expression was inversely proportional to width.	Pan *et al.* 2013 [80]
Nanogratings (H=350 nm, W=350nm, 1 µm, 10um; S =700 nm, 2 µm, 20 µm)	Poly(dimethylsiloxane) coated with bovine collagen I	MSC	N	The effect of nanogratings alone was greater than the effect of retinoic acid on flat substrates, regarding upregulation of neuronal markers.	Yim *et al.* 2007 [77]
Nanogratings (H=500 nm, S=250 nm)	Polyurethane acrylate on glass coverslip	ESC	N	Nanoscale gratings alone can induce the differentiation of ESC into a neuronal lineage without the use of differentiation-inducing agents.	Lee *et al*. 2010 [76]

Nanogratings (H=625nm, W=S=1.5 µm) Nanopores (S=28nm, pore size=10nm) Hierarchical (combination of nanopores and nanogratings)	Polystyrene-Poly(methyl methacrylate) random copolymer and Polystyrene-Poly(methyl methacrylate) block copolymer	NSC	Y (β1 integrin-mediated binding, intracellular Rho-associated protein kinase pathway)	Cells have a mechanical memory of the conditions under which neuronal differentiation was induced. Enhanced neuronal differentiation persisted even after the removal of the hierarchical pattern.	Yang *et al*. 2014 [102]
Microgratings (H=W=S=2µm)	Poly(dimethylsiloxane) coated with Matrigel	ESC and iPSC	N	The effect of topography is additive. An initial exposure to 2um increase neural differentiation rate and an additional culture period can improve neural differentiation.	Chan *et al*. 2012 [75]
Microgratings (H=W=S=2µm) Micropillars (H=2µm, P=12µm and D=2µm)	Poly(dimethylsiloxane) coated with poly-L-ornithine, fibronectin and laminin	iPSC	N	Gratings are beneficial for early stage of differentiation (lineage commitment). Pillars are beneficial for later stages (maturation). Sequential application resulted in significantly increased overall differentiation rate.	Tan *et al*. 2018 [56]
Nanogratings and microgratings: i. H=W=S=250nm ii. H=120nm, S=1µm, W=2um iii. H=80nm, S=2µm, W=1µm iv. H=W=S =2µm Nanopillars: v. H=1 µm, P=6.5 µm, H= 1 µm Nanowells: vi. H=2µm, P=12µm, H=2µm Hierarchical: vii. 250nm gratings with 250nm space perpendicular to 2 µm gratings.	Poly(dimethylsiloxane) coated with poly-L-ornithine and laminin	ESC	N	High throughput topography screening. Anisotropic patterns promote neuronal differentiation and isotropic patterns promote glial differentiation.	Ankam *et al*. 2013 [61]
Nanogratings H=W=S=250nm	Poly(dimethylsiloxane) coated with poly-L-ornithine and laminin	ESC	Y (actomyosin contractility and YAP/TAZ pathway)	Nanotopography induces high actomyosin contractility which is crucial for ESC commitment to neuronal lineage. YAP localized to cytoplasm.	Ankam *et al.* 2015 [57]
Nanogratings and microgratings (H =0.35 µm, 0.8 µm, 2 µm and 4 µm, W=2 µm, S=2 µm)	Poly(dimethylsiloxane) coated with poly-L-ornithine and laminin	NPC	Y (Cytoskeletal bending)	Cells can sense the depth of micro-gratings. Neurite elongation, alignment and neuronal	Chua *et al*. 2014 [86]

				differentiation increased with grating depth. Filopodial adhesion in growth cones favour elongation but the neurite cytoskeleton resists it.	
Electrospun fibers					
Aligned and random nanofibers, D=250 nm	Electrospun polycaprolactone	ESC	N	Aligned nanofibers enhanced differentiation into neural lineage and directed neurite outgrowth	Xie *et al*. 2008 [90]
Aligned and randomly oriented nanofibers, D=260 nm, 480 nm and 930 nm	Electrospun polycaprolactone coated with poly-L-ornithine and laminin	NSC	Y (Wnt Signaling)	Highest yield of neuronal progenitors on 480 nm aligned fibers, due to selectivity against oligodendrocytes and increase in canonical Wnt signaling.	Lim *et al.* 2010 [92]
Aligned nanofibers, D=270 nm	Electrospun polycaprolactone and gelatin	MSC	N	Aligned fibers up-regulated neural markers at both the protein and mRNA level, compared to the control.	Jiang *et al*. 2011 [91]
Aligned and randomly oriented nanofibers, D=400 nm and 800 nm	Tussah silk fibroin	ESC-derived NPCs	N	Aligned fibers significantly promoted neuronal differentiation and neurite outgrowth. Cells on 400 nm fibers had higher viability, differentiation and neurite outgrowth.	Wang *et al*. 2011 [105]
Randomly oriented nanofibers, D=283 nm, 749 nm, 153 nm, 1452 nm.	Laminin coated electrospun polyether sulfone	NSC	N	Fiber diameter was found to be inversely proportional to proliferation and cell spreading, and directly proportional to degree of cell aggregation.	Christopherson *et al*. 2009 [89]

1.4.5. Effect of Stiffness on Neuronal Differentiation

The effect of substrate stiffness has less parameters to optimize compared to topography. Thus, there seems to more consensus in the field as to which range of stiffnesses are optimal for enhancing neuronal differentiation. In general, stem cell differentiation to a certain lineage is best enhanced by substrates that match the stiffness of the native tissue in which that cell lineage resides. The average Young's modulus of native adult brain tissue has been reported to be in the range of 0.5 – 3.4 kPa.[106-109] It has also been reported that brain stiffness varies with myelin content, age, and neurodegeneration. Weickenmeier *et al*. found that there was a significant difference between the average stiffnesses of grey matter (0.68 kPa) and white matter (1.33 kPa) of bovine brains. Further they found between brain samples, there was significant variation in maximum white matter stiffness (0.59 – 2.45 kPa).[107] This is significant as immature brains are not completely myelinated and thus are softer. Using mouse embryonic cerebral cortex as an experimental model, Iwashita *et al*. showed there is considerable change in stiffness of the subventricular zones, where stem cells reside. Earliest measurements recorded an average stiffness of 74 Pa, and the latest measurement recorded an average stiffness of 169 Pa. They also noted that neuronal stiffness increased with cytoskeletal maturation (154.7 Pa at the earliest time point to 230.5 Pa at the latest time point).[110] Looking at adult brains aged 20 to 60, it has also been shown that the stiffness of multiple brain regions decreases with age.[111] Neurodegenerative diseases such as Alzheimer's have also been shown to decrease regional brain stiffnesses. [106, 112]

Indeed, empirical findings have indeed shown that substrates with stiffnesses in the range of 0.1 – 10 kPa enhance neuronal differentiation. [108, 113-119] Saha *et al*. found that stiffnesses in the range of 0.1 – 0.5 kPa promote commitment to the neuronal lineage, and stiffnesses in the range of 1 – 10 kPa promote the glial lineage.[113] Leipzig and Shoichet found that substrates with stiffnesses < 1 kPa best promoted neuronal differentiation and substrates >

7 kPa promoted oligodendrocyte differentiation. They also found the optimal stiffness for NSC proliferation was 3.5 kPa. [108] Teixeira *et al*. investigated maturation of neurons derived from stem-cells, and found that once again softer substrates, better promoted maturation. They found substrates in the range of 12 kPa to approximately 0 kPa, increased the rate of neuronal maturation. [118] The exact mechanotransduction mechanism responsible for stiffness effects on neuronal differentiation are not well understood and are subject of current investigation (Figure 1.2). Stiff substrates have been shown to activate Rho GTPases[70, 119, 120], increase focal adhesions[117, 121, 122], and increase contractility.[119, 123, 124]

1.5. Limitations in the field and hypotheses

Despite the breadth of knowledge in the study of biophysical cues to enhance neuronal differentiation, there are still many outstanding questions. The effect of biophysical cues such as topography have yet to be studied for novel neuronal regeneration techniques such as direct neuronal reprogramming. The low programing efficiency of nonviral neuronal reprogramming is a persistent problem in the field and major roadblock to clinical application. Implementation of topographical cues has been shown to be a simple and cost-effective method to enhance lineage-directed neuronal differentiation and contact guidance of mature neurons. We hypothesize that since topographical cues have been applied successfully to enhance lineage-directed differentiation and multipotent stem cell transdifferentiation, they could also improve nonviral neuronal reprogramming efficiency.

Further, for lineage based and non-lineage based neuronal differentiation, biophysical cues such as topography and stiffness have been thoroughly studied, but only independently. It is of interest to see if their combined application results in synergistic effects or other interactions. However, there is difficulty in producing a material that can be patterned with microtopographies, has controllable stiffness and to which cells can attach for a long period of time. Especially for neuronal differentiation studies wherein cells must attach to the substrate for the differentiation

period and the resulting neurons must also attach during maturation, all of which can take up to a month. We hypothesize, a polyacrylamide-based gel could be fabricated to meet stiffness and topography requirements, and then modified with carbodiimide conjugation of extracellular matrix and/or charged polypeptides to allow for extended periods of neural progenitor cell and neural cell attachment. Once developed, this platform can be used to study the combined effects of topography and stiffness on neuronal differentiation.

An understanding of the interaction between stiffness and topography is important for a few reasons. First, it is impossible to impart only the cue of topography as topography can only be applied on substrate which will have some characteristic stiffness. Thus, when designing biomaterials with topography, it is important to consider how the effect of topography may differ with substrate stiffness. Second, it allows for the opportunity to potentially design substrates that are even better tailored to promoting neuronal differentiation because multiple cues could be optimized. We hypothesized that effects of stiffness and topography on neuronal differentiation would be dependent on one another.

1.6. Research scope and thesis outline

To address the gaps outlined in Section 1.5, the aims of this thesis are as follows:

Aim 1 *– Investigate whether topography can enhance efficiency of non-viral direct neuronal reprogramming on topographical patterns.*

To investigate whether topography can enhance non-viral direct neuronal reprogramming, we will preform transfections on various micro- and nanotopographies. A polymer-BAM (Brn2, Ascl1, Myt1l) factor transfection polypex will be used to reprogram primary mouse embryonic fibroblasts into induced neuronal (iN) cells. Using a multiarchitecture chip, we will screen for patterns that may improve transfection and subsequent induced neuronal reprogramming efficiency. The first round of screening will use a GFP reporter gene to determine if any topographies can improve transfection efficiency. The second round of

screening will use BAM reprogramming to reprogram fibroblasts to iN cells. These iN cells will be identified using beta-tubulin III (TUJ1). Selected patterns will then be investigated further by analyzing lineage commitment using TUJ1 and maturity using microtubule-associated protein 2 (MAP2) protein, cell morphology and electrophysiological function of induced neurons.

Aim 2 *– Develop a platform that allows for the investigation of the combine effects of stiffness and topography on neuronal differentiation over an extended period of time.*

To study the combined cues of microtopography and stiffness we will modify a polyacrylamide - N-acryloyl-6-aminocaproic acid copolymer (PAA-ACA) using carbodiimide crosslinking. First, we will test if this gel can be fabricated with suitable stiffness and microtopographies. If successful, we will then test different methods of conjugating laminin to the substrate to promote cell adhesion of human and mouse neural progenitor cells (hNPC and mNPC). Laminin alone, laminin with a charged polypeptide intermediary, and laminin with heparin will all be considered. Which ever of these methods support initial cell adhesion will then be test for extended cell to ensure the progenitor cells and their subsequently derived neurons can adhere for the entire differentiation period (14 – 28 days).

Aim 3 *– Use the developed gel platform to investigate the combined effect of stiffness and topography on neuronal differentiation.*

To identify potential interactions between stiffness and topography when applied simultaneously, we will differentiate mNPCs for 14 days on PAA-ACA gels of four different stiffnesses, and four different topographies. Lineage commitment preference on the substrate will be gauged by determining the percentage of cells that are positive for the neuronal marker TUJ1, and the astrocyte marker glial fibrillary acidic protein (GFAP). Neuronal maturity will be gauged by determining the percentage of cells that are positive for the mature neuronal marker MAP2. Neuronal morphology will also be assessed by measuring neurite length and branching.

CHAPTER

2

Enhanced efficiency of nonviral direct neuronal reprogramming on topographical patterns

2.1. Introduction

Direct neuronal reprogramming is the reprogramming of adult somatic cells to adult neurons, without the introduction of an intermediary pluripotent state. This method of cellular reprogramming offers exciting new opportunities in the field of regenerative medicine, and disease modelling.[46, 49, 125] Using this method, autologous cell sources for cell-based therapies can be generated in situ without a proliferative stem cell-like stage. Because cells do not have to transit a pluripotent state, expansion and subsequent differentiation, this technique is significantly faster as well.[46] Further, it is speculated that the induced neuronal (iN) cells generated by direct neuronal reprogramming, can maintain aging and epigenetic signatures of the patient. Thus, iN cells also have potential as a cell source for *in vitro* disease modelling.[48, 49]

A variety of different methods have been employed to generate iN cells including transcription factors, microRNAs and small molecules that regulate developmental pathways.[46, 49] One such method is the use of three transcription factors *Brn2*, *Ascl1*, and *Mytl1* (BAM factors) developed by Vierbuchen *et al*., that have been shown to reprogram a variety of cell types into functional iN cells.[38] A multitude of different gene delivery methods have been employed to deliver BAM factors for direct neuronal reprogramming. So far, the most efficient method has been the use of viral gene delivery (2-20% reprogramming). [38, 126, 127] However, the use of viruses poses challenges to clinical translation regarding safety. Non-viral methods, both physical and chemical, have been developed as alternatives. Physical methods such as electroporation or ultrasound rely on membrane disruption and *in vitro* have shown efficiency comparable to that of viral transfection (9 – 12%). However, *in vivo* translation remains a challenge and these methods can cause excessive cell damage. [128-130] Chemical methods, such as lipids, polymers, inorganic and hybrid carriers, are more amenable to *in vivo* translation. However, chemical non-viral direct neuronal reprogramming systems tend to have significantly lower reprogramming efficiency (0.05 – 2%, with single doses).[131]

Studies have been able to increase the efficiency of these systems by combining them with physical methods or adding in small molecules, but this increases the overall cost and complexity. Additionally, the same barriers to in vivo translation posed by physical systems alone still persistA reprogramming method developed by Adler *et al*. that uses a non-viral polymer gene vector developed by Lin *et al.* [132] called poly(N,N-cystaminebisacrylamide-4-amino-1-butanol) (poly(CBA-ABOL)), was able to increase neuronal reprogramming efficiency to almost 8% using five doses, without the incorporation of physical methods.[131] While this is a significant improvement, this efficiency is still much lower than that of viral reprogramming. The issue of low reprogramming efficiency poses a significant problem as large volumes of iN cells would be required for both *in vitro* and *in vivo* applications. [46, 48, 133]

One way to improve efficiency, could be the incorporation of topography. Inspired by the phenomenon of contact guidance and the physical microenvironment of the native stem cell niche, nano- and microtopograhical substrates have been shown enhance lineage-directed differentiation and transdifferentiation of multipotent stem cells. In these systems, topographical cues significantly increased the differentiation rate and neuronal yield. In general, anisotropic patterns have provided the most significant improvement due to their ability to alter focal adhesions and promote cytoskeletal reorganization which in turn affects gene expression. [67, 70, 134-139] Topography has also been shown to promote non-viral gene delivery. Both anisotropic and isotropic patterns have been shown to “prime” cells before nonviral transfection by modulating their integrin binding, focal adhesion formation, cytoskeletal organization, endocytic mechanisms and intracellular trafficking.[140-142] A study by Kulangara *et al*. even demonstrated that topography can be used to enhance viral neuronal reprogramming with BAM factors. [143]

Thus, we hypothesized, the incorporation of biophysical cues in the form of topography, may improve the efficiency of non-viral neuronal reprogramming. To investigate this, we used a high-throughput screening tool, the Multiarchitecture Chip (MARC), to screen fifteen patterns of varying dimensions and geometries to see which, if any, could enhance non-viral transfection and

non-viral direct neuronal reprogramming. Patterns that stood out during screening were used in subsequent single pattern studies to further investigate their effect on non-viral direct neuronal reprogramming. The maturation and functionality of the iN cells produced on patterns were then characterized by expression of neuronal markers, morphology, and electrophysiological analysis.

2.2. Methods and Materials

2.2.1. Molecular Cloning and Plasmid Purification

The pUNO1-mAscl1 (3892 bp) and pUNO1-mMyt1lb (6744 bp) were purchased from InvivoGen (San Diego, CA, USA). pUNO1-mBrn2 (4513 bp) was generated by first amplifying the Brn2 cassette from pmax-Brn2 [131] by PCR (left primer: CAAATGACCGGTCACCATGGCGACCGC, right primer: CTCCCCCTGAACCTGAAAC), creating an AgeI restriction enzyme site near the 5' end of the amplicon. To improve cloning efficiency, the PCR product was sub-cloned into a TOPO-ligase conjugated vector. The intermediate plasmid and pUNO-mAscl1 were digested AgeI and HpaI restriction enzymes, then separated by agarose gel electrophoresis, extracted, and purified by ethanol precipitation. The Brn2 insert was ligated into the pUNO-mAscl1 backbone, transformed into DH5α *E. coli* (Invitrogen, Carlsbad, CA, USA), selected by colony PCR, expanded and purified (Plasmid Mini Kit, Qiagen, Hilden, Germany), and validated by sequencing, immunocytochemistry, and Western blot. The reporter vector pmax-GFP (3486 bp, Amaxa, Cologne, Germany) which expresses GFP under control of CMV promoter, was used for measurement of transfection efficiency. To generate the plasmid pLV-hSyn1-GFP, pLV-hSyn-RFP (Addgene #22909) was digested with restriction enzymes AgeI and PmeI, and pmaxFP-Green-N (Amaxa, Cologne, Germany) was digested with AgeI and HpaI. Following agarose gel electrophoresis and gel extraction, the GFP fragment was ligated into the pLV-hSyn backbone and transformed into Stbl3 E. coli (Invitrogen). A sequence-

validated clone was expanded, purified (EndoFree Plasmid Maxi Kit, Qiagen), and used for viral packaging.

2.2.2. Poly(CBA-ABOL) Synthesis and Bulk Polyplex Formation

The protocol used by Adler *et al.*, for Poly(CBA-ABOL) synthesized and bulk polyplex formation was used in this study.[131] Briefly, N,N-cystaminebisacrylamide (CBA) (Polysciences, Warrington, PA) and 4-amino-1-butanol (ABOL) (Sigma-Aldrich, Saint Louis, MO) were combined via Michael polyaddition as described by Lin *et al*. [144] The reaction product was purified by dialysis, in acidic deionized water and then lyophilized. The polymer was collected in its HCl-salt form and its structure validated by ^{1}H NMR (in D_2O) on a Varian Mercury 300 MHz NMR Spectrometer. Lyophilized p(CBA-ABOL) was dissolved in molecular grade water at a final concentration of 50 µg/µL. p(CBA-ABOL)/DNA nanocomplexes (polyplexes) were synthesized at a polymer:DNA mass ratio of 45:1, which was selected based on a preliminary optimization.[131] Polyplexes were prepared by adding a HEPES buffer solution (20 mM HEPES, 5 wt % glucose, pH 7.4) of p(CBA-ABOL) (844 µg p(CBA-ABOL)/mL) to a HEPES buffer solution (20 mM HEPES, 5 wt % glucose, pH 7.4) of plasmid DNA (75 µg/mL), followed immediately by vortexing for 20 seconds. A dose of 0.25 µg DNA/cm^2 was used for all experiments.

2.2.3. Lentiviral Production

HEK293FT cells (Invitrogen) were seeded in a 75 cm^2 flask, cultured in DMEM (Gibco, Carlsbad, CA, USA) containing 10% fetal bovine serum (Gibco) and 25 µg/mL gentamicin (Gibco), and were transfected using Lipofectamine 2000 (Invitrogen) with 5.14 µg pMD2.G (Addgene #12259), 9.73 µg psPAX2 (Addgene #12260), and 15 µg of pLV-hSyn1-GFP according to the

manufacturer's protocol. Culture media was discarded and replaced after one day. Three days after transfection, the medium was collected and passed through a 0.45 μm syringe filter to remove cell debris. The supernatant was then concentrated to 30× in Amicon Ultra centrifugal filter tubes (MWCO 100 kDa, Millipore, Billerica, MA, USA), and the concentrated virus was aliquoted and stored at −80 °C.

2.2.4. Preparation of Multi-Architecture Chip (MARC) Arrays and Single Patterns

Both MARC arrays and single patterns were fabricated via soft lithography on Polydimethylsiloxane (PDMS) (Sylgard™184, Elastomer Kit, Dow Corning) An elastomer to curing agent ratio of 10:1 was prepared, degassed and then poured on to silanized PDMS master molds. Both the circular and rectangle MARC designs were used in this study (Figure 2.1B). A description of MARC master mold fabrication can be found in Moe *et al*. [145] and Ankam *et al*. [146] A list of single patterns used in this study, a description of the pattern features, and the shortened name used to refer to the pattern can be found in Table 1. Topographical features were characterized by scanning electron microscopy (SEM) and the Olympus LEXT OLS4100 laser confocal microscope. (Figure 2.1C). A schematic of the MARC used for screening can be seen in Figure 2.1B. Samples were placed under vacuum for at least 1 hr to remove any air bubble and then move to a 60 ^{o}C oven to cure overnight. Once cured, the PDMS samples were left in the oven for an additional seven days. Samples were then stored at room temperature until use. Samples were air-plasma treated for two minutes (Harrick Expanded Plasma Cleaner). Prior to seeding cells, samples were sterilized for one hour with 75% ethanol and ultraviolet irradiation. They were then placed in a 6-well tissue culture plate and coated with 100 μL of fibronectin (Sigma) in sterile water (50 μg/mL) in a 37 °C incubator for one hour. Chips were next washed with PBS then seeded with cells.

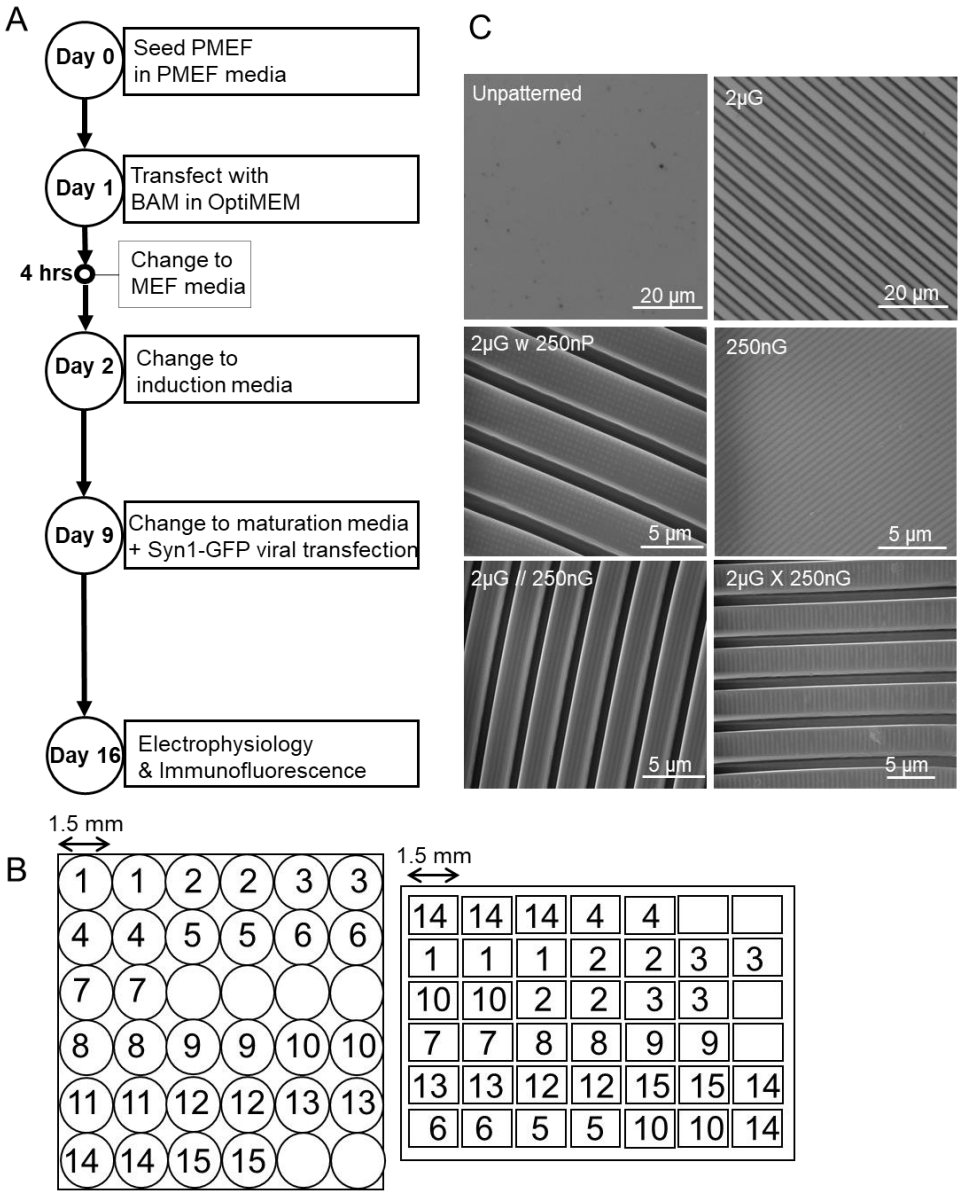

Figure 2.1 – Parameters of experiment and materials used for determining effect of topography on non-viral direct reprogramming. (A) Experimental timeline outlining key steps over the 19-day timespan. (B) Schematic of the Multi-Architecture Array Chips (MARC) used in this study, indicating pattern distribution of pattern regions and area of pattern regions. Left, circular chip and right, rectangular chip. Numerical pattern key can be found in Table 1. (C) Images of the unpatterened control (unp), and 2x2x2μm gratings (2uG), taken with the LEXT Olympus5000 microscope. Images of 250x250x250 nm gratings (250nG), 2x2x2μG with hierarchical 250 nm pillars (2μG w 250nP), 2x2x2μG with hierarchical parallel 250x250x250 nm gratings (2μG // 250nG) and 2x2x2μG with hierarchical with perpendicular 250x250x250 nm gratings (2μG ∟ 250nG) taken with scanning electron microscopy (SEM).

Table 2.1 – Pattern descriptions, pattern shorthand, and numerical key for screening the effect of topography on non-viral neuronal differentiation.

No. in Figure 2.1B	Pattern	Description
	Unp	Unpatterned control
1	2uG	2um width, 2um space, 2um height gratings
2	1x2uG	1um width, 2um space, 120nm depth gratings
3	2x1uG	2um width, 1um space, 80nm depth gratings
4	250x250x150nG	250nm width, 250nm space, 150nm depth gratings
5	1uH	1um holes, 6.5um pitch, 1um depth
6	2uP	2um diameter, 12um pitch, 2um height pillars
7	2uG ∟ 250nG	2x2x2 µm gratings with perpendicular 250x250x250 nm hierarchical gratings
8	2uG // 250nG	2x2x2 µm gratings with parallel 250x250x250 nm hierarchical gratings
9	2uG w 250nP	2x2x2 µm gratings with 250x250x250 nm pillars
10	250nP	250nm diameter, 400um pitch, 250nm height pillars
11	250nG	250nm width, 250nm space, 250nm depth gratings
12	1uL convex	1um pitch, 300nm sag microlens, convex
13	1uL concave	1um pitch, 300nm sag microlens, concave
14	1.8uL convex	1.8um diameter, 2um pitch, 700nm sag microlens, convex
15	1.8uL concave	1.8um diameter, 2um pitch, 700nm sag microlens, concave

2.2.5. Cell Culture and Transfection

Primary mouse embryonic fibroblasts (PMEF) (ATCC) between passage two and four were used for all experiments. Cells were expanded from a seeding density of 20,000 cells/cm^2 in a TCPS T25 flask. Cells were incubated at 37 °C and 5% CO_2 in complete PMEF medium: Dulbecco's Modified Eagle's Medium, high glucose with L-glutamine and phenol red (GIBCO 11965092) (Invitrogen), 15% (v/v) fetal bovine serum (Invitrogen), and 1% (v/v) penicillin streptomycin (Invitrogen). Half of the media was changed every other day. After expansion, PMEFs were seeded at a density of 20,000 cells/cm^2 onto substrates. After 24 hrs, PMEFs were transfected with p(CBA-ABOL)/DNA nanocomplexes containing either pUNO-BAM cocktails or pmax-GFP plasmid. All transfections were carried out in serum- and antibiotic-free OptiMEM (Invitrogen) media. OptiMEM was replaced with complete PMEF medium four hours after the onset of transfection. After 24 hours, PMEF medium was replaced with neuronal induction medium containing: DMEM/F-12 (Invitrogen), 1% Glutamax 100X (Invitrogen), 1% penicillin streptomycin 100X (Invitrogen), 1% N2 Supplement 100X (Invitrogen), 2% B27 Supplement 50X (Invitrogen). A supplement of bFGF (Invitrogen) at final concentration of 5 ng/ml was added daily. Two-thirds of media was changed every other day. After seven days in induction media, on day 9, the media was changed to maturation media containing: a 1:1 ratio of DMEM/F-12 (Invitrogen) and Neurobasal medium (Invitrogen), 1% Glutamax 100X (Invitrogen), 1% penicillin streptomycin 100X (Invitrogen), 0.25% N2 Supplement 100X (Invitrogen), 2% B27 Supplement 50X (Invitrogen). Growth factors were discontinued from this point onwards. Also on day 9, cells were transduced with the synpasin1-GFP reporter lentivirus, pLV-hSyn1-eGFP, at a concentration of 0.5 µL virus concentrate/cm^2. Two-thirds of media was changed every other day until day 16, when cells were fixed and stained, or electrophysiology was done. An overview of the experimental timeline can be seen in Figure 2.1A.

2.2.6. Immunofluorescence and image analysis

Cells were fixed with 4% paraformaldehyde, permeabilized with 0.25% Triton X-100 and blocked with 1% (w/v) bovine serum albumin and 10% (v/v) goat serum in 1X tris-buffered saline (TBS). Next cells were immunostained with β-tubulin III (TUJ1) (rabbit anti-TUJ1 at 1:1000, polyclonal, microtubule associated protein (MAP2) (mouse anti-microtubule associated protein at 1:600, polyclonal, Abcam) overnight at 4 ^{o}C. Samples were then washed with washing buffer composed of 0.05% triton X-100 and 1% goat serum in 1X TBS. Secondary staining was done with Alexa Fluor 488 goat anti-rabbit IgG at 1:1000 (Invitrogen) for TUJ1 and Alexa Fluor 546 goat anti-mouse IgG at 1:1000 (Invitrogen) for MAP2, overnight at 4 ^{o}C. Samples were counterstained with DAPI at 1:2200 to label nuclei for one hour at room temperature. Imaging was done using a Zeiss fluorescence microscope (Axio Observer Z1) and analyzed by manually counting the number of DAPI objects and GFP or TUJ1 positive cells.

For the first round of screening which aimed to determine the transfection efficiency on various patterns, transfection efficiency for the i_{th} pattern, T_i, was calculated as,

$$T_i = \frac{GFP\ positive\ cells\ on\ pattern\ i}{total\ cells\ on\ pattern\ i}$$

and then averaged across biological replicates. For the second round of screening which aimed to determine the reprogramming efficiency on various patterns, induced neurons were considered to be any cell that expressed TUJ1. The fraction of induced neurons for the i_{th} pattern, N_i, was calculated as,

$$N_i = \frac{TUJ1\ positive\ cells\ on\ pattern\ i}{total\ cells\ on\ pattern\ i}$$

These values were then converted to reprogramming efficiency for each pattern, R_i, as follows,

$$R_i = \frac{N_i}{(T_i)avg} = \frac{\frac{(TUJ1\ positive\ cells\ on\ pattern\ i)}{total\ cells}}{Average\ fraction\ of\ transfected\ cells\ on\ pattern\ i}$$

$$= fraction\ of\ transfected\ cells\ that\ express\ BAM$$

The reprogramming efficiency for each pattern was then normalized to the reprogramming efficiency of the control.

In single pattern studies, to determine the percentage of marker positive iN cells, the criteria outlined in Yang *et al.* was used. The criteria states that for a cell to be considered an iN it needs to express a neuronal marker and have distinct neuronal morphology. Distinct neuronal morphology is defined as a round soma with at least one thin protruding neurite.[52] Cells expressed a marker but had fibroblastic morphology were considered failed iN cells and thus were not included in the count of marker positive iN cells in single pattern studies. An example of a failed iN compared to a successful iN can be seen in Figure 2.2. Cells were counted manually. The ImageJ plugin NeuriteJ was used for measuring neurite length by tracing neurite length semi-manually. [147]

2.2.7. Electrophysiology

Cells were identified for patch clamp analysis by synapsin-1 promoter-driven GFP expression after 16 days in culture as described in section 2.5. Cells were visualized and patched using the Axon Multiclamp 700B Microelectrode Amplifier (Molecular Devices, Sunnyvale, CA). The micropipettes used for clamping in this system had a resistance of 4-8 MΩ. The cells were perfused with 50 mM HEPES buffer. Giga-ohm membrane seals were formed under voltage-clamp conditions. Whole-cell current-clamp was done using stepwise increments of 20 pA, starting at −20 pA up to 160 pA for 1 second. Whole-cell voltage-clamp was done using stepwise increments of 5 mV starting at -60 mV up to 40 mV. Spontaneous synaptic currents were recorded

in the interim between voltage steps at the resting membrane potential of the neurons. Analysis was done using Clampfit (Molecular Devices).

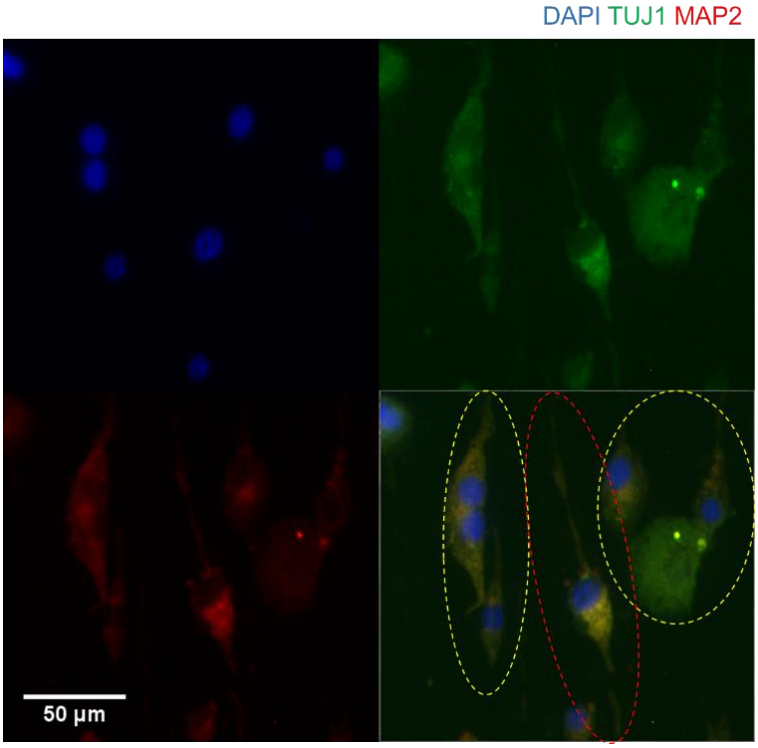

Figure 2.2 – A representative image showing the morphology of failed reprogramming and successful reprogramming. The dashed-yellow outlines indicate cells that expressed neuronal markers but maintained fibroblastic morphology and thus they were classified as failing to reprogram. The dashed-red outlines indicate a cell that was considered to be successfully reprogrammed. It expresses neuronal markers and has the distinct neuronal morphology of a round soma with protruding extensions.

2.2.8. Statistical Analysis

Data is presented as the mean and standard deviation (SD). Data analysis was performed using one-way analysis of variance (ANOVA), followed by post-hoc Dunnett's test for multiple comparisons. The student's t-test was used to calculate p-values. p values of < 0.05 were considered statistically significant. The Spearman correlation coefficient, *r*, was used to gauge

correlation strength and direction between parameters. For the screening experiments, a biological replica is one MARC. Each MARC contains two to three pattern regions (technical replica) per pattern per sample. Two images were taken of each of the two to three pattern regions per pattern. For the single pattern experiments, a biological replica was a single PDMS sample (approximately 1 cm^2). Four to seven images were captured per sample per replica. In total approximately 700 to 1200 cells were analyzed per sample per replica. For neurite length analysis on single patterns, approximately 25-100 cells were measured for each group. Counting varied depending on the number of cells available.

2.3. Results

2.3.1. Effect of substrate topography on non-viral transfection efficiency

To screen patterns that may affect the non-viral delivery aspect of neuronal reprogramming, we used GFP as a reporter of transfection. Using p(ABOL) polyplexes, 0.25 $\mu g/cm^2$ doses of pmax-GFP were delivered to PMEF cells seeded on PDMS MARC chips. Using image cytometry, it was found that there were no statistically significant differences in the percentage of GFP+ cells on the different patterns. Most patterns seemed to perform comparatively well to each other and the unpatterned blank (Figure 2.3). Patterns were classified by feature size and orientation to determine if any correlations exist between feature types and transfection efficiency. Using the Spearman correlation coefficient, *r*, moderate positive correlations between %-GFP+ cells and anisotropic patterns (R = 0.27), and %-GFP+ cells and hierarchical patterns (R = 0.33) were observed. A moderate negative correlation between %-GFP+ cells and isotropic patterns (R = -0.41) was also observed. There was no notable correlation between %-GFP+ cells and nano- or microscale features.

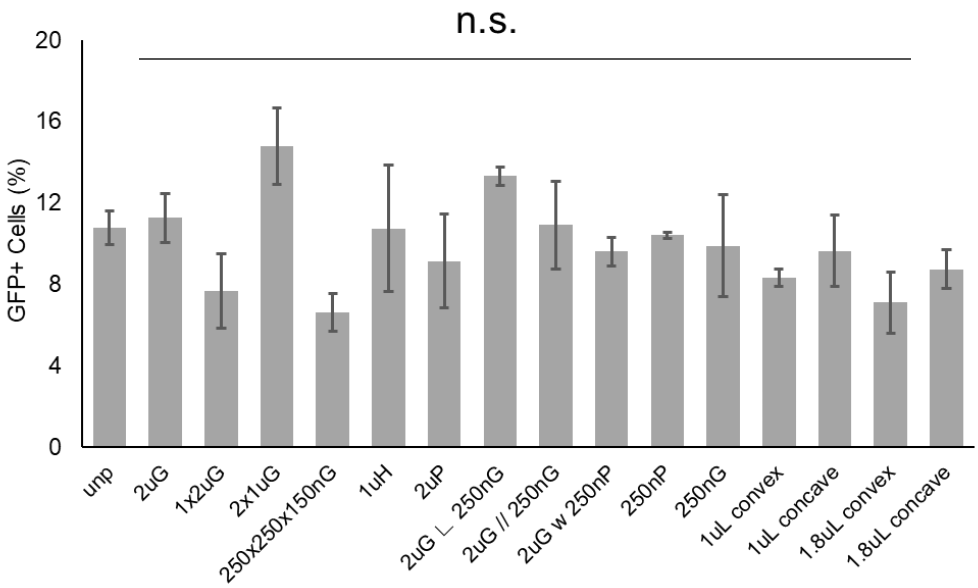

Figure 2.3 - Effect of topography on pABOL polyplex GFP transfection efficiency. Data shown as average of N=2 biological replica (each with 2-3 technical replicas) with standard error mean (SEM).

2.3.2. Effect of substrate topography on non-viral neuronal cellular reprogramming efficiency

Next, we screened the patterns for those that may affect the reprogramming efficiency, which would be quantified by the percentage of cells that become iN after one dose. After transfection, cells were allowed to mature for two weeks and were then stained for TUJ1, a pan neuronal cytoskeletal marker. The percentage of TUJ1-postive (TUJ1+) cells on each pattern was determined using image cytometry as isolation of cells from patterns for qPCR was not feasible. PMEFs cultured on the unpatterned controls were converted to TUJ1+ cells at a rate of 0.8% ± 0.4%. Figure 2.4A shows morphology and fraction of TUJ1+ cells on each of the 15 patterns screened and the unpatterned control.

To separate the effects of patterns on transfection efficiency and reprogramming efficiency, patterns were compared using a fold change normalized to GFP transfection efficiency (see section 2.2.6 for explanation of calculations). Most patterns did not affect neuronal

reprogramming efficiency. However, we were able to identify three patterns that significantly improved neuronal reprogramming efficiency (Figure 2.4B). These patterns included 2 μm lines with hierarchical perpendicular 250 nm lines (2μG ∟250nG), 2 μm lines with hierarchical parallel 250 nm lines (2μG // 250nG), and 2 μm lines with hierarchical 250 nm pillars (2μG w 250nP) ($p=0.038$, $p=0.016$, and $p=0.002$, respectively). All these patterns yielded at least twofold improvement compared to the reprogramming efficiency of the control. We were also able to see cells with distinct neuronal morphology on these patterns, to further confirm iN reprogramming (Figure 2.4A). Interestingly, isolation of the components of the hierarchical patterns (2μG, 250nG, and 250nP) did not yield notable changes in reprogramming efficiency.

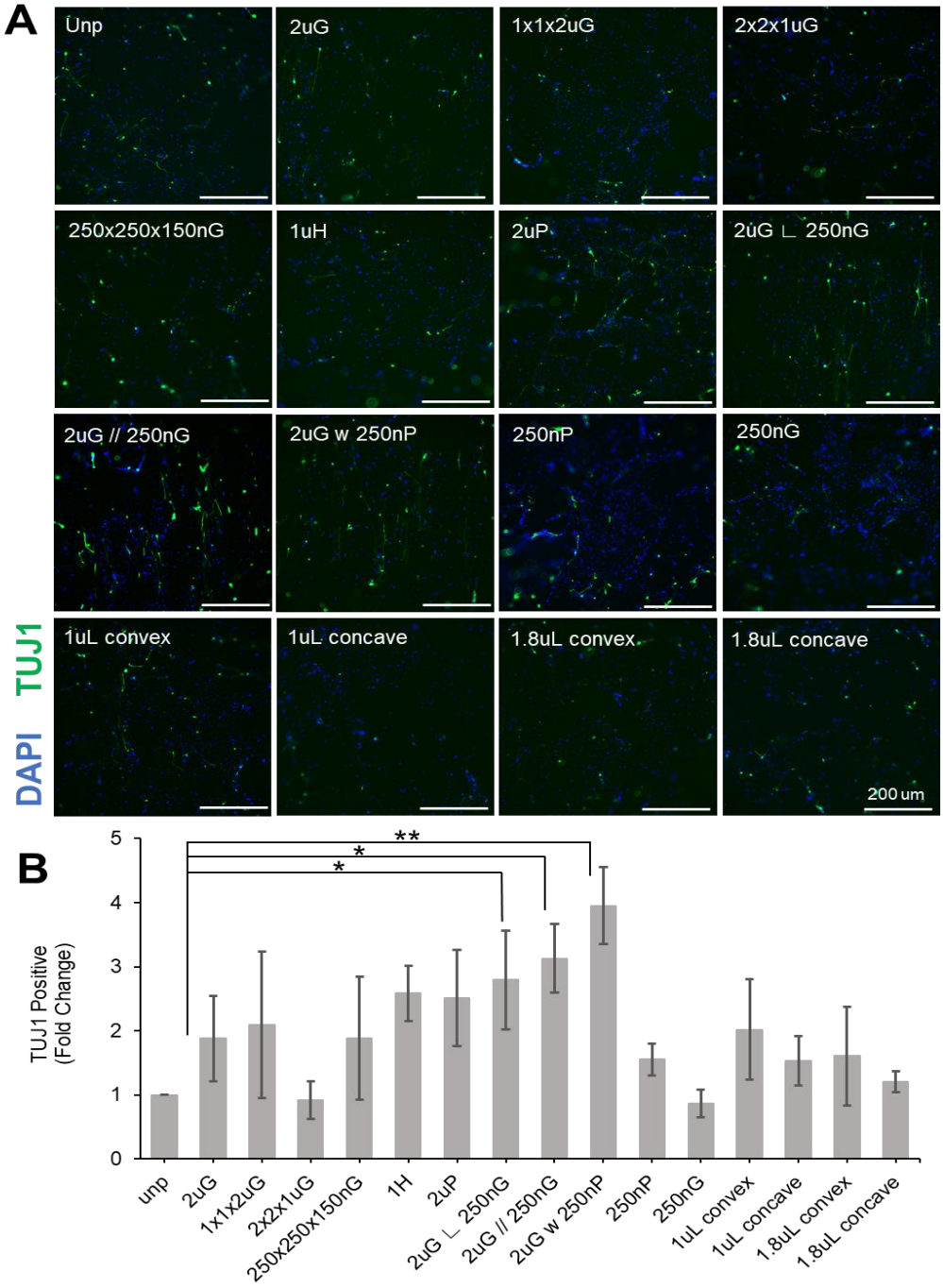

Figure 2.4 – Screening of topographies on the MARC to determine if any can enhance neuronal reprogramming efficiency using pABOL polyplex. (A) Representative images of induced neuronal (iN) cells stained with beta tubulin III (TUJ1) and DAPI on MARC topographies. All scale bars are 200µm. (B) Quantification of the generation of TUJ1+ cells on distinct MARC patterns following normalization to the transfection efficiency measured for each pattern. Data are shown as average of N=5 biological replica (each with 2-3 technical replicas) with SEM. (*, p≤0.05, ***, p≤0.01).

2.3.3. Effect on resulting iN cell maturity and morphology.

Paracrine signaling effects can occur when using a MARC chip for pattern screening cells as all patterns share the same pool of soluble factors. Thus, to further validate the effects of patterns of interest, they should be tested individually. Based on the results of pattern screening in section 2.3.2, three patterns were selected for further investigation: 2μG, 250nG and 250uG ∟ 250nG. The hierarchical pattern 250uG ∟ 250nG was selected as it performed significantly better than the control. The patterns 2μG and 250nG were selected as they are components of the chosen hierarchical pattern. We delivered a single 0.25 μg/cm^2 dose of pUNO-BAM factors in p(ABOL) polyplexes to PMEFs on MARC chips. After transfection, cells were allowed to mature for two weeks and were then stained for TUJ1 and MAP2.

ANOVA analysis indicated that patterns had a significant effect on both the percentage of TUJ1+ and MAP2+ iN cells (p=0.004 and p=0.013, respectively). In general, all patterns and the control had a higher amount of MAP2+ iN cells than TUJ1+ iN cells (Figure 2.5A,B). Only the hierarchical pattern, 2μG ∟ 250nG, significantly increased the percentage of TUJ1+ and MAP2+ iN cells compared to the unpatterned control (p=0.027 and p=0.007, respectively). On the 2μG ∟ 250nG pattern, 6% ± 0.3% of cells were TUJ1+ and 9% ± 0.7% of cells were MAP2+. Similar to what was observed in MARC chip screening, the isolated components of the hierarchical patterns, 2μG and 250nG, did not significantly increase the percentage of TUJ1+ and MAP2+ iN. However, while not statistically significant, the pattern 2μG tended to perform comparatively well to the hierarchical pattern. On the 2μG sample, 4% ± 0.8% of cells were TUJ1+ and 8% ± 1.5% of cells were MAP2+. The percentage of TUJ1+ and MAP2+ of 250nG was consistent with that of the control and had the most variation of all the groups. On the 250nG pattern, 2% ± 1% of cells were TUJ1+ and 3% ± 2.2% of cells were MAP2 positive. On the unpatterened control, 1% ± 0.01% of cells were TUJ1+ and 2% ± 0.5% of cells were MAP2+.

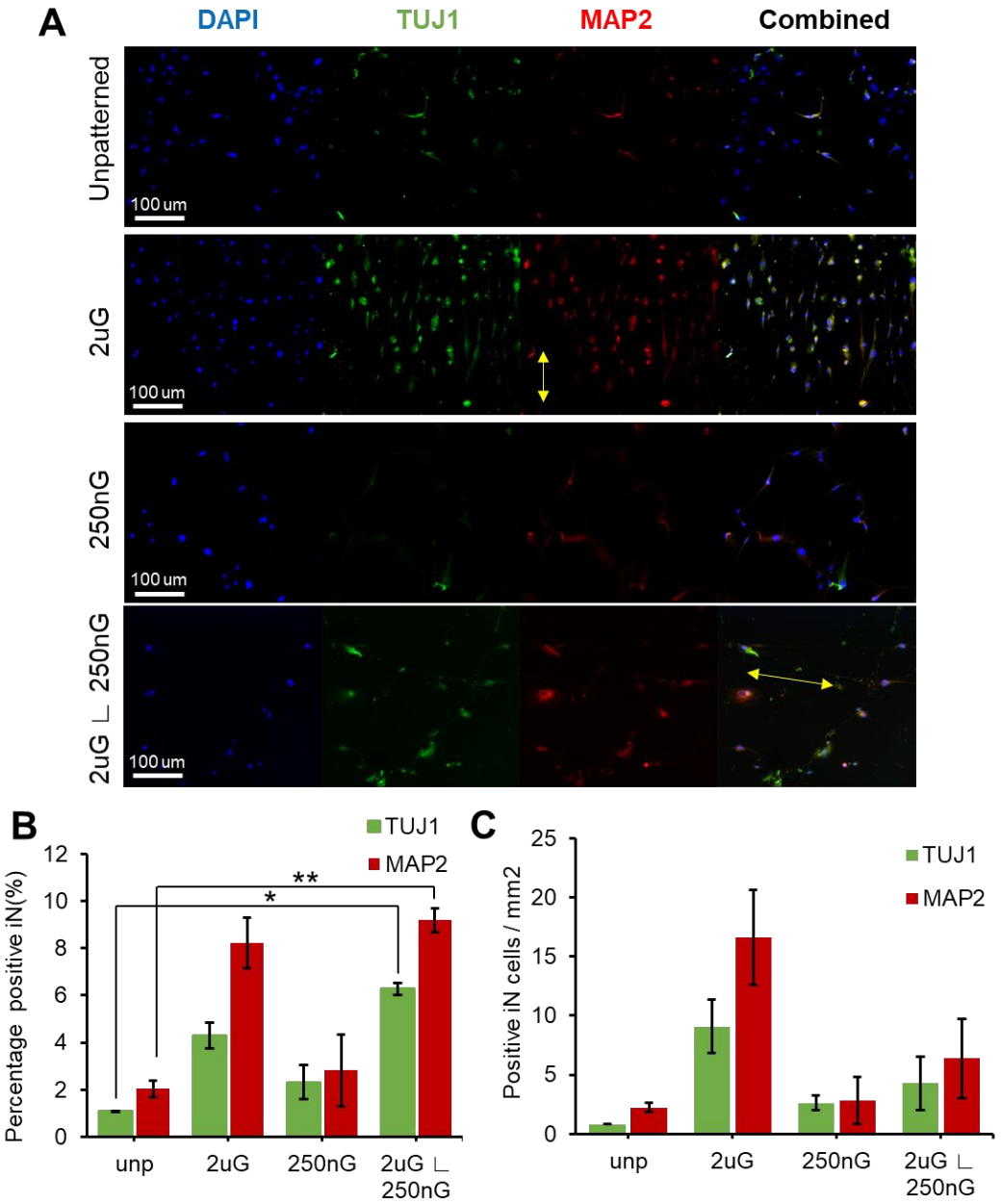

Figure 2.5 – Single pattern analysis of the effect of topography on neuronal reprogramming efficiency using pABOL polyplex. (A) Representative images of beta tubulin III (TUJ1), microtubule-associated protein 2 (MAP2) expression on the unpatterened control (unp), 2x2x2μm gratings (2uG), 250x250x250nm gratings (250nG), and 2x2x2μG with hierarchical with perpendicular 250x250x250nm gratings (2μG ∟ 250nG). Yellow arrow on 2μG image indicates direction of pattern. Yellow arrow on 2μG ∟ 250nG image indicates direction of base pattern. (B) Percentage of iN cells that express TUJ1, and MAP2, and (C) Number of cells per mm^2 of substrate that express TUJ1, and MAP2. Data shown as the average and SEM (*, $p<0.05$, **, $p < 0.01$). N=2 biological replicates, with approximately 700 to 1200 cells were analyzed per sample per replica; 4-7 images were captured at random location per sample.

Despite the hierarchical substrate having the highest percentage of TUJ1+ and MAP2+ iN cells, the highest yield of TUJ1+ and MAP2+ iN cells was found on the 2μG substrate (Figure 2.5C). The 2μG substrate on average had 9 ± 3 TUJ1+ iN cells/mm^2 and 17 ± 6 MAP2+ iN cells/mm2. The hierarchical pattern only had 4 ± 3 TUJ1+ iN cells/mm^2 and 6 ± 5 MAP2+ iN cells/mm2. The 250nG and unpatterned substrates had notably lower yields. The 250nG substrate had a yield of 3 ± 1 TUJ1+ iN cells/mm^2 and 3 ± 3 MAP2+ iN cells/mm2. The unpatterned substrate had a yield of 1 ± 0 TUJ1+ iN cells/mm^2 and 2 ± 1 MAP2+ iN cells/mm^2. However, ANOVA analysis indicated there was no statistically significant difference in the yield of marker-positive iN cells between the different substrates ($p = 0.08$ and $p = 0.06$, for TUJ1 and MAP2, respectively).

Next, we considered whether topography influenced iN morphology. ANOVA analysis indicated that patterns had a significant effect on the average neurite length ($p < 0.0001$). On 2μG samples, PMEF elongated parallel to the grooves, and iN cell neurite outgrowth aligned with the grooves (Figure 2.5A, 2.6A). The average neurite length was 44 μm ± 30 μm. On the 250 nG samples, orientation of cells relative to the grooves could not be determined but most iN cell neurites and PMEFs tended to extend in all directions (Figure 2.5A, 2.6A). Despite many cells on the 250nG pattern retaining fibroblastic morphology, those that were successfully reprogrammed had a longer average neurite length, 54 μm ± 29 μm, compared to the 2μG samples. Though, this difference was not statistically significant. A similar behavior was noted on the unpatterned control. The average neurite length on the unpatterned control was 47 μm ± 26. On the hierarchical pattern, iN cells had an average neurite length, 78 ± 49 μm, that was significantly longer than the 2μG and 250nG patterns, and the unpatterned control ($p < 0.0001$, $p = 0.0007$ and $p < 0.0001$, respectively). On the hierarchical pattern, PMEF tended to elongate parallel to the base grooves (2μG) but the neurite outgrowth of iN cells aligned both parallel and

perpendicular to the base grooves. In other words, neurites aligned with both the microgrooves and hierarchical (∟ 250nG) grooves (Figure 2.5A, 2.6A).

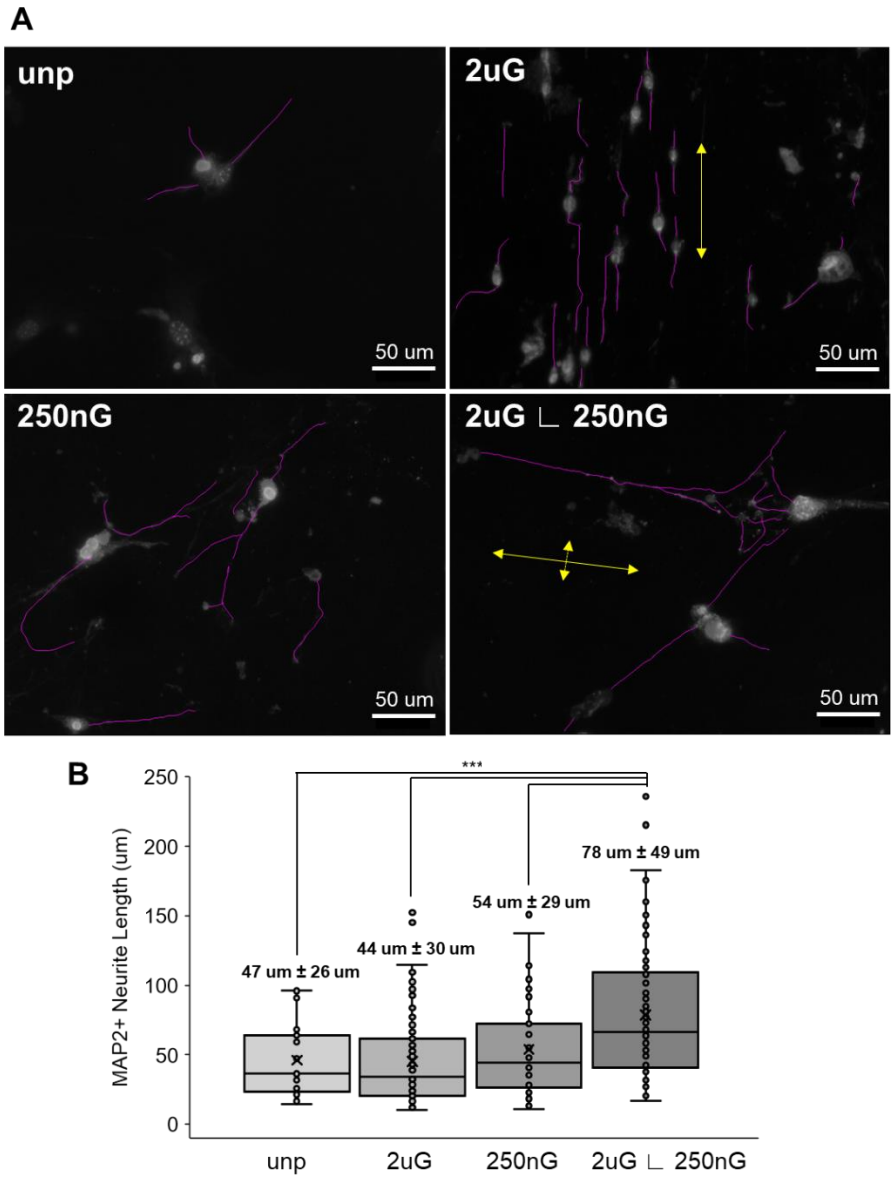

Figure 2.6 – Induced neurite length and orientation relative to patterns. (A) Representative images of iN cell morphology, neurites and orientation relative to pattern) expression on the unpatterened control (unp), 2x2x2μm gratings (2μG), 250x250x250nm gratings (250nG), and 2x2x2μG with hierarchical with perpendicular 250x250x250 nm gratings (2μG ∟ 250nG). Large yellow arrows indicate the direction of the microscale pattern and small yellow arrows indicate direction of nanoscale hierarchical pattern. (B) Distribution and average length of microtubule-associate protein 2 (MAP2) positive neurites on patterns compared to the unpatterened control. Average with 95% confidence interval labelled for each group. Data are obtained 25-100 cells were for each group, N=2 replicates. (***, $p<0.001$)

The length of neurite outgrowth was quantified by measuring approximately 25-100 MAP2+ outgrowths per pattern. The broad range of the number of outgrowths measured was due to the low reprogramming efficiency of some patterns. Quantifying the length of the neurite outgrowth of iN cells, it was found that iN cells on the hierarchical pattern, 250uG ∟ 250nG, had statistically significantly longer extensions (78 ± 49 μm) than both the individual 2μG (44 ± 30 μm) and 250nG (54 ± 29 μm) patterns, and the unpatterned control (47 ± 26 μm) ($p < 0.0001$, $p < 0.001$ and $p = 0.0007$, respectively) (Figure 2.6B). However, despite the consistent alignment of outgrowth with pattern grooves, iN cells on the 2μG pattern had the shortest average neurite length of all groups.

2.3.4. Effect on resulting iN cell functionality.

To further determine the reprogramming success on patterns and subsequent maturity of the iN cells, both voltage- and current-clamp patch clamping was performed. Voltage clamping was performed to determine how many cells on each pattern were capable of spontaneous synaptic activity and current clamping was done to determine how many cells on each pattern were capable of at least one action potential. Cells were transfected via lentivirus with an GFP driven by a Syn1 promoter to identify which cells expressed synapsin and were likely to have electrophysiological activity and thus should be patched. Two independent experiments, each measuring 3 – 12 cells per pattern, were performed.

All patterned samples had cells capable of firing at least one action potential in response to current injection but only the 250nG pattern had cells capable of firing multiple action potentials (Figure 2.7D). On the 2μG pattern, 4/11 iN cells fired at least one action potential but none fired multiple action potentials. On the 250nG pattern, 7/15 cells fired at least one action potential and

of those cells, 5/7 fired repetitive action potentials. However, these repeated spikes had much lower amplitude than the initial spike. On the hierarchical pattern, 5/15 cells fired at least one action potential, but none fired repetitive action potentials. On the unpatterned control, no action potentials could be recorded. Representative voltage plots for each substrate can be seen in Figure 6B.

Square voltage test pulses were delivered to cells, and spontaneous synaptic activity was recorded in intervals between stimuli. To differentiate between spontaneous synaptic currents and noise, a threshold of 15 pA, and a peak showing sharp rise and slow decay were used as selection criteria. Representative current plots for each substrate can be found in Figure 6A. About half of the cells tested on patterns showed spontaneous synaptic currents (Figure 2.7C). On the 2μG pattern 6/12 iN cells had spontaneous synaptic activity. On the 250nG pattern,10/19 cells had spontaneous synaptic activity. On the hierarchical pattern 5/10 cells had spontaneous synaptic activity. On the unpatterned control only 4/12 cells had spontaneous synaptic activity.

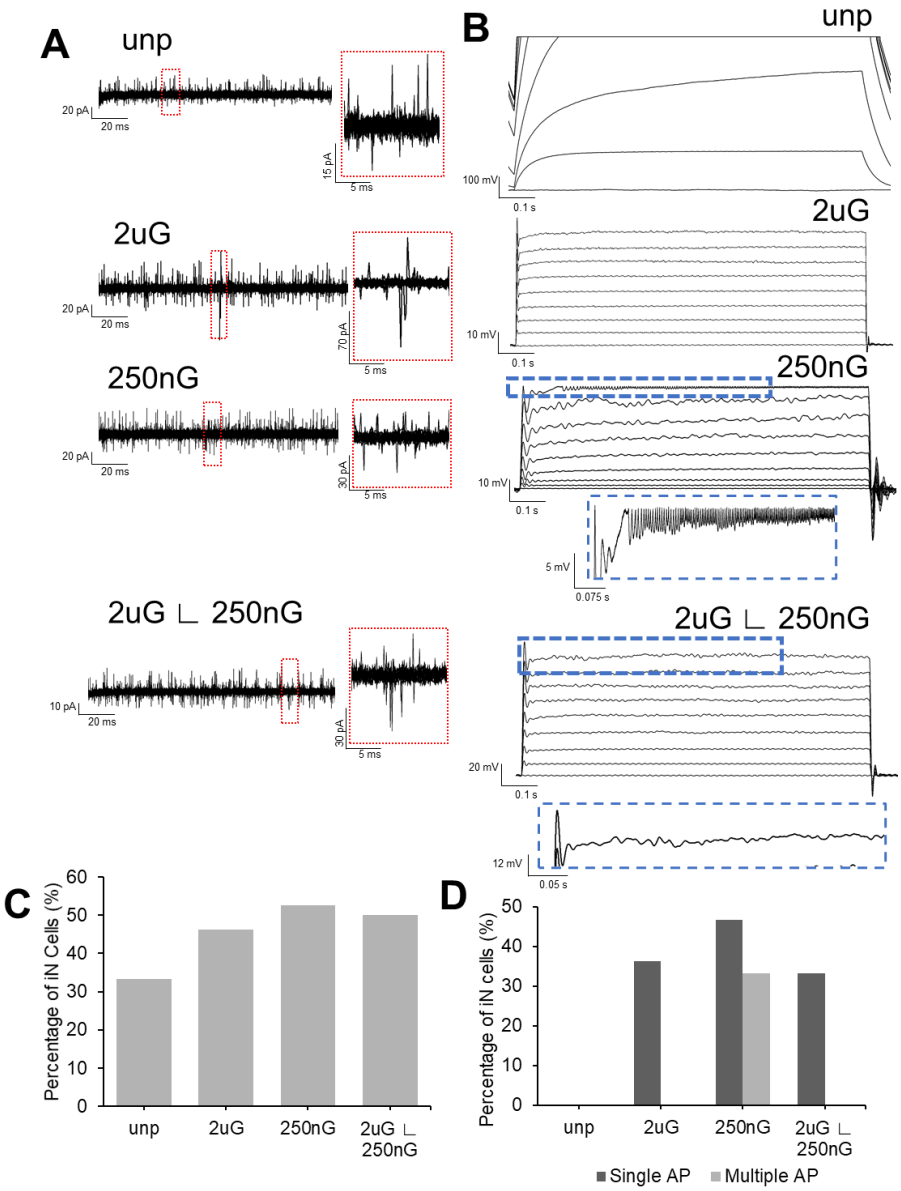

Figure 2.7 – Electrophysiological properties of induced neuronal (iN) cells on patterns compared to the unpatterened control. Representative image of (A) current profiles from voltage-clamping demonstrating evoked and spontaneous postsynaptic currents (magnified in red box) and (B) action potentials from current-clamping. Scales shown next to each plot. From top to bottom: unpatterened control (unp), 2x2x2μm gratings (2μG), 250x250x250nm gratings (250nG), and 2x2x2μG with hierarchical with perpendicular 250x250x250nm gratings (2μG ∟ 250nG). (C) Percentage of iN cells demonstrating spontaneous synaptic activity. (D) Percentage of iN cells firing a single action potential (AP) or multiple AP. Data were collected in two independent experiments from 3-12 cells per experiment.

2.4. Discussion

This study aimed to identify patterns that may enhance the direct non-viral neuronal reprogramming of PMEF via transfection with BAM factors using a bioreducible linear poly(amido amine) carrier. We hypothesized topographical patterns would enhance the efficiency of direct non-viral neuronal reprogramming. To determine which patterns, if any, affected the non-viral neuronal reprogramming, we used the multi-architecture chip (MARC) as a template on PDMS as a screening tool.[145] Using this system, we were able to screen 16 distinct patterns that contained anisotropic and/or isotropic features in the nanoscale and/or microscale. Two rounds of screening were done to better discern how topography affects neuronal reprogramming. We considered the overall process of non-viral transdifferentiation of fibroblasts to neurons to be, broadly, comprised of two main processes: (1) the delivery and uptake of BAM plasmids, and (2) neuronal reprogramming, comprised of expression of BAM genes with subsequent iN emergence and maturation. The first round of screening focused on the first process and investigated the effect of topography on transfection efficiency using a GFP reporter. The second round of screening focused on the second process and investigated the effect of topography on neuronal reprogramming efficiency. No patterns had a statistically significant effect on transfection efficiency though three patterns were shown to significantly improve neuronal reprogramming. It is important to note, however, that the first round of screening involved the uptake of only one gene (GFP). During BAM reprogramming cells must take up three plasmids and express each at sufficiently high levels for successful reprogramming.[38] The effects of topographies on transfection efficiency with the GFP reporter were minimal, but the incremental improvement seen with a one plasmid transfection could be amplified when three plasmids are used.

The significant difference in the fold change of TUJ1+ positive cells on certain patterns in the second round of screening implies that topographies affect the second step of neuronal reprogramming, more than the first. A fold change and normalization to transfection efficiency

was used in the second round of screening to decouple the reprogramming effect from any transfection effects. It should be noted though, on occasion TUJ1 can be expressed in cells that do not fully convert into iN cells and still have fibroblastic morphology.[143] In this round of screening only the hierarchical patterns were shown to have a significant effect on neuronal reprogramming efficiency, 2μG ∟ 250nG, 2μG // 250nG, and 2μG w 250nP). Similar to the findings of Kulangara *et al.* and most lineage-directed neuronal differentiation studies, these are anisotropic patterns. Interestingly, while the hierarchical patterns performed the best overall, their microscale base pattern and their respective nanoscale hierarchical patterns alone did not have a significant effect on iN development. This implied a cooperative or synergistic effect between the base pattern and the hierarchical pattern.

To further investigate the effect of topography on non-viral neuronal reprogramming, and the synergistic effect of hierarchical patterns, single pattern studies were performed. The 2μG ∟ 250nG hierarchical pattern was selected as it performed better than the unpatterned control in the first round of screening and resulted in a significant fold change in TUJ1+ cells in the second round of screening. The patterns, of which this hierarchical pattern is comprised of, 2μG and 250nG, were selected so we could better understand the synergistic effect observed in the screening. An unpatterned substrate was used as the control. In general, all substrates had a higher percentage of TUJ1+ cells in single pattern studies, compared to that observed during screening, perhaps due to paracrine signaling depressing pattern effects. In general, compared to the study from Adler *et al.* which used the same non-viral reprogramming system on blank substrates with various doses, patterns greatly improved neuronal reprogramming efficiency with only one dose. The unpatterned substrate with one dose from this study and the sample with one dose from Adler *et al.* performed comparatively well (0.67% TUJ1+ and 0.47% TUJ1+, respectively). The 2μG ∟ 250nG substrate with one dose in this study performed better than the five-dose sample from Adler *et al.* The 2μG sample with one dose performed comparatively well

to the five-dose sample. The 250nG sample with one dose, which showed a low percentage of TUJ1+ cells compared to other patterns in this study, still performed better than the three-dose sample from Adler *et al*.[131]

In general, all substrates showed a trend of higher yield and percentage of MAP2+ cells, compared to TUJ1+ cells on the same substrate. Though this difference was not statistically significant, it implies mature cells have been derived. During neuronal development, the expression window of TUJ1 has considerable overlap with MAP2 expression, however, the MAP2 expression window extends further.[148] The hierarchical pattern, 2μG ∟ 250nG, was the only pattern to have a significantly higher percentage of TUJ1+ and MAP2+ iN cells compared to the unpatterned substrate. However, the 2μG sample also had a high percentage of TUJ1+ and MAP2+ iN cells and had the highest average yield of TUJ1+ and MAP2+ cells per area. A high yield but non-significant change in the percentage of TUJ1+ and MAP2+ iN cells indicates that the total number of cells on this substrate was greater than that of the other substrates. While initial seeding confluency was set to 20,000 cells/cm^2 and held constant across patterns, it is evident that the 2uG pattern does have a higher density of remaining cells on day 14 (Figure 2.5) compared to the other patterns. This implies that the 2μG pattern improves cell adhesion or cell survival, but it is less efficient in reprogramming the attached cells as the 2μG ∟ 250nG pattern. There is also a chance that the 2uG pattern has improved proliferation. It is currently not clear whether iN undergo a pseudo-neural stem cell state during the transition between being a fibroblast and becoming an iN.[48, 52]

Looking at neurite length, the synergistic effect of the components of the hierarchical patterns becomes clearer. On the hierarchical pattern, cells had a significantly longer average neurite length and neurites were able to extend parallel to both the microscale base pattern and the hierarchical nanoscale pattern. In both transdifferentiation and lineage-directed differentiation, it has been shown that microscale gratings can improve the rate of neuronal marker expression,

as they help cells to elongate. By providing contact guidance cues to cells, gratings promote the elongated neuronal morphology which in turn alters focal adhesions, cytoskeletal arrangement, and subsequently gene expression. [70, 114, 134, 149-152] However, the effect of contact guidance on direct neuronal reprogramming and the mechanisms involved have been less explored. In this study, once reprogrammed, as the iN cells mature, the iN neurites could either continue to follow the base grooves or move in other directions by following the hierarchical grooves. Previous studies have shown that the effects of topography can be additive, and the optimal topography may vary during different phase of differentiation.[134, 153] Tan *et al.* showed that induced pluripotent stem cells undergoing neuronal differentiation, matured fastest when first induced on microgratings then transferred to micropillars. The secondary isotropic pattern allowed committed neurons to have more neuronal complexity by not restricting their direction of extension.[153] Studying lineage-directed neuronal differentiation, Chua *et al.* proposed shallower gratings were easier for neurites to extend which increased the number of directions in which the neurite could travel.[154] Similarly, a study by Yang *et al.*, investigating neuronal transdifferentiation of mesenchymal stem cells, showed hierarchical patterns help to reduce cell contractility and subsequently decrease nuclear localization of Yes-associated protein (YAP/TAZ), increasing neurogenesis. [155]

The results of electrophysiology analysis also support this proposed synergistic effect. Electrophysiological functioning of iN cells is one of the most important parameters to ensure proper neuronal maturation and functioning. During current clamping, when a constant current is delivered to cells and the change in cellular membrane potential is recorded, we can determine if ion channels have developed and the extent to which they are developed. An action potential generation indicates proper voltage-gated sodium channel development and functioning. Multiple action potentials further indicate regeneration capability of these sodium channels and proper orchestration between ion channgels.[52] During voltage clamping, when membrane potential is

held constant and the ionic current crossing the cell membrane is measured, we can verify if ion channels are capable of opening when presented with suitable membrane potential. If capable of opening, spontaneous synaptic activity should be recorded after a voltage pulse has been delivered. This indicates that neurotransmitter receptors have been developed.[52] Despite showing the lowest percentage and yield of neuronal marker positive cells amongst the patterns, the 250nG substrate had iN cells with the most mature electrophysiological functionalities. In addition to neuronal marker expression, the successful neuronal cellular reprogramming of PMEFs requires that the resulting iN cells display neuronal functionality.[52] Features such as the ability to generate action potentials upon depolarization and synaptic functioning indicate successful neuronal reprogramming. More mature features, such as repetitive action potentials and spontaneous synaptic currents with high amplitudes, can be used to indicate the extent of reprogramming. The 250nG substrate had the highest percentage of cells showing at least one action potential and was the only pattern to have iN cells that were capable for firing action potential trains. The 250nG pattern also had the highest percentage of cells with spontaneous synaptic activity. Thus, like what was seen in the analysis of neurite length, the 250nG pattern helped to promote cell maturation once iN cells had committed to the neuronal lineage. The 2μG substrate the 2μG ∟ 250nG substrate, had a similar percentage of cells that were able to fire action potentials. The unpatterned substrate did not have any iN cells capable of firing an action potential. This is consistent with previous studies using this non-viral carrier for neuronal reprogramming of PMEF with BAM factors, wherein three doses were required to see iN cells capable of firing action potentials. [131]

Improving neuronal reprogramming efficiency has been a major goal for nonviral neuronal reprogramming techniques, as a large quantity of cells are required for potential cell therapies. Our findings that hierarchical patterns can significantly increase the percentage of TUJ1+ and MAP2+ cells and produce mature cells capable of firing an action potential and showing

spontaneous synaptic activity, shows that patterns can enhance neuronal reprogramming efficiency *in vitro*. Further, as previously stated, this significant improvement in efficiency was seen using only one dose. Adler *et al.* showed that with five doses, efficiency could be improved to 8% reprogramming,[131] whereas we showed with a single dose on optimal topography, efficiency could be improved to 9% reprogramming. Thus, it is speculated that with multiple doses on optimal topography, efficiency could be comparable to that of virus-based protocols (2-20%).[38, 126, 127] Further studies should investigate the combination of topography with multiple doses.

Topography is low-cost, and a variety of well-developed techniques exist for imparting detailed topographies in both the micro- and nano-range on wide variety of different materials. Importantly, many techniques for patterning biocompatible materials such as hydrogels and the development of biocompatible electro-spun fibrous meshes with controllable fiber orientation have been developed. [156-159] These topographically modified substrates have been used to enhance lineage-based differentiation and transdifferentiation successfully both *in vivo*. [13, 160-162] Future studies should investigate the mechanisms behind this increased efficiency, and how they may affect transfection and subsequent reprogramming.

2.5. Conclusion

The findings of this study indicate that topography can be used to enhance nonviral BAM factor direct neuronal reprogramming of embryonic mouse fibroblasts using a polyplex carrier. By performing screening on MARC chips, we were able to select patterns that affected transfection and/or neuronal reprogramming efficiency. We found that anisotropic patterns may be able to enhance transfection efficiency, but the effect was not significant. Meanwhile, hierarchical patterns showed a significant effect on increasing neuronal reprogramming efficiency. Further investigating using single pattern studies, we speculated that the base pattern of microscale gratings could be responsible for improving initial expression of BAM factors and neuronal marker, TUJ1 and MAP2, expression in iN cells. The secondary pattern on the hierarchical pattern, the

250nG perpendicular to the base gratings, was speculated to be responsible for promoting subsequent maturation and development of iN cells. Using hierarchical patterns, we were able to increase efficiency with one dose to a level was similar to previous studies using five doses. The combination of multiple doses and topography may have the potential to produce an even more efficient system. Future optimization of patterns and dosing may be able to provide efficiencies that bring direct neuronal reprogramming closer to being clinically feasible.

CHAPTER 3

Development of a platform to test the combined effect of topography and stiffness on neuronal differentiation.

3.1. Introduction

Mechanobiology has been shown to play an important role in a wide range of developmental, physiological, and pathological processes.[163-165] Of particular interest, are the biophysical cues of microtopography and stiffness, which have been successfully applied to a wide variety of tissue engineering domains including vascular, neuronal, corneal, pulmonary, bone, kidney, and liver applications.[166-170] These cues are often studied independently, but it is of interest to see if they could be optimized to provide synergistic effects. However, there is difficulty in producing a material that can be patterned with micro topographies, has controllable stiffness and to which cells can attach for a long period of time. Especially for neuronal differentiation studies wherein cells must attach to the substrate for the differentiation period and the resulting neurons must also attach during maturation, all of which can take up to a month.

Polyacrylamide (PAA) has been widely used as a substrate for mechanobiology studies. It is easy to pattern in the micrometer range [171-175], and has stiffness that can be precisely controlled in the pascal to megapascal range.[176-179] However, for cells to attach to PAA, the conjugation of cell attachment factors, such as extracellular matrix (ECM) proteins, are required. Using the crosslinker sulfosuccinimidyl 6-(4′-azido-2′-nitrophenylamino) hexanoate (Sulfo-SANPAH) is the most common method of conjugating cell attachment factors to PAA. It is a relatively simple procedure that works with a wide variety of ECM proteins and other cell attachment factors, but it's distribution of conjugated compounds is uneven and unstable. It has been shown that cells can remove ECM conjugated by Sulfo-SANPAH which could lead to misrepresentation of rigidity-dependant cell behavior.[180] Alternative methods that rely on co-polymerization of PAA with compounds such as acrylic acid,[181, 182] N-succinimidyl ester of acrylamidohexanoic acid,[183, 184] acrylic acid N-hydroxysuccinimide,[185] N-hydroxyethylacrylamide,[186] and N-acryloyl-6-aminocaproic acid (ACA) [175, 180, 187] have been developed. These compounds introduce functional groups that allow for more stable conjugation

with carbodiimide crosslinking. The crosslinking method is compatible with a wide range of cell attachment factors are only a carboxyl group and primary amine are required. Carbodiimide crosslinking is also significantly stronger than sulfo-SANPAH and is relatively simple to implement.

Using carbodiimide crosslinking of collagen to a copolymer of polyacrylamide and N-acryloyl-6-aminocaproic acid (PAA-ACA), Yip *et al*. found that cells were not able to remove collagen from the surface. Further this controllable stiffness and are amenable to microscale patterning. Because of these excellent properties, we think it may be possible to use the PAA-ACA gel with carbodiimide ECM conjugation to study the combined effects of stiffness and topography on neuronal differentiation. For the gel to be suitable it must be easy to pattern with microtopography, have reliable stiffness in a physiologically relevant range and allow for stable adherence of mouse and human neural progenitor cells, and their differentiated progeny. To investigate this, we fabricated PAA-ACA gels with varying acrylamide and bisacrylamide ratios but constant ACA concentration. A sandwiching technique for patterning the gels with microtopographies. A variety of different cell attachment factors were tested to determine if any could be successfully conjugated with PAA-ACA and allow for long term attachment of the neural progenitor cells. Cell attachment was verified by allowing cells to adhere and differentiate for either 14 or 28 days.

3.2. Methods and Materials

3.2.1. Silanization and generation of aldehyde groups on coverslips

No.1, 12 mm diameter glass coverslips (1254581, Fisher Scientific) were cleaned by briefly submersing in ethanol and then flaming. Coverslips were then placed in 3D-printed polylactic acid holders (Model ID 3DPX-012889, NIH 3D Print Exchange) [188], and submersed in

a 0.5% (v/v) aqueous solution of (3-aminopropyl)triethoxysilane (A3648, Sigma Aldrich) for 30 min at room temperature, with occasional agitation to ensure even activation. Next, they were rinsed six times with deionized water. Excess water was blotted from the surface and coverslips will allowed to dry fully. Once dry, coverslips were then submerged into a solution of 0.5% glutaraldehyde (G5882, Sigma Aldrich) in 1X phosphate buffered saline (PBS), at room temperature for 30 min, with occasional agitation. They were then rinsed three times with deionized water. Excess water was blotted from the surface and coverslips were allowed to dry full at room temperature. Once dry, coverslips were sealed in a plastic container with calcium chloride as a desiccant to prevent humidity and stored at 4°C until used, for up to two months.

3.2.2. Hot embossing of polyethylene terephthalate

Molds made from 1:10 polydimethylsiloxane (PDMS) (184 Kit 4019862, Ellsworth Adhesives Canada) with 2 x 2 x 2 µm (height x width x spacing) gratings, 5 x 5 x 5 µm gratings or 10 x 10 x 10 µm gratings were used as master molds for hot embossing. Using a hot plate, a glass microscope slide on aluminum foil was heated to 75 ^{o}C. While temperature stabilized, a 3 cm x 3 cm piece of polyethylene terephthalate (PET) (ES301445, Goodfellow Cambridge Limited) was rinsed with ethanol and blown dry. The PET piece was then placed on the heated coverslip and allowed to soften for 10 s. The PDMS pattern mold was then placed pattern-down on top of the PET. This assembly was then covered with another microscope slide. An approximately 5 lb weight was them placed on top of the second glass slide, directly above the PDMS and PET. The weight was then held in place with a retort stand for 5 min. After this, the hot plate was turned off, and the weight was left on for another 5 min as the sample cooled. Once cooled, the entire assembly from aluminum foil up to the weight were lifted off all together and placed on the bench top and allowed to cool for another 5 min. Once at room temperature, the weight was removed

and the PDMS mold was peeled off the patterned PET. The PET pieced was then cut into 12 mm rounds and air plasma treated using 85W and 0.8 NL/h for 30 s.

3.2.3. Copolymerization of polyacrylamide and N-acryloyl-6-aminocaproic acid

A copolymer of polyacrylamide (PAA) and N-acryloyl-6-aminocaproic acid (ACA), here in referred to as PAA-ACA, was produced using free radical polymerization (Figure 3.1A) following a protocol developed by Yip *et al*.[180] A solution of 500mN N-acryloyl-6-amincaproic acid (ACA) (A1896, Tokyo Chemical Industry) was made by dissolving ACA powder in 0.35M sodium hydroxide in deionized water. This solution was then vortexed until completely dissolved and then filtered using a 0.22 µm filter. The solution was store in the fridge for up to one month. 100 mM 2-(N-morpholino)ethanesulfonic acid, 0.9% (w/v) sodium chloride (MES) buffer was made by dissolving BupH MES buffered saline packs (28390 Thermo Scientific) in deionized water. The pH was corrected to 6.1 using 5M NaOH.

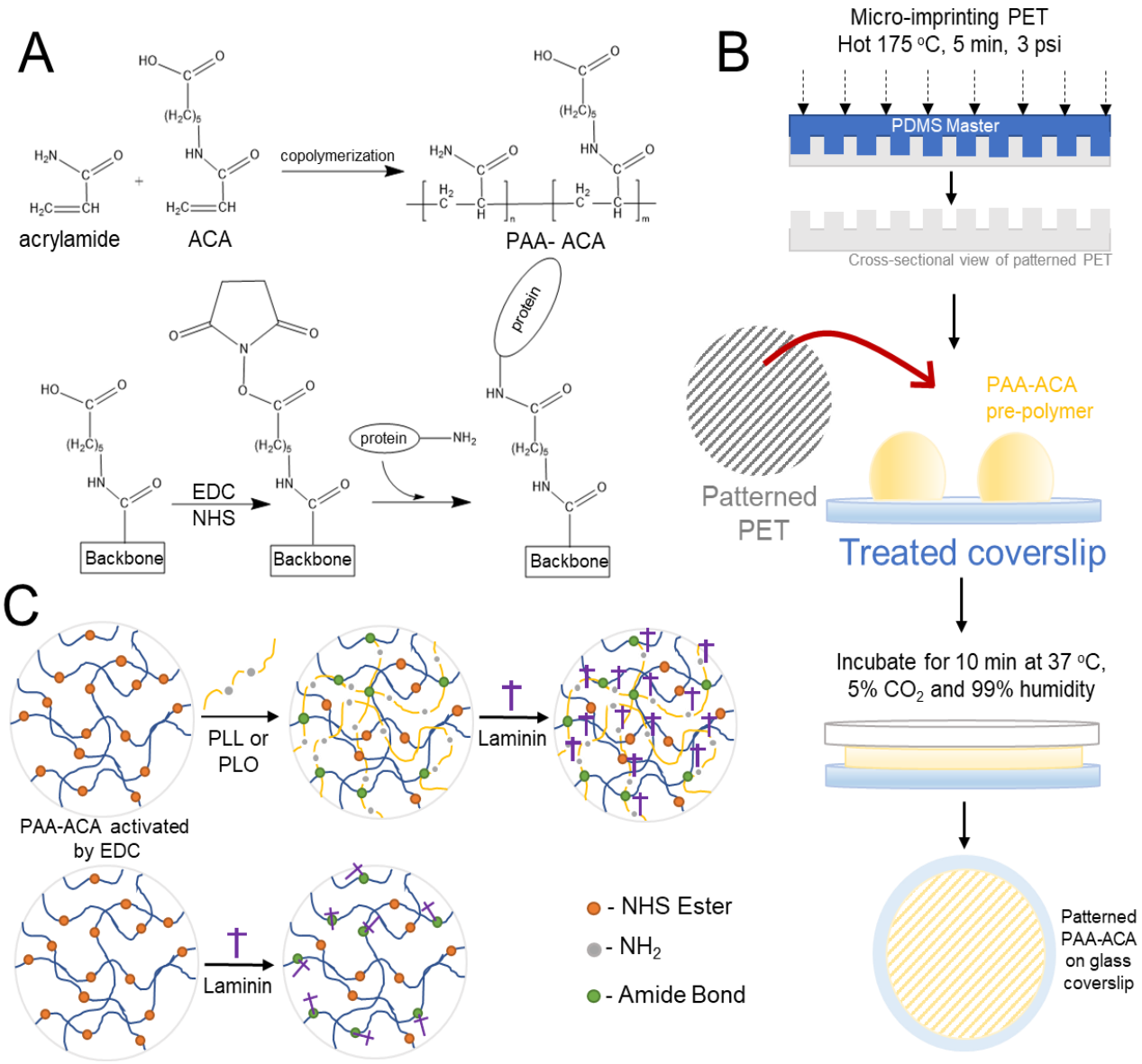

Figure 3.1. – Schematic of PAA-ACA gel fabrication and cross-linking chemistry. (A) Copolymerization of polyacrylamide and N-acryloyl-6-aminocaproic acid (PAA-ACA) followed (top) by carbodiimide chemistry used to crosslink extracellular matrix to PAA-ACA gel (bottom). Prepared using ChemDraw® a registered trademark of PerkinElmer Informatics. (B) Fabrication schematic of micropatterned PAA-ACA gels schematic. Prepared using PowerPoint® a registered trademark of Microsoft Corporation. (C) Conjugation of various laminin to PAA-ACA gel using a polypeptide intermediate (top) or directly (bottom). Prepared using PowerPoint® a registered trademark of Microsoft Corporation.

Pre-polymer solutions were prepared following the concentrations of reagents stated in Table 3.1. For the pre-polymer solution, acrylamide (161-0140, Bio Rad), bisacrylamide (161-0142 BioRad), ACA and deionized water, were combined. The pre-polymer solutions were mixed with gentle pipetting to avoid the introduction of air for 30 s. Once homogenous, aqueous tetramethlethlenediamine (TEMED) (T7025 Sigma Aldrich) was added and gently mixed into the pre-polymer solutions for 30 s. Treated coverslips were placed in a petri dish about one inch apart from each other. Next the free radical initiator, aqueous ammonium persulfate (A3678 Sigma Aldrich) was added to the pre-polymer solutions and gently mixed for 10 s. Quickly after mixing, 20 µl of pre-polymer solution was placed in two to three droplets on the treated coverslips. Embossed PET molds were placed on top to sandwich the pre-polymer solution droplets (Figure 3.1B) and then the petri dish was gently knocked on the table to ensure even solution spreading. The samples were then placed in an incubator at 37°C, 5% CO_2, 99% humidity for 10 min to fully polymerize. Once completely polymerized, the petri dish was flooded with 100 mM 2 MES buffer and the PAA-ACA gels were incubated at room temperature for at least 10 min. At this point samples were either de-molded or stored with their PET cover in 100mM MES buffer at 4 ^{o}C for up to one week. To de-mold samples, the PET mold was gently lifted from the surface. The resulting thin PAA-ACA gel remained bound to the treated coverslip.

To prepare samples for mechanical testing, instead of sandwiching droplets of pre-polymer solution between PET molds and treated coverslips, the solution was casted into a cylindrical mold. Microcentrifuge tubes with inner diameter of 5 mm, were filled with 200 µl of pre-polymer solution. Once polymerized, the ends of the tube were cut off and the samples were allowed to soak in 100 mM MES buffer. The resulting gel was then pushed out of the mold and cut as needed. Samples were stored in 100mM MES buffer at 4 ^{o}C for up to one week.

Table 3.1 – Composition of PAA-ACA gels of varying stiffness

	Stiffness			
Reagent	Very Soft	Medium Soft	Medium Stiff	Very Stiff
Acrylamide (w/v)	3.0%	4.0%	5.5%	10.0%
Bisacrylamide (w/v)	0.13%	0.17%	0.23%	0.43%
ACA (w/v)	1.85%	1.85%	1.85%	1.85%
TEMED (w/v)	0.1%	0.1%	0.1%	0.1%
APS (v/v)	0.1%	0.1%	0.1%	0.1%

3.2.4. Conjugation of polypeptides and extracellular matrix

Polypeptides and extracellular matrix (ECM) were conjugated to the thin cast PAA-ACA samples bound to treated coverslips to promote cell adhesion. Samples were rinsed three times with MES buffer. In MES buffer, samples were then sterilized with ultraviolet light in a biosafety cabinet for 30 min. In the meantime, a 0.5 M N-hydroxysuccinimide (NHS) (130672, Sigma Aldrich) and 0.2 M N-(3-Dimethylaminopropyl)-N′-ethylcarbodiimide hydrochloride (EDC) (221465, Sigma Aldrich) solution in MES buffer was prepared and kept cold until use. This solution was prepared fresh every time. After sterilization, the carboxyl groups of the PAA-ACA were activated using with excess EDC/NHA to convert all carboxyl groups of the PAA-ACA to NHS esters (Figure 3.1A). Samples were submersed in the 0.5 M NHS/0.2 M EDC solution, and incubated at room temperature for 30 min on a rocker. Samples were briefly rinsed three times with 1X PBS to removed unreacted EDC/NHS. Next samples were incubated with either poly-L-ornithine hydrobromide, mol 30,000 – 70,000 (PLO) (P4957 Sigma Aldrich) diluted to 0.07 mg/ml in 1X PBS or poly-l-lysine hydrobromide, mol 30,000 – 70,000 (PLL) (P2636, Sigma Aldrich) diluted to 0.5 mg/ml in 1X PBS to form amide linkages. In a 24-well plate, samples were incubated in 0.5 ml polypeptide solutions for 2 hr at room temperature. Samples were rinsed with 1X PBS

for 15 min, three times. Next, ECM was bound to the surface of the samples via electrostatic interactions (Figure 3.1C). Samples were placed in either a solution of 20 µg/ml Englebreth-Holm-Swarm sarcoma (EHS) mouse laminin (354232, Corning) in 1X PBS, or a solution of 20 µg/ml EHS mouse laminin and 1 mg/ml heparin sulfate in 1X PBS. The heparin-laminin solution was allowed to rest at least two hours in 4 ^{o}C prior to use to ensure the laminin and heparin had time to react. Samples were incubated in ECM solution for 2 hr in the incubator (37 ^{o}C, 5% CO_2 and 99% humidity). Samples were washed once with 1X PBS and either used immediately or stored in 1X PBS at 4 ^{o}C for up to one week. Before use samples were allowed to soak in DMEM/F12 media for 30 min in the incubator.

An alternative protocol, that crosslinked laminin to the surface of the gels was also considered. In this method, after activating the gels with carbodiimide chemistry and washing, the gels were directly incubated 20 µg/ml EHS mouse laminin in 1X PBS, rather than one of the polypeptides. Samples incubated in the laminin solution for 2 hr in the incubator (37 ^{o}C, 5% CO_2 and 99% humidity). Samples were then washed once with 1X PBS and either used immediately or stored in 1X PBS at 4 ^{o}C for up to one week. To visualize laminin attachment, a 1:5 ratio of HiLyte488 green fluorescent laminin (LMN02, Cytoskeleton Inc.) and EHS laminin was used.

3.2.5. Mechanical characterization

A MicroTester (CellScale) was used to measure to the compressive Young's modulus of cylindrical PAA-ACA samples. Cylindrical PAA-ACA samples had a diameter of 5 mm and were cut to 4 – 6 mm in height using a scalpel. A microbeam of stiffness 1.0160 MPa (as reported by CellScale) with a 6 mm x 6mm platen glued to the end was used. The platen completely covered the top of the cylindrical sample. The test was performed in a bath of 1X PBS at 37 ^{o}C. Samples equilibrated in the bath for 5 min before testing. Once equilibrated, the platen was lowered so it

just touched the top of the sample (Figure 3.2A). No pre-load was applied. The sample was compressed at a rate of 5 μm/s until approximately 30% strain was achieved. The platen was then raised at a rate of 5 μm/s until returning to its starting position. The Young's modulus was determined by plotting stress versus strain plots and finding the slope of linear region that directly followed the toe and heel regions. Five samples of each gel rigidity were used for measurement.

3.2.6. Optical profilometry

To verify surface patterning, optical profilometry of PAA-ACA thin gel samples was performed using the LEXT OLS5000 3D Laser Scanning Microscope (Olympus). Fully hydrated samples were used for imaging. Water on the surface of the samples was remove by blow drying and then samples were immediately imaged. Using the stiffest sample group, surface topography profiles were generated using the fine laser scanning mode. Three replicates of each pattern and 10 – 12 measurements per replicate were used to calculate average dimensions.

3.2.7. Cell adhesion

Cell adhesion to the polymer surface was confirmed by using seeding primary mouse neural progenitor cells (mNPC) at a density of 20,000 cells/cm^2 on thin gel PAA-ACA samples in mouse maintenance media (Table 3.2). The primary mNPC were a gift from Dr. Eyleen Goh's lab at the National University of Singapore. Their isolation protocol can be found in Shivaraj *et al.*[189] Mouse maintenance was comprised of a basal media comprised of 1:1 Dulbecco's modified eagle medium and Ham's F12 medium with added L-glutamine and HEPES buffer without sodium bicarbonate (DMEM/F12) (11330032, Gibco), penicillin-streptomycin (LS15070063, Gibco), and N2 supplement (17502048, Gibco). A daily supplement of recombinant human fibroblastic growth

factor (bFGF) (Gibco PHG0021) and recombinant human epidermal growth factor (EGF) (Gibco PHG0311) was added also added. Concentrations of media components can be found in Table 3.2. Samples were then put in an incubator at 37 ^{o}C, 5% CO_2 and 99% humidity. After 24 hr, cell adhesion was assessed using brightfield microscopy. In the wells that had viable cells, media was changed to mouse induction media to induce differentiation (Table 3.2) and half the media was changed every other day. After seven days, media was changed to mouse maturation media (Table 3.2) and cells incubated for another seven days. The total differentiation time for the mNPC was 14 days.

Adhesion of induced pluripotent stem cell (iPSC) derived human neural progenitor cells (hNPC) was also tested. Similar to mNPC, hNPC were seeded at 20,000 cells/cm^2 or 5,000 cells/cm^2 in human maintenance media with 5 µm of the ROCK inhibitor Y-26732 (1254/1, BioTechne). Samples were then put in an incubator at 37 ^{o}C, 5% CO_2 and 99% humidity. After 24 hr, cell adhesion was assessed using brightfield microscopy. Media was changed to human differentiation media and half the media was changed every two to three days. The total differentiation time for the hNPC was 28 days.

After 14 days for the mNPC and 28 days for the hNPC, respectively, cells were fixed with 4% paraformaldehyde, permeabilized with 0.25% Triton X-100 and blocked with 1% (w/v) bovine serum albumin and 10% (v/v) goat serum in 1X tris-buffered saline (TBS) overnight at 4 ^{o}C. Next cells were immunostained with β-tubulin III (TUJ1) (rabbit anti-TUJ1 at 1:600, polyclonal, Sigma Aldrich), microtubule associated protein (MAP2) (mouse anti-microtubule associated protein at 1:600, polyclonal, Abcam) overnight at 4 ^{o}C. Samples were then washed with washing buffer composed of 0.05% triton X-100 and 1% goat serum in 1X TBS. Secondary staining was done with Alexa Fluor 488 goat anti-rabbit IgG at 1:1000 (Invitrogen) for TUJ1 and Alexa Fluor 546 goat anti-mouse IgG at 1:1000 (Invitrogen) for MAP2, overnight at 4 ^{o}C. Samples were counterstained

with DAPI at 1:2200 to label nuclei for one hour at room temperature. Imaging was done using a fluorescence microscope (Axio Observer Z1, Zeiss GmBH) and analyzed using ImageJ software.

Table 3.2 – Media used for mouse neural progenitor cells

	Volume/50 ml media (Final Concentration)		
	Maintenance Media	Induction Media	Maturation Media
DMEM-F12 medium	49 ml	47.5 ml	24 ml
Neurobasal medium	--	--	24ml
Glutamax (100X)	--	0.5 ml (1X)	0.5 ml (1X)
Penicillin/streptomycin (100X)	0.5 ml (1X)	0.5 ml (1X)	0.5 ml (1X)
N2 supplement (100X)	0.5 ml (1X)	0.5 ml (1X)	0.125 ml (0.25X)
B27 supplement (50X)	--	1 ml (1X)	1 ml (1X)
Daily supplement	EGF (20 ng/ml) FGF (20 ng/ml)	FGF (5 ng/ml)	--

Table 3.3 – Media used for human neural progenitor cells

	Volume/ 50 ml media (Final Concentration)	
	Maintenance Media	Differentiation Media
DMEM-F12 medium	23.5 ml	24 ml
Neurobasal medium	23.5 ml	24 ml
N2 supplement (100X)	0.5 ml (1X)	0.5 ml (1X)
B27 supplement (50X)	1 ml (1X)	1 ml (1X)
L-glutamine (100X)	0.5 ml (1X)	0.5 ml (1X)
Penicillin/streptomycin (100X)	0.5 ml (1X)	0.5 ml (1X)
Bovine serum albumin (5 mg/ml)	50 µl (5 µg/ml)	--
Human LIF (10 µg/ml)	50 µl (10 ng/ml)	--
CHIR99021 (0.8 mM)	187.5 µl (3 µm)	--
SB431542 (10 mM)	10 µl (2 µm)	--

3.2.8. Statistics

Statistical analysis was done using one-way analysis of variance (ANOVA) in Excel with an alpha of 0.05. If the results of ANOVA were determined to be significant, Tukey's post-hoc test was used to determine which samples differed from one another. All confidence intervals are reported with a 95% confidence level. The number of replicas used for each test are denoted in the figure legends.

3.3. Results

3.3.1. Physical characterization of PAA-ACA gels

The produced PAA-ACA gels were completely transparent. The thin gel samples bound to the glass coverslip had an average height of 196.20 μm ± 13.86 μm. Gels remained bound to the coverslips for the entire cell culture period.

Using a compressive uniaxial test, the Young's moduli of the PAA-ACA gels were found to be significantly distinct from one another, and consistent across replica. The average Young's moduli at 37 ^{o}C, for the 3.0%A/0.13%B, 4.0%A/0.17%B, 5.5%A/0.23%B, and 10.0%A/0.43%B gels fully hydrated in 1X PBS were 6.1 ± 0.6 kPa, 12.9 ± 2.5 kPa, 22.9 ± 3.2 kPa, and 92.6 ± 4.9 kPa, respectively (reported as 95% CI) (Figure 3.2C). The gels were significantly distinct from one another (ANOVA, p-value < 0.0001) and none of their confidence intervals overlapped. The stress strain curves for each of the gel stiffnesses were shaped like the stress-strain curves of soft tissue, with a toe region followed by a linear region. The stress-strain curves for each gel stiffness show that the compression and recovery curves track each other quite closely (Figure 3.2B), indicating that like polyacrylamide gels, PAA-ACA copolymer gels are purely elastic. Using the PET moulds and following a method similar to that of Yip *et al.*, microgratings were successfully printed on the

6.1 kPa, 12.9 kPa, 22.9 kPa and 92.6 kPa gels (Figure 3.3). Gratings of three different dimensions were imparted: 2 x 2 x 2 μm (height x length x spacing) (2uG), 5 x 5 x 5 μm (5uG), and 10 x 10 x 10 μm (10uG).

Using the stiffest gel (92.6 kPa), the dimensions of the imparted gratings were confirmed using laser scanning optical profilometry. The dimensions for the 2uG pattern were determined to be 2.03 ± 0.12 μm height x 1.85 ± 0.19 μm width x 2.13 ± 0.15 μm spacing. The dimensions for the 5uG pattern were determined to be 5.64 ± 0.21 μm height x 5.31 ± 0.27 μm width x 5.02 ± 0.28 μm spacing. The dimensions for the 10uG pattern were determined to be 10.05 ± 0.65 μm height x 10.21 ± 0.40 μm width x 10.51 ± 0.49 μm spacing.

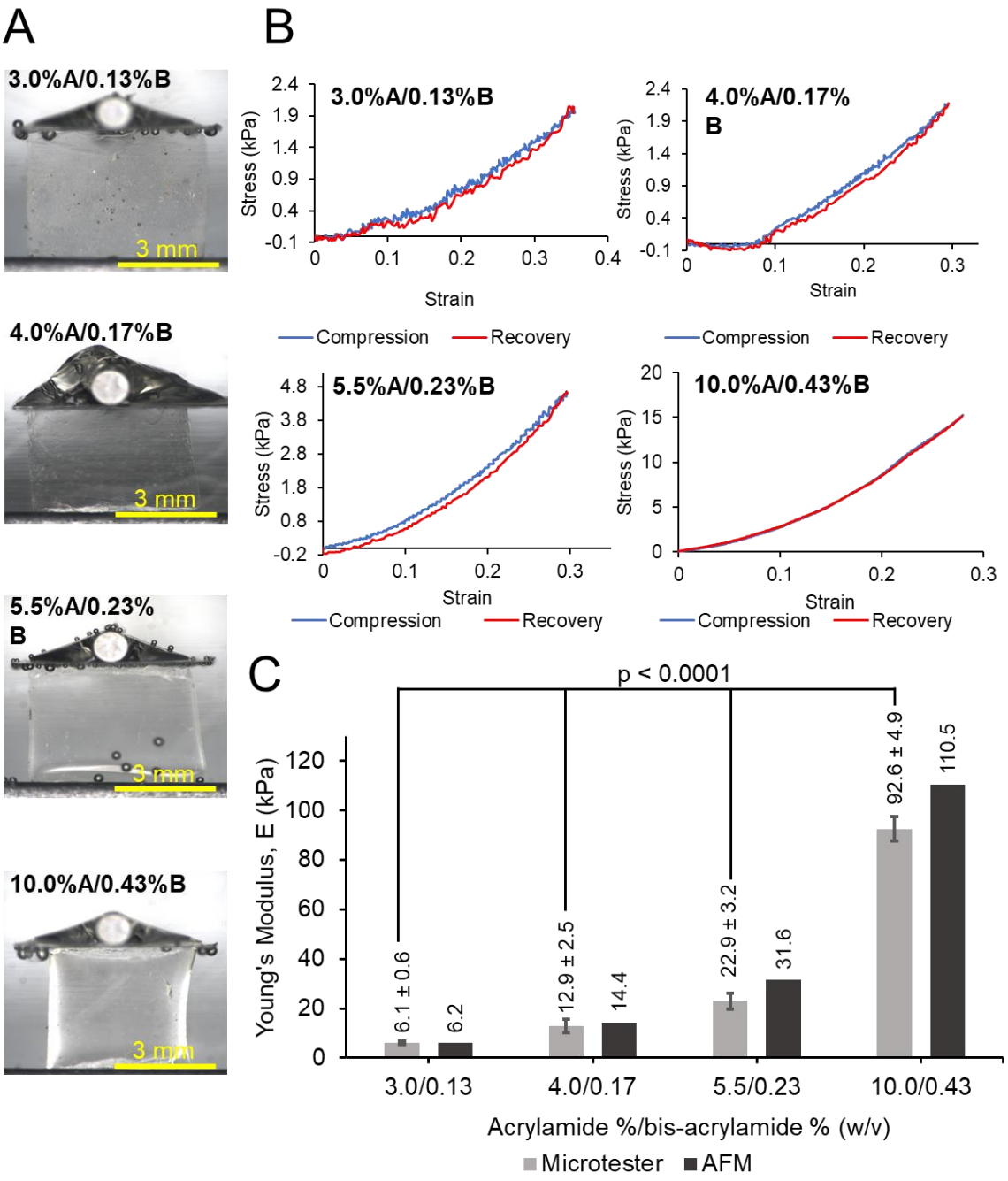

Figure 3.2 – Mechanical characterization of polyacrylamide- N-acryloyl-6-aminocaproic acid (PAA-ACA) hydrogels. (A) Representative images of mechanical testing starting conditions and samples. (B) Stress versus strain curves for samples for various ratios of acrylamide and bis-acrylamide. (C) Young's modulus measured with the Microtester and AFM for various ratios of acrylamide and bis-acrylamide. AFM measurements were obtained from Yip *et al.* [65]

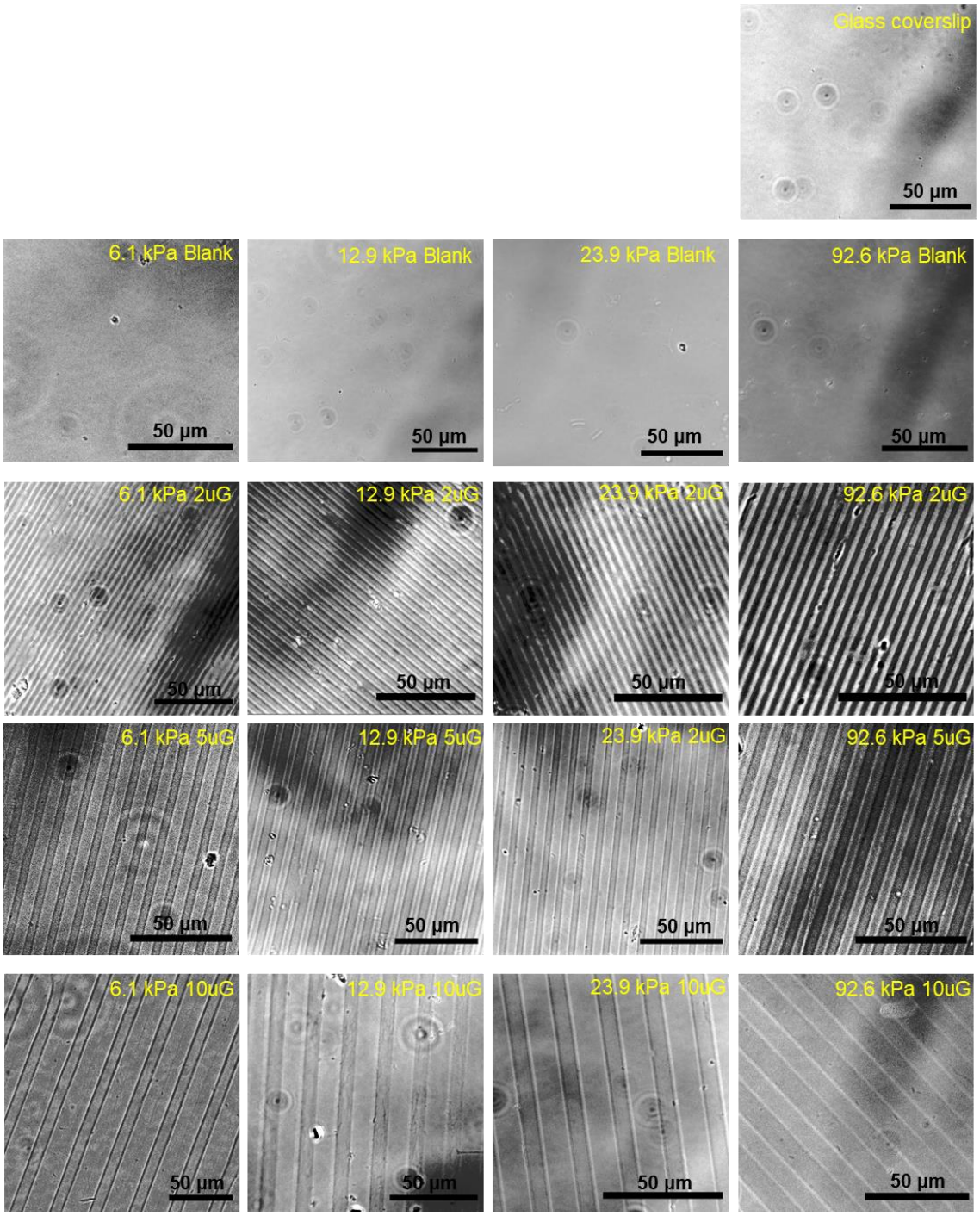

Figure 3.3 – Representative images of patterns on polyacrylamide- N-acryloyl-6-aminocaproic acid (PAA-ACA) hydrogels. Young's modulus and topography are labelled in the top right corner for each image. All scale bars represent 50 µm. Gratings dimensions (width x height x spacing) are 2 x 2 x 2 µm for 2uG, 5 x 5 x 5 µm for 5uG and 10 x 10 x 10 µm for 10uG. Blank refers to gels with no pattern. The glass coverslip was used as a control.

3.3.2. Attachment of mouse neural progenitor cells to PAA-ACA gels

First, direct cross-linking of whole laminin to PAA-ACA was tried. While imaging of fluorescent laminin indicates some laminin had been cross-linked to the surface of the gel, the mNPCs attached poorly to the gels after 24 hrs. The cells had round morphology, and there were many floating cells (Figure 3.4A). Next a cationic intermediary was tested. PLL and PLO were reacted at a concentration greater than that recommend by the supplier for coating as it was assumed the cross-linking reaction would not consume all PLL or PLO. Coating concentrations of 0.125 mg/cm^2 of PLL and 0.0175 mg/cm^2 PLO were used, versus the supplier's recommended density of 0.002 mg/cm^2.[190] Both PLO and PLL crosslinked to the gel followed by electrostatic binding of whole cell laminin improved cell adhesion, though the most notable effect was seen on the gel with PLL. (Figure 3.4B). On the platform with PLL and laminin, there was a high density of cells and almost all cells had a flat elongated morphology, typical of healthy mNPC. The PLO and laminin substrate had some cells with elongated morphology, but they were quite sparse, and most had a round morphology.

To see if adhesion could be further improved, heparin and laminin were combined in the second phase of electrostatic adsorption. However, heparin had a preventative effect on mNPC cell attachment in this system. On both the PLL and PLO conjugated samples, cells did not adhere after 24 hrs when a laminin-heparin solution was used as the ECM coating (Figure 3.4B).

Using the PLL scaffold with laminin, cells were differentiated on the scaffold for 14 days. Cells remained well attached after 14 days on the scaffold. Their expression of TUJ1 also indicated that they had successfully begun differentiating into neurons (Figure 3.4C). Additionally, it is important that once cells become neurons, they remain attached to the scaffold and continue to mature. After 14 days, cells expressed MAP2, a marker indicative of neuronal maturity, thus the neurons remained attached and were able to mature (Figure 3.4C).

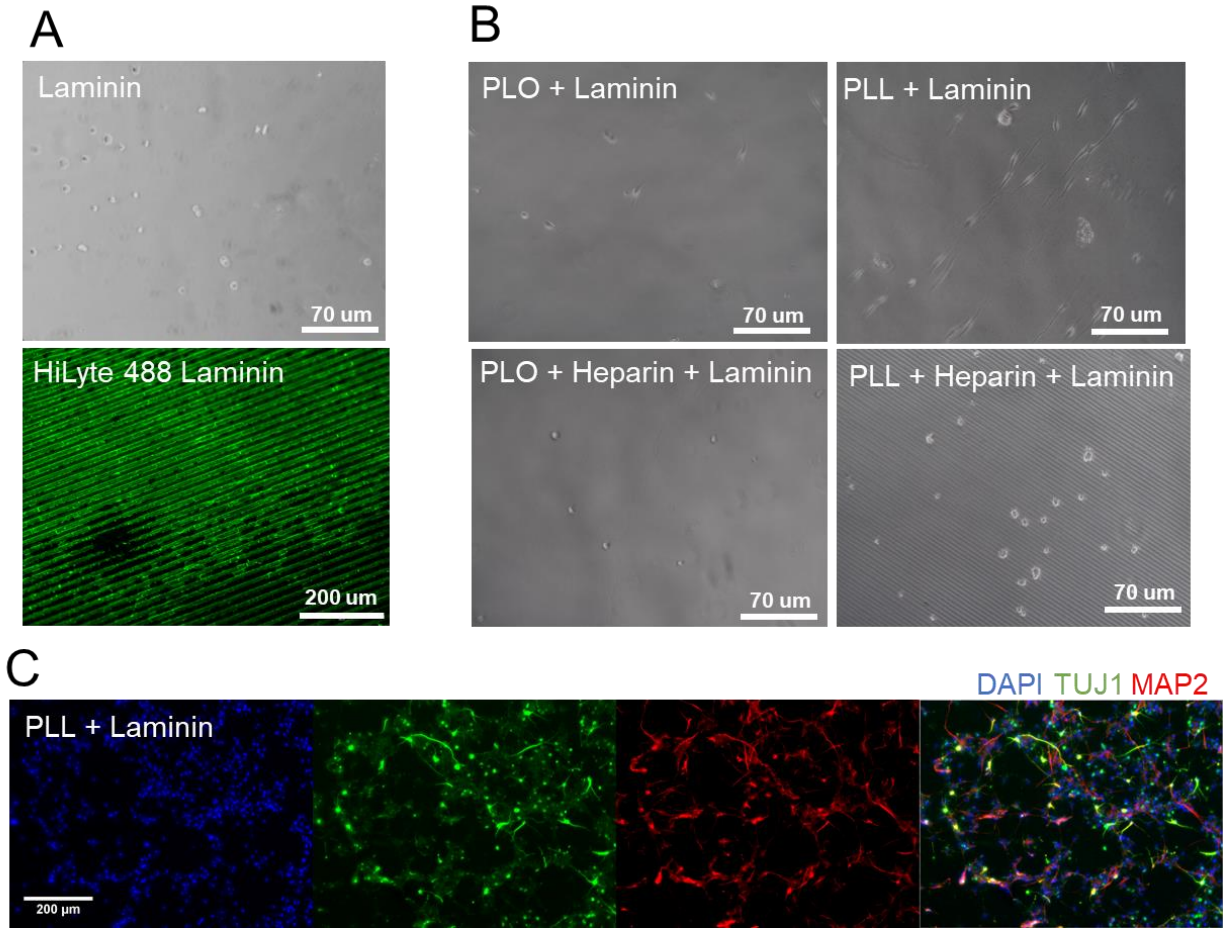

Figure 3.4 – Representative images of mNPC attachment on ECM-coated polyacrylamide- N-acryloyl-6-aminocaproic acid (PAA-ACA) hydrogels. (A) mNPC attachment on direct laminin-conjugated gel (top), and direct laminin conjugation visualized with HiLyte 488 Laminin (bottom). (B) mNPC attachment on PAA-ACA gels conjugated with polypeptide intermediates, electrostatic binding of laminin with and without heparin. (C) mNPCs and subsequently derived neurons attached to PAA-ACA conjugated with PLL and laminin coated after 14 days of differentiation on substrate. Stained with beta tubulin III (TUJ1) and microtubule associated protein 2 (MAP2) to show neuronal differentiation.

3.3.3. Adhesion of human neural progenitor cells to PAA-ACA gels

Direct cross-linking of laminin to PAA-ACA, and PLL cross-linking followed by electrostatic adsorption of laminin were the only two coating methods tested with hNPCs. On the substrate with direct laminin conjugation, hNPCs were only able to adhere if they were given a dose of 5 µm Y-26732 upon initial seeding. Without Y-26732 none of the cells adhered. On the substrate

with direct laminin conjugation and an initial dose of Y-26732, some cells adhered nicely with elongated morphology, but a large quantity did not adhere and floated in solution or adhered with round morphology and detached after two to three days (Figure 3.5A). Nonetheless, because cells were seeded at a fairly high density (20,000 cells/cm^2), a satisfactory number of cells remained well attached to the surface and the cells remained viable. On the substrate with PLL and laminin, cells were able to attach both with and without Y-26732. However, the cells attached much better with Y-26732. On the PLL and laminin substrate without Y-26732 a few cells showed flattened and somewhat elongated morphology; many were round and detached after two to three days (Figure 3.5A). Eventually even the weakly attached cells detached. On the PLL and laminin substrate with Y-26732, cells had an elongated morphology and most cells attached (Figure 3.5A). This caused the seeding density of 20,000 cells/cm^2 to be too high. A lower seeding density of 5,000 cell/cm^2 was determined to be more suitable for the PLL and laminin substrate with an initial dose of Y-26732.

To test extended attachment, hNPC were differentiated on the scaffold with direct laminin conjugation for 28 days. There were more cells on day 28 than on day 0, when they were seeded (Figure 3.5 A and B), implying a low initial seeding density may still result in a high number of cells for imaging. Cells remained well attached after 28 days on the scaffold. They also began expressing TUJ1 indicating they had successfully begun differentiating into neurons (Figure 3.5B). There were also some neurons expressing the mature neuronal marker MAP2, indicating that the derived neurons were capable of maturation on this substrate (Figure 3.5B).

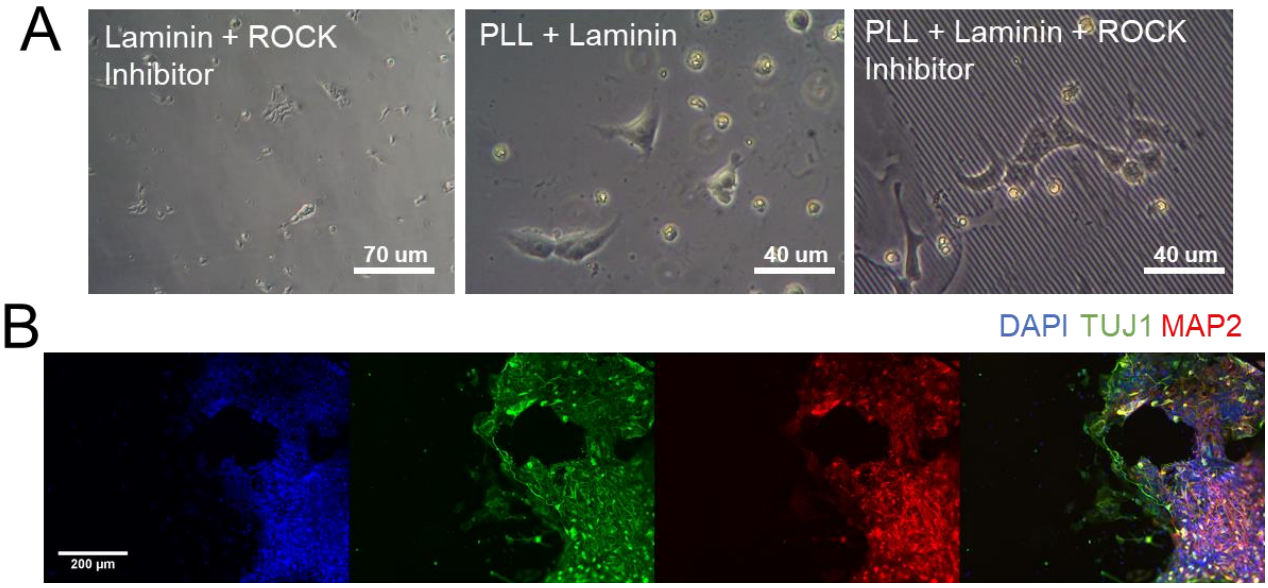

Figure 3.5 – Representative images of hNPC attachment on ECM-coated polyacrylamide- N-acryloyl-6-aminocaproic acid (PAA-ACA) hydrogels. (A) hNPC attachment on direct laminin-conjugated gel with ROCK inhibitor (left) and gels conjugated with PLL followed by laminin coating both with and without ROCK inhibitor (right). (B) hNPC and derived neurons attached to PAA-ACA conjugated directly with laminin with ROCK inhibitor after 28 days of differentiation on substrate. Stained with beta tubulin III (TUJ1) and microtubule associated protein 2 (MAP2) to show neuronal differentiation.

3.4. Discussion

Biophysical cues have been shown to be very powerful tissue engineering tools.[168, 169, 191] As investigations in the field progress and biophysical cues such as topography and stiffness are combined to optimize their potentially synergistic effects, it is important to develop platforms that can reliably vary these properties and allow for stable cell attachment. Presented here is a method to create a substrate with controllable stiffness, that can be patterned with micropatterns, to which ECM can be stably conjugated allowing for extended periods of cell attachment. Polyacrylamide is a commonly used platform for studying cell mechanics as it is simple to fabricate, has easily controllable stiffness, and is amenable to patterning with microtopography.[175-178, 180, 192, 193] However, cells will not adhere to poylacrylamide alone. Due to the setbacks of sulfo-SANPAH

and more tedious methods such as PEGylation of ECM, for this study we opted to use the copolymer developed by Yip *et al*., PAA-ACA.[180] Using this platform, we were able to create a gel platform with controllable stiffness, that can be patterned with micropatterns, to which ECM can be easily conjugated allowing for stable long-term cell attachment.

The gels were simple and quick to make. They could be made and used within the same day or made ahead of time and stored for up to one week. They were easy to handle due to their attachment to a glass coverslip. This also prevented them from floating in media, a tedious yet common problem with hydrogels. The gels were completely transparent and did not have autofluorescence, making them ideal for immunofluorescent imaging. Using the sandwiching method, the gels could be cast in a thin layer, further contributing to their excellent optical properties. The height of the gels on average was 196.20 μm ± 13.86 μm. It has been shown that cells including, mesenchymal stem cells, stem-cell derived neurons, myoblasts and osteoblasts, can sense underlying surface stiffness on gels thinner than 20 μm.[194, 195] Therefor, the gel was thick enough to ensure the stiffness of the underlying glass coverslip did not influence the stiffness the cells feel.

The PAA-ACA gels also had consistent and repeatable stiffness for each ratio of acrylamide and bisacrylamide used. The measure stiffnesses were also significantly distinct from one another. Compared to the moduli recorded for PAA-ACA gels using atomic force microscopy (AFM) spherical indentation and a Hertz model for fitting done by Yip *et al*., the results of mechanical testing with the Microtester were very comparable (Figure 3.2C).[180] The PAA-ACA gels also retained the purely elastic nature of polyacrylamide gels, which is one of they key advantages of polyacrylamide gels as this helps to prevent the confounding effect of viscoelasticity. We were also able to pattern the gels with consistency. The average height, width and spacing of 2uG, 5uG and 10uG samples was consistent among replicas. Due to the difficulty of performing AFM on fully hydrated hydrogel samples at 37 ^{o}C, we assumed the bulk elastic modulus measure with the Microtester, would be comparable to the effective modulus sensed by

the cells with or without patterns, seeing as samples were sufficiently thick (> 20 μm). However, it should be noted that patterns can modify the effective stiffness though if they are deformable. In another study by Yip *et al*., using a PAA-ACA gel with micrometer gratings topography, they found that AFM analysis, using a probe with 4.5 um-diameter sphere attached to the cantilevers, resulted in a Young's modulus that was very similar to the findings of their previous AFM analysis using a blank PAA-ACA gel with the same acrylamide to bisacrylamide ratio (16.9 kPa vs. 16.6 kPa). [65, 196]

The same concentration of ACA was used in each copolymer to ensure even distribution of conjugated cell attachment factors. As the carboxyl on the ACA group is the only group available for carbodiimide crosslinking with a primary amine, the amount of conjugated material should be proportional to the concentration of ACA. We first attempted to conjugate whole laminin using carbodiimide crosslinking chemistry. Whole laminin is much cheaper than recombinant laminin. Recombinant laminin has also been shown to influence stem cell self-renewal and differentiation via mechanotransduction pathways.[197-200] However, we found that direct carbodiimide conjugation of whole laminin was not sufficient for attachment of mNPC. To see if steric hinderance due to the large size of laminin (400 – 900 kDa) was impeding crosslinking, fluorescently tagged laminin was used to verify immobilization. Doing this we were able to verify that the laminin had been conjugated to the surface. Laminin is a heterotrimeric protein comprised of three subunits, which have a wide variety of binding domains. Cells needs to be able to access these subunits and binding domains for laminin to work as a cell attachment factor. Many of these cell binding sites contain amino acids with free amines meaning they could be obscured from cells due to crosslinking. [201] Further it is impossible to control which of these amines will react in carbodiimide crosslinking, meaning how immobilized laminin will be oriented relative to the substrate and the cell cannot be controlled either. Because laminin immobilization was confirmed but cells still did not attach, it was assumed the immobilized laminin orientation, conformation, or potential change in quaternary structure could be the cause of low cell adhesion.

A common practice in standard cell culture protocols is the use of an intermediate cationic polypeptide to enhance laminin adsorption through electrostatic interactions. Two such polypeptides are PLL and PLO. The cruciform shaped laminin has cell-surface receptor binding domains at the top and bottom of the cross. Towards the bottom of the molecule near the lower binding domain, are carboxyl groups which interact with the positively charged PLL or PLO layer. Thus, the laminin binds in an upright position, like a grave stone, allowing cells access to the upper cell-surface receptor binding domain and adhere to the surface (Figure 3.1B).[202] Furthermore, both PLL and PLO, have free amine residues, making them suitable for carbodiimide crosslinking to PAA-ACA. Interestingly, despite their structural similarity and common method of action, only PLL enhanced cell attachment. Both polypeptides were added a density greater than that recommended by the supplier. Both polypeptides also had the same range of molecular weight. It is likely that limiting reagent in this reaction was the carboxyl groups on the surface of the thin gel rather than the polypeptides in solution as both the PLL and PLO were added in excess. PLO and PLL have the same backbone but vary in their pendant groups. PLO has a propylamine pendant group and PLL has a butylamine pendant group. The second phase of EDC/NHS chemistry involves nucleophilic attack of the NHS ester, such as a primary amine. While the primary amines of PLL and PLO have similar pKa values (pKa 10.5 – 10.7), the two molecules do have conformational differences.[203, 204] Therefor it is suspected the difference in performance between PLL and PLO is a result of differing cross-linking efficiencies due to steric hinderance and access to primary amine groups.

After the improvement seen with PLL, we next tried incorporating heparin to see if it could further improve mNPC attachment. Heparin is known to interact with almost all ECM components *in vivo*, playing a role in the mediation of adhesion of cells by acting as co-receptors that integrate cell signals.[205, 206] A variety of platforms have even used grafted heparin to improve neuronal cell attachment.[207-210] Despite this, using PLL, and laminin with heparin, resulted in a notable reduction of cell attachment to the substrate. Laminin has a heparin binding site in its long-arm G domain,

to which heparin has a high binding affinity.[206, 211, 212] The heparin and laminin solution used in this step was reacted prior to use with the substrate to ensure heparin binding to laminin. However, because of the strong negative charge of heparin and its affinity to bind to laminin, there is a chance that the bound heparin changed the charge distribution of laminin. Thus, the orientation of laminin during electrostatic binding to PLL could have been affected such that it no longer supported cell adhesion. Perhaps it would be more advantageous to bind heparin and laminin to the surface separately to ensure they do not intervene in each other's electrostatic binding. It is also interesting to note, that despite PLL often being used to improve cell attachment to surface, without biologically active laminin (such as the case with the combine heparin and laminin), cells would not adhere to the PLL-crosslinked substrate. This implies that the cells are still adhering predominantly to laminin, and the orientation of this laminin must be different than that of the directly crosslinked laminin.

On the PLL-laminin samples, mNPC were able to adhere for 14 days. This is important because it can take up to 14 days of differentiation for mNPC to express TUJ1, a marker that indicates commitment to the neuronal lineage. At the 14-day mark cells were well adhered and expressed TUJ1. By this point their expression of the mature neuronal marker, MAP2, indicated they had begun maturation and the differentiated mouse neurons were also compatible with the substrate. Using hNPC the PAA-ACA gel with directly cross-linked laminin was sufficient for cell adhesion. The hNPC were able to adhere for 28 days, which is how long it takes differentiating hNPC to begin to express TUJ1. At the 28 day mark they were well adhered and expressed TUJ1 and MAP2, indicating the hNPC could survive and undergo the ordeal of differentiation on the platform and the differentiated human neurons were compatible with the substrate. Both the 14-day long attachment of mNPC and the 28-day long attachment of hNPC on the PAA-ACA gel is longer than (to the best of that author's knowledge) any other study seeding either type of neuronal progenitor cell on a polyacrylamide or polyacrylamide co-polymer.

It should be noted though, that the human NPC were only able to adhere to the laminin substrate with an initial dose of Y-26732. A 10 μM dose of Y-26732 is commonly used in standard protocols for iPSC culture and iPSC-derived hNPC culture to reduce dissociation-induced apoptosis and encourage cell attachment.[213-215] Cells are dissociated prior to seeding on the PAA-ACA substrates thus a dose of Y-26732 (5 μM) was used during seeding. Y-26732 acts by affecting mechanotransduction pathways, which could be of concern for mechanobiology studies. However, it becomes inactivated over time in media with cultured cells. The effects of Y-26732 on cells also wears off if additional doses of Y-26732 are not added to cells. Ishizaki *et al*. showed that a 10 μm dose of Y-26732 delivered to Swiss 3T3 cells abolished actin bundles, however 24 hrs after the dose was delivered the actin bundles returned. [216]

The required hNPC seeding densities also differed between the laminin gel and the PLL-laminin gel, with the use of an initial dose of Y-26732. On the laminin gel, cells eventually had stable, long-lasting adhesion, but initially few adhered, so a high density of 20,000 cells/cm^2 had to be used. In comparison, on the PLL-laminin gel, seeding the cells at 20,000 cells/cm^2 resulted in over confluence after three days. A lower density of 5,000 cells/cm^2 was determined to be more suitable for the PLL-laminin gel as more cells adhered to it initially. For the PLL-laminin gel seeded without Y-26732, at 20,000 cells/cm^2 very few cells adhered, and those that did adhere detached after two or three days, likely due to the sparse density. It is worthwhile investigating if a higher density could be used such that the PLL-laminin gel could be seeded without the addition of Y-26732.

3.5. Conclusions

In conclusion, using a polypeptide intermediate, whole laminin can be conjugated to the surface of PAA-ACA gels such that it is bioavailable and allows for stable attachment of cells.

PAA-CA can be fabricated to have reliable and repeatable stiffness in the scale of kilopascals and topography with consistent dimensions in the microscale. Further this copolymer is purely elastic preventing the confounding effects of viscoelasticity. With carbodiimide crosslinking, extracellular matrix required for cell adhesion can also be stably added to the gel to allow for extended adhesion of both human and mouse neural progenitor cells and subsequently derived neural cells. Mouse NPC tended to be more sensitive to laminin activity, as they could not adhere to substrates with directly bound laminin but could adhere to substrates with electrostatically adsorbed laminin. Additionally, heparin interactions with laminin prevent mNPC attachment. Human NPC are less sensitive to laminin activity if ROCK inhibitor is added upon seeding. The conjugation of a polypeptide intermediate followed by electrostatic binding of laminin improved initial hNPC cell attachment as more cells attached, but none the less ROCK inhibitor was still required for attachment. Future studies should aim to optimize hNPC seeding density to determine if a density exists such that a suitable number of hNPC may be able to adhere to the PLL and laminin substrate without the addition of ROCK inhibitor.

CHAPTER

4

Combined effect of stiffness and topography on neuronal differentiation

4.1. Introduction

Topography and stiffness have independently been shown to have a powerful effect on neuronal differentiation. They can enhance neuronal differentiation rate, neuronal lineage commitment and morphology of resulting neurons. [59, 61-63, 66, 68, 75, 79, 91, 92, 101, 108, 117, 119, 121, 122, 134, 149, 150, 217-224] Further they are inexpensive tools that can and have been implemented into a variety of biomaterials for both *in vitro* and *in vivo* applications such as drug screening platforms, neurological disease models, peripheral nerve grafts, and scaffolds for central nervous system repair. [9, 95, 225-229]

However, there are few studies that have investigated their combined effects. An understanding of their interaction could offer insight into *in vivo* cellular response to these cues, optimization of these cues for biomaterials and a better understanding of how they affect mechanotransduction pathways. *In vivo* cells are simultaneously exposed to both stiffness and topography. Thus, when we try to determine how cells are affected by topography, and use the *in vivo* microenvironment to guide our investigations, it makes sense to study topography in the context of stiffness. In terms of biomaterial optimization, an understanding of potential interactions is important because it is impossible to impart only the cue of topography. Topography can only be applied on substrate which will have some characteristic stiffness. Thus, when designing biomaterials with topography, it is important to take into account how the effect of topography may differ with substrate stiffness. Additionally, it could allow for the opportunity to potentially design substrates that are even better tailored to promoting neuronal differentiation because multiple cues could be optimized. Lastly, the effects of topography and stiffness on neuronal differentiation have been implicated to be cause by the same mechanotransduction pathways. [1, 101, 119, 120, 149, 230]

In this chapter we investigated how combined topography and stiffness cues affect neuronal differentiation. We hypothesized that stiffness and topography would have a notable interaction effect on neuronal differentiation. To do this we differentiated mNPC on PAA-ACA gels with four different stiffnesses, and four different topographies. Samples were then immunofluorescence stained for TUJ1, GFAP, and MAP2 to gauge neuronal lineage commitment based on marker expression, and neuronal maturation based on marker expression and morphology.

4.2. Methods and Materials

4.2.1. Maintenance culture of primary mouse neural progenitor cells

Primary mouse neural progenitor cells were expanded in maintenance media containing a basal media comprised of 1:1 Dulbecco's modified eagle medium and Ham's F12 medium with added L-glutamine and HEPES buffer without sodium bicarbonate (DMEM/F12) (11330032, Gibco), penicillin-streptomycin (LS15070063, Gibco), and N2 supplement (17502048, Gibco). A supplement of recombinant human fibroblastic growth factor (bFGF) (Gibco PHG0021) and recombinant human epidermal growth factor (EGF) (Gibco PHG0311) was added daily. Concentrations of maintenance media components can be found in Table 3.2. Cells were seeded in 6-well plates coated with 25 mg/ml Matrigel (356234 Corning). Cells were passaged once they reached 95% confluence and were seeded using a split ratio of either 1:2 or 1:3, such that their seeding density was between 30,000 – 60,000 cells/cm^2. Media was changed 50% every other day. Cells were grown in an incubator at 37 ^{o}C, 5% CO_2 and 99% humidity.

4.2.2. Differentiation of primary mouse neural progenitor cells

After thawing, mNPC were passaged at least four times prior to use in experiments. Cells were used between passages 15 – 19 for all experiments. Cells were seeded on PAA-ACA and

glass coverslips substrates at a density of 20,000 cells/cm^2, in maintenance media (Table 3.2). Cells were allowed to attach overnight in an incubator at 37 ^oC, 5% CO_2 and 99% humidity. The next day the maintenance media was replaced with induction media to remove unattached cells and begin differentiation. Induction media was comprised of a basal media of DMEM/F12 (11330032, Gibco), penicillin-streptomycin (LS15070063, Gibco), N2 supplement (17502048, Gibco), Glutamax (35050061 Gibco), and B27 supplement (17504044 Gibco). A supplement of recombinant human fibroblastic growth factor (bFGF) was added daily. Concentration of induction media components can be found in Table 3.2. Media was changed 50% every other day. Cells were kept in induction media for seven days. On day seven, media was completely changed to maturation media. Maturation media was comprised of a basal media of comprised of equal amounts DMEM/F12 (11330032, Gibco) with Neurobasal media (21103049 Gibco), penicillin-streptomycin (LS15070063, Gibco), N2 supplement (17502048, Gibco), Glutamax (35050061 Gibco), and B27 supplement (17504044 Gibco). Concentration of maturation media components can be found in Table 3.2. For the entirety of the differentiation period, cells were kept in an incubator at 37 ^oC, 5% CO_2 and 99% humidity. Maturation media was changed 50% every other day. Cells were kept in maturation media for seven days. On day 14, cells were fixed for staining. This differentiation timeline can be seen in Figure 4.1A.

4.2.3. Preparation of PAA-ACA hydrogel substrates and coverslip control

PAA-ACA gels were fabricated as described in sections 3.2.1. – 3.2.4. Briefly, glass coverslips were treated with ATPES and glutaraldehyde. A pre-polymer solution of acrylamide, bisacrylamide, ACA and water was deposited on the treated coverslips and topped with a micropatterned PET mold. The polymer was crosslinked using TEMED and APS and the reaction was carried out for 10 min in an incubator at 37 ^oC, 5% CO_2 and 99% humidity. Once crosslinked, samples were quenched in MES buffer. The PET molds were removed and samples were washed

thrice with MES buffer. Samples were UV sterilized, then EDC and NHS were used to activate the surface of the gels. Once activated, the samples were reacted with PLL to conjugate it to the surface of the samples. Samples were washed and then laminin was then allowed to electrostatically bind to the PLL-coated surface. Before use, samples were washed once with 1X PBS, and allowed to soak in DMEM/F12 media for 30 min in the incubator. Analysis of sample stiffness and topography dimensions can be found in section 3.3.1. The stiffness and topographies used in this study can be found in Figure 4.1B.

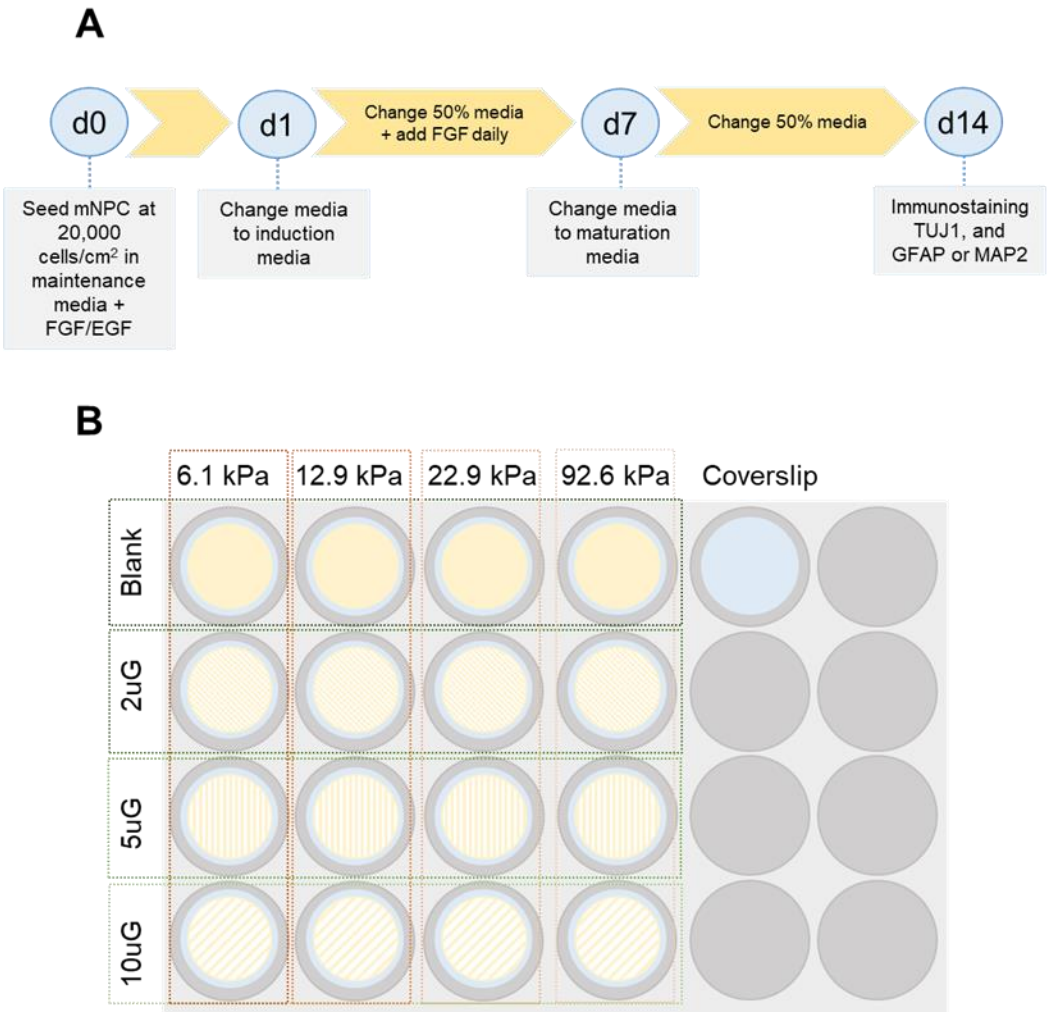

Figure 4.1 – Parameters used to investigate the combined effect of stiffness and topography on neuronal differentiation of mNPC. (A) Differentiation timeline. (B) Overview of the polyacrylamide-N-acryloyl-6-aminocaproic acid copolymer (PAA-ACA) gels topography and stiffness combinations used in this study. The glass coverslip acted as a control.

4.2.4. Immunofluorescence staining

After 14 days of differentiation, cells were fixed with 4% paraformaldehyde, permeabilized with 0.25% Triton X-100 and blocked with 1% (w/v) bovine serum albumin and 10% (v/v) goat serum in 1X tris-buffered saline (TBS) overnight at 4 ^{o}C. Cells were immunostained with β-tubulin III (TUJ1) (rabbit anti-TUJ1 at 1:600, polyclonal, Sigma Aldrich), and microtubule associated protein (MAP2) (mouse anti-microtubule associated protein at 1:600, polyclonal, Abcam) or glial fibrillary acidic protein (GFAP) (mouse anti-GFAP at 1:600, polyclonal, Sigma Aldrich) overnight at 4 ^{o}C. Samples were then washed with washing buffer composed of 0.05% triton X-100 and 1% goat serum in 1X TBS. Secondary staining was done with Alexa Fluor 488 goat anti-rabbit IgG at 1:1000 (Invitrogen) for TUJ1 and Alexa Fluor 546 goat anti-mouse IgG at 1:1000 (Invitrogen) for MAP2 or GFAP, overnight at 4 ^{o}C. Samples were counterstained with DAPI at 1:2200 for one hour at room temperature. Imaging was done using a fluorescence microscope (Axio Observer Z1, Zeiss GmBH) and analyzed using the software ImageJ and CellProfiler.

ImageJ was used to convert the image stacks to individual greyscale images. A pipeline in Cell Profiler to determine the percentage of cells positive for a given marker including TUJ1, GFAP or MAP2 was constructed as follows. First an image illumination correction function for the DAPI channel was calculated for each image based on background illumination. This function was then applied to remove shadows. Next DAPI objects were enhanced using the speckles feature type with a feature size of 40 pixels. Next background was suppressed using a feature size of 15 pixels. Identify primary objects was used to identify DAPI. An object diameter of 20 to 80 pixels was required and a global thresholding strategy with the Robust Background method was used. Next the neuronal or glial marker channel was enhanced using the neurites feature type, enhancing based on tubeness smoothing with a smoothing scale of three. Next marker positive cells were identified as secondary objects with DAPI objects used as input objects. A watershed was used at the identification method, and a global thresholding strategy with the

robust background method was applied. Last, the identified secondary objects were filtered by form factor (<0.25) and compactness (>5) to ensure they were not debris that may have been near a nuclei.

Neurite length and branching was also measured using a Cell Profiler pipeline. MAP2 positive cells were identified as described above. The objects were then skeletonized and each neurite was reduced to a line. Length and branching was then measured.

4.2.5. Statistics

Two-way analysis of variance (ANOVA) and Tukey's post-hoc test with an alpha of 0.05 were used to determine statistical significance. Cells differentiated on the glass coverslip were used as the control. The control was used as a reference value and indicator of cell health and neuronal differentiation capability between biological replica. It was not included in the ANOVA or pairwise analysis. All values are reported as mean with a 95% confidence interval. The symbols *, **, ***, **** represent $p<0.05$, $p<0.01$, $p<0.001$, and $p<0.0001$, respectively. Spearman's coefficient, r, was used an indicator of relationship direction and strength between factors. A correlation coefficient between 0.1 – 0.29 was considered to be low, a value between 0.3 – 0.49 was considered to be moderate, and a value >0.5 was considered high. For correlation analysis, topography was treated as a continuous variable with average feature dimension size used to quantify each topography. To code the 2uG, 5uG and 10uG patterns, two, five and ten were used, respectively. A value of zero was used for the blank. Average values of percent positive or morphology measurements per substrate type were used for response variables.

All TUJ1 data was collected from N=5 biological replica, with n = 2 or 3 technical replica and a total of 2,000 to 7,000 cells being analyzed for each stiffness and pattern combination. All MAP2 data was collected from N=3 biological replica, with n = 3 technical replica and a total of 2,000 to 6,000 cells being analyzed for each stiffness and pattern combination. All GFAP data

was collected from N=2 biological replica, with n=2 technical replica and a total of 110 to 1,000 cells being analyzed for each stiffness and pattern combination. For neurite length and branching, approximately 50 to 200 cells were analyzed for each stiffness and pattern combination.

4.3. Results

4.3.1. Effect of stiffness and topography on neuronal lineage commitment

TUJ1 and GFAP were used as indicators of neuronal or astrocyte lineage commitment, respectively. Both TUJ1 and GFAP were present on the coverslip control indicating cells were healthy and capable of differentiation. In general, all gels regardless of topography or stiffness had a higher percentage of TUJ1+ cells compared to the coverslip control. Gels with patterns tended to have lower percentages of GFAP+ cells compared to the control. Representative images of TUJ1 and GFAP expression on each stiffness and pattern combination can be seen in Figure 4.2. Pairwise comparisons and interaction plots between factors and the percent TUJ1+ or GFAP+ can be found in Figure 4.3 and Figure 4.4, respectively. The average percentage of cells expressing TUJ1 or GFAP each stiffness and pattern combination can be found in Table 4.1. Spearman correlation coefficients calculated between parameters and the percentage of cells expressing TUJ1 or GFAP can be found in Figure 4.5.

ANOVA analysis indicated that stiffness, topography and their combined interaction all had a significant effect on the percentage of TUJ1+ cells ($p<0.0001$ for each) indicating that they all significantly affected neuronal lineage commitment. ANOVA analysis indicated that topography had a significant effect on percent GFAP+ ($p = 0.02$) but stiffness and topography did not have a significant effect. Overall, the highest percentage of TUJ1+ cells was seen on the 6.1 kPa gel with 5uG pattern (37% positive) and the lowest was seen on the 92.6 kPa gel with no pattern (13.8% positive). The highest percentage of GFAP+ cells was seen on the 92.6 kPa gel

with no pattern (25% positive) and the lowest was seen on the 22.9 kPa gel with the 2uG pattern (9.4% positive).

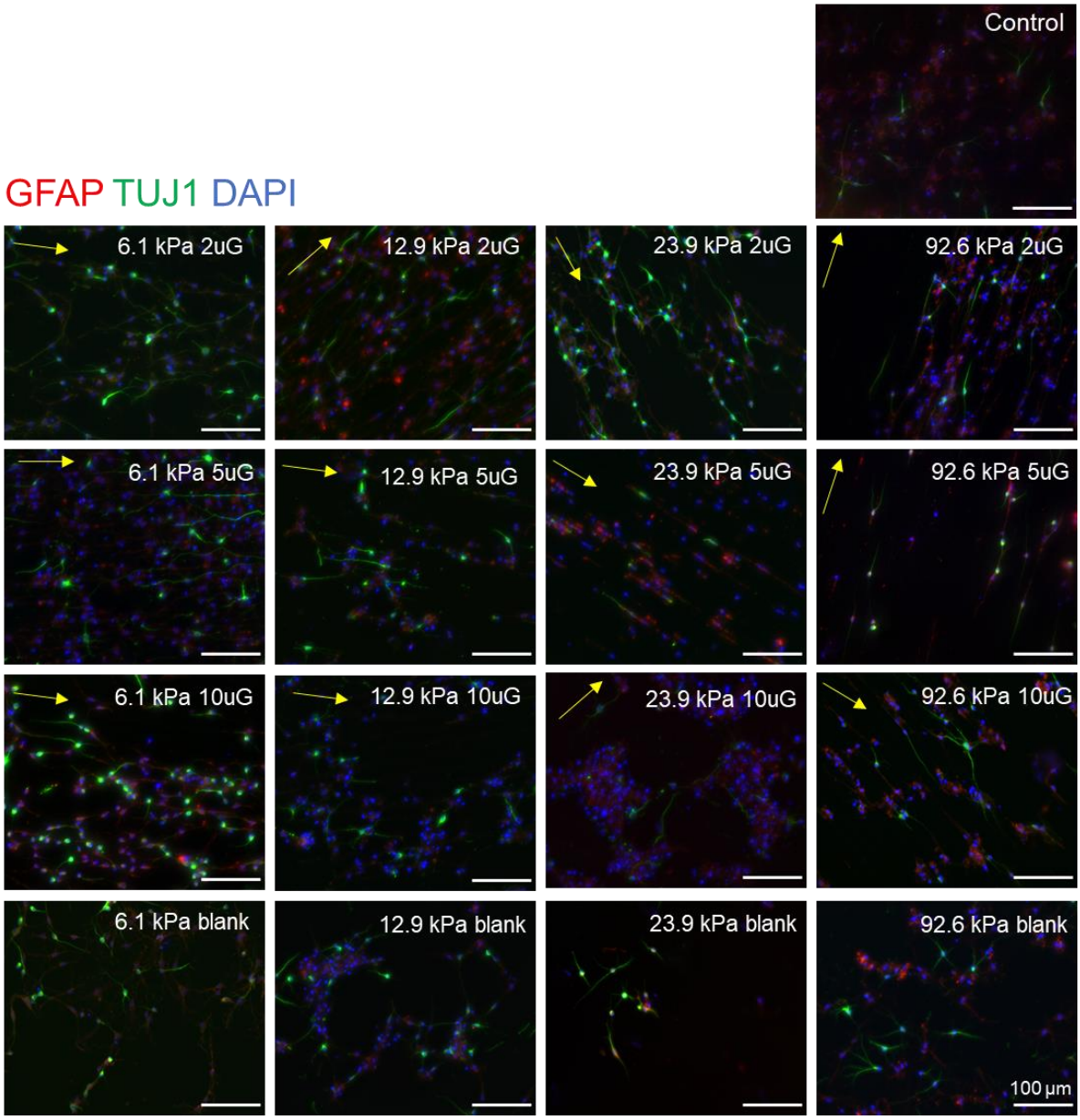

Figure 4.2 – Representative images of beta tubulin III (TUJ1) and glial fibrillary acidic protein (GFAP) expression on gels of varying stiffness and topography. Young's modulus and topography are labelled in the top right corner for each image. Yellow arrows in the top left corner indicate the gratings direction. All scale bars represent 100 µm. Gratings dimensions (width x height x spacing) are 2 x 2 x 2 µm for 2uG, 5 x 5 x 5 µm for 5uG and 10 x 10 x 10 µm for 10uG. Blank refers to gels with no pattern. The control is a glass coverslip.

Table 4.1 – Percentage of TUJ1+ cells, GFAP+ cells and MAP2+ cells on the different stiffnesses and patterns.

Stiffness	Topography	TUJ1 Positive	GFAP Positive	MAP2 Positive
Glass coverslip control		8.4%	25.6%	6.9%
6.1 kPa	2uG	26.1%	15.2%	16.9%
	5uG	36.6%	11.5%	22.9%
	10uG	27.7%	19.1%	14.5%
	Blank	19.6%	17.0%	7.4%
12.9 kPa	2uG	35.6%	17.1%	21.1%
	5uG	27.6%	13.0%	18.3%
	10uG	22.2%	24.1%	17.6%
	Blank	16.4%	21.0%	11.8%
22.9 kPa	2uG	29.1%	9.4%	11.8%
	5uG	21.5%	11.7%	13.2%
	10uG	17.3%	27.3%	9.13%
	Blank	13.9%	15.2%	11.0%
92.6 kPa	2uG	24.9%	10.0%	11.6%
	5uG	22.7%	14.1%	11.9%
	10uG	16.0%	17.6%	12.8%
	Blank	13.8%	25.1%	9.0%

Topography dimensions had a low degree of positive correlation with percent TUJ1+ as measured by the Spearman correlation coefficient ($r = 0.25$). Within each stiffness group, trends of patterns having a higher percentage of TUJ1+ cells than their respective blanks were observed. A positive curvilinear relationship between percent TUJ1+ and topography dimensions was observed for the 6.1 kPa gels (Figure 4.4B). The stiffer gels had more linear relations. Within the 12.9 kPa, 22.9 kPa and 92.6 kPa stiffness groups, the 2uG samples had the highest percentage of TUJ1+ cells but in the 6.1 kPa group, the maxima occurred at the 5uG pattern.

In the 12.9 kPa and 22.9 kPa groups, the 2uG pattern had a significantly higher percentage of TUJ1+ cells, compared to the 5uG, 10uG ($p<0.0001$) and blank samples ($p < 0.02$). In the 92.6 kPa groups, the 2uG samples had a higher percentage of TUJ1+ cells compared to the 5uG pattern but was only significantly greater than the 10uG and blank ($p < 0.003$) (Figure 4.3A). Interestingly, on the 6.1 kPa sample, the 2uG pattern had a significantly higher percentage of TUJ1+ cells compared to the blank ($p = 0.05$) but was lower than the other two patterns. It had significantly less TUJ1+ cells than the 5uG sample ($p=0.0004$) and, while not statistically significant, it had less TUJ1+ cells than the 10uG sample. In all stiffness groups, the 5uG pattern had a significantly higher percentage of TUJ1+ cells compared to their respective blanks ($p < 0.01$) (Figure 4.3A). The 5uG samples also had a significantly higher percentage of TUJ1+ cells than the 10uG samples, in the 6.1 kPa and 92.6 kPa stiffness groups ($p < 0.03$). In only the 6.1 kPa group did the 10uG pattern have significantly more TUJ1+ cells compared to the blank ($p = 0.01$). In the other stiffness groups, the 10uG pattern had a higher percentage of TUJ1+ cells than the respective blank, but it was not statistically significant.

Stiffness had a moderate negative linear correlation with percent TUJ1+ ($r = -0.49$). In general, the curves representing percent TUJ1+ vs topography for each stiffness group, tended to shift downward as stiffness increased. For all patterns and the blank a trend of percent TUJ1+ decreasing with increasing stiffness was observed, the exception being the 6.1 kPa with 2uG pattern (Figure 4.3B). The 2uG pattern produced the most TUJ1+ cells on the 12.9 kPa gel and the percentage of TUJ1+ cells on this pattern significantly decreased as stiffness changed in either direction ($p<0.04$). Interestingly, with the 2uG pattern, the 22.9 kPa gel also had a higher percentage of TUJ1+ cells compared to the 6.1 kPa gel, however this difference was not statistically significant ($p = 0.63$). The 2uG pattern on the 6.1 kPa gel did have a higher percentage of TUJ1+ cells than on the 92.6 kPa gel though ($p = 0.96$). The highest percentage of TUJ1+ cells on the 5uG pattern was seen on the 6.1 kPa gel and the percentage of TUJ1+ cells significantly

decreased as stiffness increased ($p < 0.003$), compared to the 6.1 kPa gel. Additionally, on this pattern, the 12.9 kPa gel had more TUJ1+ cells than the 22.9 kPa substrate and the 92.6 kPa which were very close to one another ($p > 0.07$). The 10uG pattern and the blank showed a direct relationship with stiffness and percent TUJ1+ cells, with the percentage decreasing as stiffness increased, in a direct manner. However, these differences were not statistically significant.

The interaction of topography and stiffness (T*S) had a strong negative correlation with percent TUJ1+ ($r = -0.86$), indicating as T*S increases percent TUJ1+ decreases. Additionally, this implies that the percent TUJ1+ on small patterns increases with increasing stiffness, and the percent TUJ1+ on larger patterns increases with decreasing stiffness. For example, the 5uG pattern on the 6.1 kPa gel results in nearly the same amount of TUJ1+ cells as the 2uG pattern on the 13.2 kPa gel ($p > 0.999$). The percentage of TUJ1+ positive cells on the 10uG pattern on the 6.1 kPa gel is similar to that of the 5uG pattern on the 13.2 kPa gel ($p > 0.999$). The percentage of TUJ1+ positive cells on the 5uG pattern on the 12.9 kPa gel is similar to that of the 2uG pattern on the 22.9 kPa gel ($p > 0.999$). The percentage of TUJ1+ positive cells on the 10uG pattern on the 12.9 kPa gel is similar to that of the 5uG pattern on the 22.9 kPa gel ($p > 0.999$). This interaction trend fades between the 22.9 kPa and 92.6 kPa gels, where patterns begin to result in similar amounts of TUJ1+ cells on the two stiffnesses.

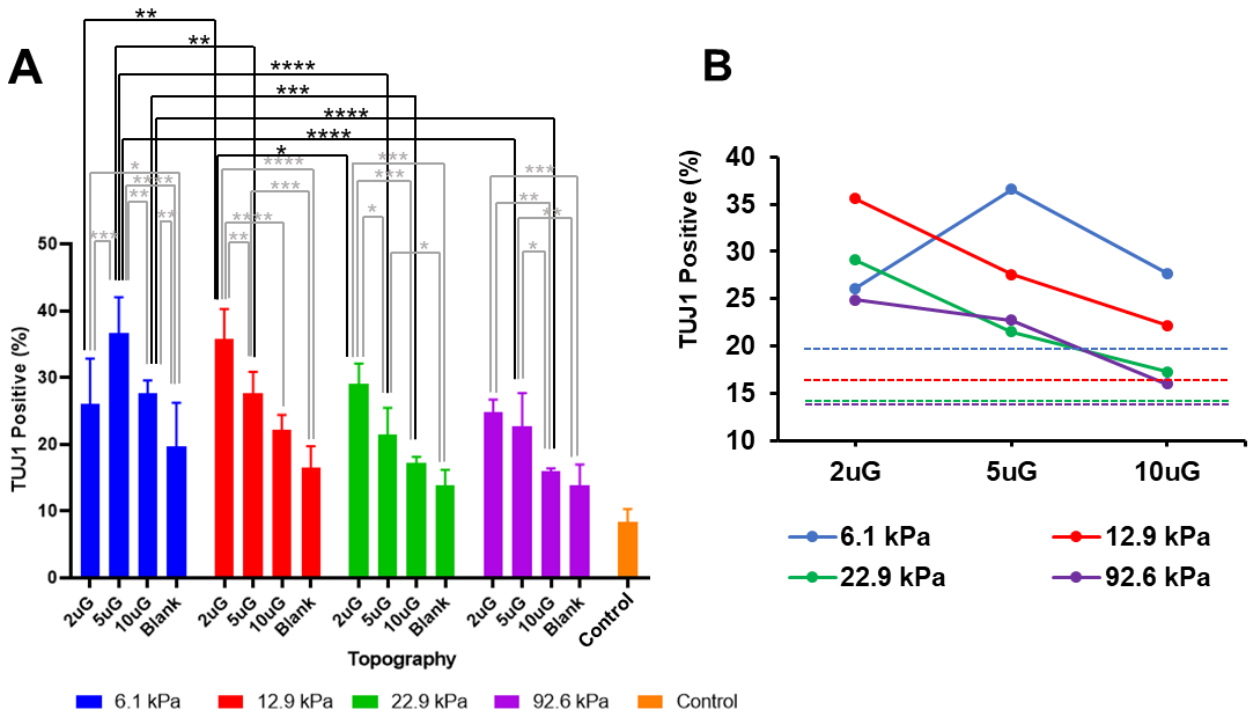

Figure 4.3 – Neuronal lineage commitment gauged by the percentage of beta tubulin III (TUJ1) positive cells on substrates with various stiffnesses and gratings of various dimensions. (A) Between and within stiffness and topography group pairwise comparisons of percent TUJ1+ cells. Data is shown as the average of N=5 biological replica with SD. The symbols *, **, ***, **** represent p<0.05, p<0.01, p<0.001, and p<0.0001, respectively. (B) Interaction plot of percent TUJ1+, topography and stiffness with dashed lines indicating the blank for each stiffness. Data is shown as the average of N=5 biological replica. Gratings dimensions (width x height x spacing) are 2 x 2 x 2 µm for 2uG, 5 x 5 x 5 µm for 5uG and 10 x 10 x 10 µm for 10uG. Blue = 6.1 kPa, red = 12.9 kPa, green = 22.9 kPa, purple = 92.6 kPa and orange = control.

In general, the trends seen with GFAP expression were opposite to those seen with TUJ1 expression, though only topography had a statistically significant effect. Topography had a low degree of positive correlation with percent GFAP+ (r = +0.15). Though, similar to TUJ1, the relation between topography and percent GFAP+ was shown to be curvilinear. Opposite to TUJ1, a negative curvilinear relationship was seen between percent GFAP+ and topography for all stiffnesses (Figure 4.4B). The minima of these curves depended on stiffness.

Within stiffness groups, the 2uG and 5uG patterns had lower percentages of GFAP+ cells compared to the 10uG pattern and blank (Table 4.1, Figure 4.4A). However, no statistically

significant pair wise comparisons could be made. Interestingly, on the stiffest two gels the 2uG pattern had less GFAP+ cells than the 5uG pattern, but on the softest two gels the opposite was observed. For all stiffness groups, except the 92.6 kPa stiffness group, the 10uG pattern increased the percentage of GFAP+ cells relative to the respective blank.

Stiffness did not correlate with percent GFAP+ (r = -0.05). The amount of GFAP+ cells at each respective curve's minima in Figure 4.4B, were similar between each curve, as increasing stiffness did not noticeably shift the curves up or down. For the blank samples, the percentage of GFAP+ did not seem to change with stiffness. For the 10uG samples, the percentage of GFAP+ cells was highest on the 22.9 kPa gel and decreased incrementally as the stiffness decreased. Interestingly, for the 5uG samples, all stiffnesses had a very similar amount of GFAP+ cells. For the 2uG samples, the percentage of GFAP+ cells was somewhat higher on softer substrates compared to stiffer substrates. Between the softest two substrates and between the stiffest two substrates, the percentage of GFAP+ cells on the 2uG pattern were very similar.

While no strong correlations between percent GFAP+ and the factors of topography and stiffness alone could be drawn, the interaction T*S, had a strong positive correlation with percent GFAP+ (r = +0.57). Smaller features reduce the percent GFAP+ cells better on stiff gels, and larger features reduce percent GFAP+ better on soft gels. This can be seen in Figure 4.4B, where in the local minima changes from 5uG to 2uG as stiffness increases.

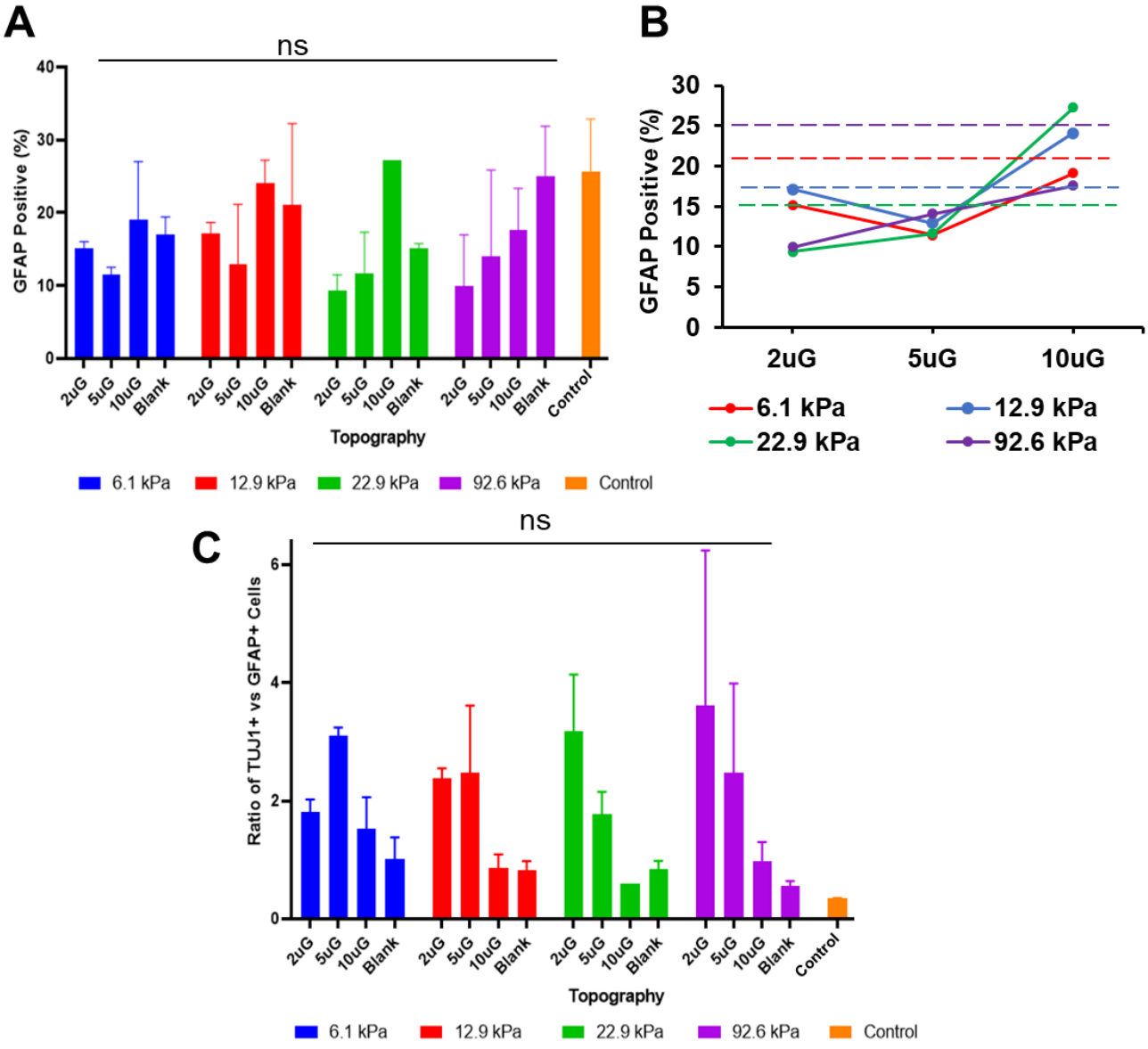

Figure 4.4 – Astrocyte lineage commitment gauged by percentage of cells positive for glial acidic fibrillary protein (GFAP) on gels of various stiffnesses with gratings of various dimensions. (A) Between and within stiffness and topography groups pairwise comparisons of percent GFAP+ cells. No significant differences were detected. (B) Interaction plot of percent GFAP+, topography and stiffness with dashed lines indicating the blank for each stiffness. (C) Ratio of neuronal lineage commitment versus astrocyte lineage commitment. For A and C, data is shown as the average of N=2 biological replica plus SD. For B, data is shown as the average of N=2 biological replica. Gratings dimensions (width x height x spacing) are 2 x 2 x 2 µm for 2uG, 5 x 5 x 5 µm for 5uG and 10 x 10 x 10 µm for 10uG. . Blue = 6.1 kPa, red = 12.9 kPa, green = 22.9 kPa, purple = 92.6 kPa and orange = control.

Looking at the total number of TUJ1+ cells versus the total number of GFAP+ cells (TUJ1/GFAP), the relative propensity for substrates to influence lineage commitment can be gauged (Figure 4.4C). Neither topography nor stiffness were correlated with TUJ1/GFAP (r = 0.08), but their interaction T*S had a high degree of negative correlation (r = -0.77). Within each stiffness group, lineage commitment to the neuronal phenotype was preferred over the astrocyte phenotype on either the 2uG or 5uG pattern. For the stiffest gels, the 2uG pattern resulted in the highest TUJ1/GFAP, and for the softest gels the 5uG pattern resulted in the highest TUJ1/GFAP.

Figure 4.5 – Heat map of correlation coefficients between topography, stiffness, the interaction of topography and stiffness (T*S), percent beta tubulin III positive cells (TUJ1+), percent glial fibrillary acidic protein positive cells (GFAP+) cells, percent microtubule associate protein 2 positive cells (MAP2+), tendency to promote the neuronal lineage over glial lineage (TUJ1/GFAP), average neurite length (Length) and average branches per neurite (Branching).

4.3.2. Effect of stiffness and topography on neuronal maturation

The mature neuronal marker, MAP2, was used to gauge the rate of neuronal maturation. MAP2 was present on the glass coverslip control indicating that the cells were healthy and capable of maturation. All gels regardless of topography or stiffness had a higher percentage of MAP2+ cells compared to the glass coverslip control. ANOVA analysis of the percentage of MAP2+ cells indicated that both stiffness and topography had a significant effect ($p = 0.001$ for both) but their combined interaction did not have a significant effect ($p = 0.1$). Representative images of MAP2 expression on each stiffness and pattern combination can be seen in Figure 4.6. Pairwise comparisons and an interaction plot between factors and the percentage of MAP2+ cells can be found in Figure 4.7. The average percent of cells expressing MAP2 on each stiffness and pattern combination can be found in Table 4.1. Spearman correlation coefficients calculated between parameters and the percentage of cells expressing MAP2 can be found in Figure 4.5.

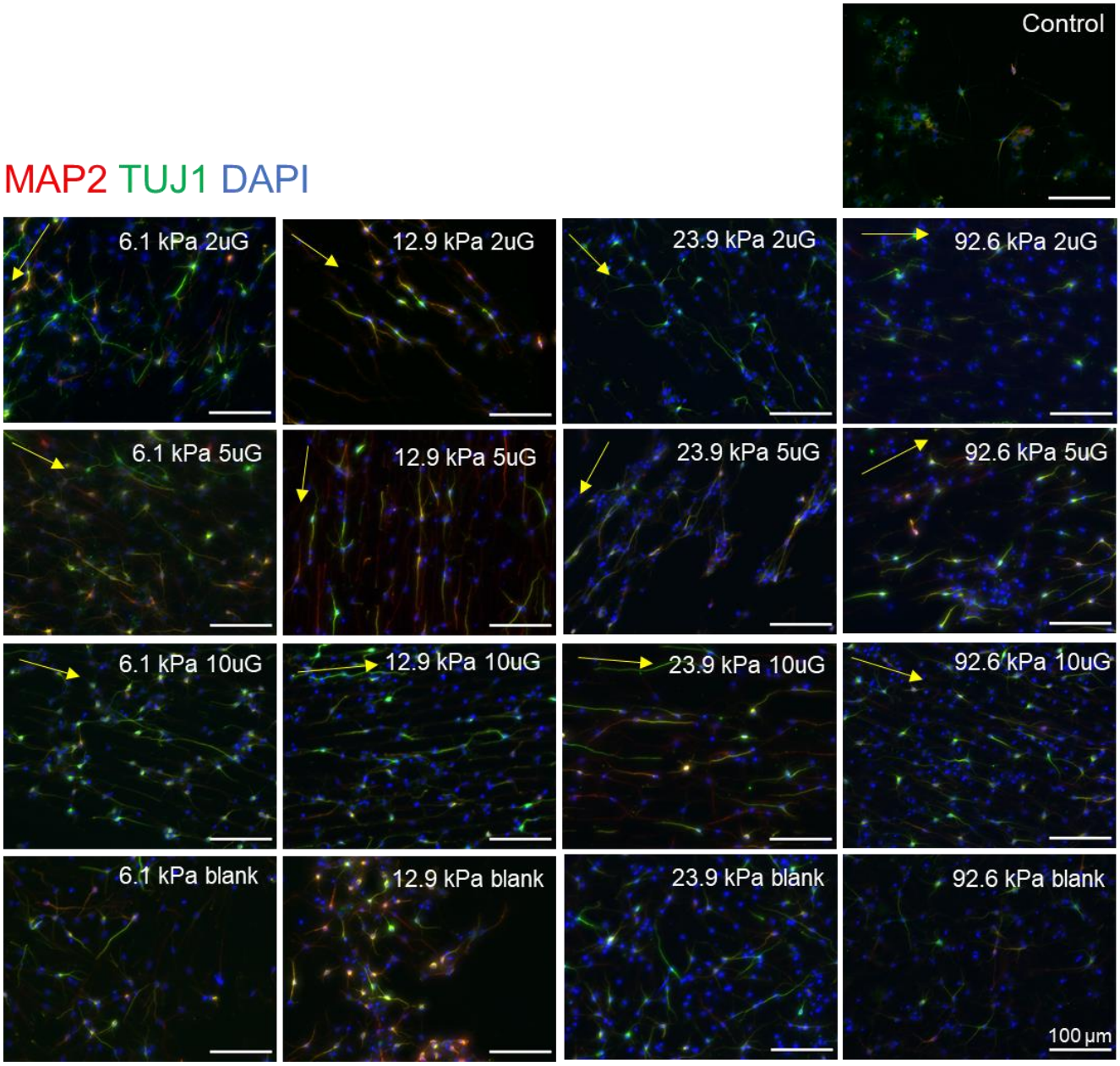

Figure 4.6 – Representative images of beta tubulin III (TUJ1, green) and microtubule associated protein 2 (MAP2, red) expression on gels of varying stiffness and topography. Young's modulus and topography are labelled in the top right corner for each image. Yellow arrows in the top left corner indicate the gratings direction. All scale bars represent 100 µm. Gratings dimensions (width x height x spacing) are 2 x 2 x 2 µm for 2uG, 5 x 5 x 5 µm for 5uG and 10 x 10 x 10 µm for 10uG. Blank refers to gels with no pattern. The control is a glass coverslip.

Topography had a moderate positive correlation with percent MAP2+ ($r = +0.46$). In Figure 4.7B, a curvilinear relationship between percent MAP2+ and topography can be observed for the 6.1 kPa gel. The stiffer gels seems to have a more linear relation. Analyzing effect of topography within stiffness groups, it can be observed that in the two softest groups topography makes the most notable impact on percentage of MAP2+ cells. The only significant difference within a stiffness group, was the higher percentage of MAP2+ cells on the 5uG pattern compared to the blank on the 6.1 kPa gel ($p = 0.0025$). As with the percentage of TUJ1+, the percentage of MAP2+ cells was highest on the 6.1 kPa gel with 5uG pattern. On this gel stiffness, as topography dimensions decreased or increased from 5uG, the percentage of MAP2+ cells decreased. The 2uG and 10uG pattern on this gel had similar effects. Looking at the 12.9 kPa gel, again the percent MAP2+ has a pattern similar to that of percent TUJ1+ on this gel. On this gel stiffness, the highest percentage of MAP2+ cells was seen on the 2uG pattern, and the percent positive decreased as pattern feature size increased. The percentages of MAP2+ cells on the 5uG and 10uG samples were closer to one another, compared to what was seen in the TUJ1 analysis though. Looking at the 22.9 kPa and 92.6 kPa gels, the overall percentage of MAP2+ cells notably decreased. Even with patterns, on these gels the percentage of MAP2+ cells was similar to that of the 6.1 kPa and 12.9 kPa blank gels. Patterns seemed to have minimal effect on these gels as the percentage of MAP2+ cells, was also like that of their own respective blanks.

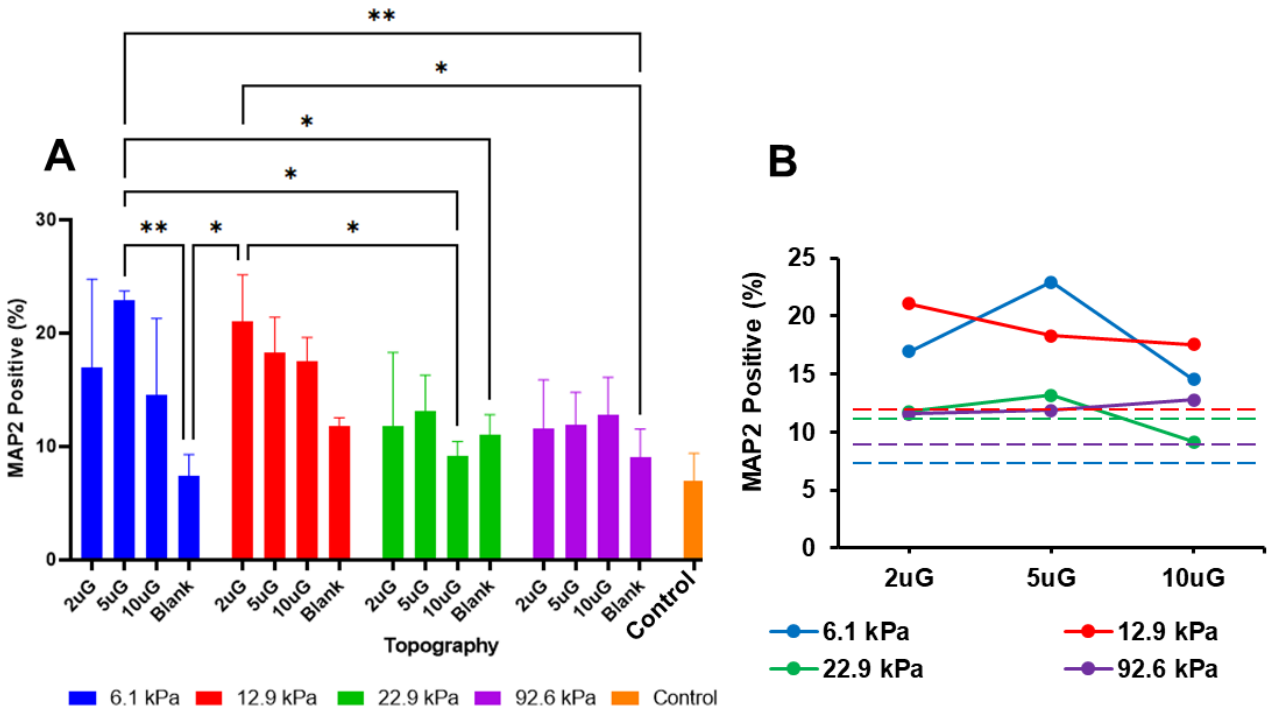

Figure 4.7 – Neuronal maturation gauged by percentage of microtubule associated protein 2 (MAP2) positive cells on substrates with various stiffnesses and gratings of various dimensions. (A) Between and within stiffness and topography group pairwise comparisons of percent MAP2+ cells. Data is shown as the average of N=3 biological replica with SD. The symbols *, **, ***, **** represent $p<0.05$, $p<0.01$, $p<0.001$, and $p<0.0001$, respectively. (B) Interaction plot of percent MAP2+, topography and stiffness with dashed lines indicating the blank for each stiffness. Data is shown as the average of N=3 biological replica. Gratings dimensions (width x height x spacing) are 2 x 2 x 2 µm for 2uG, 5 x 5 x 5 µm for 5uG and 10 x 10 x 10 µm for 10uG. Blue = 6.1 kPa, red = 12.9 kPa, green = 22.9 kPa, purple = 92.6 kPa and orange = control.

Stiffness had a moderate negative linear correlation with percent MAP2+ ($r = -0.45$). While there were no significant differences between samples with same pattern on gels of different stiffness, in general a trend can be observed that percent MAP2+ tends to decrease as stiffness increases. Looking at specific patterns, both the 2uG and 10uG patterns had the highest percentage of MAP2+ cells on the 12.9 kPa gel. The 5uG pattern had the highest percentage of MAP2+ cells on the 6.1 kPa gel. Comparing the blanks, the highest percentage of MAP2+ cells can be seen on the 12.9 kPa gel and the lowest on the 6.1 kPa blank, but these differences were small and not statistically significant.

This interaction T*S had a moderate negative linear correlation with percent MAP2+ ($r = -0.47$), indicating as T*S increases, percent MAP2+ decreases. Because topography alone had a positive correlation with percent MAP2+, and stiffness alone had a negative correlation with MAP2+, the negative direction of the T*S correlation, implies that if stiffness increases and topography is held constant, the size of the positive effect of the topography is weakened. This can be seen in Figure 4.7B as the relation between topography and percent MAP2+ becomes flattened as stiffness increases implying that the effect of topography is weakened.

4.3.3. Effect of stiffness and topography on neuronal morphology

Neurite length and number branches per cell were used to gauge the effect of stiffness and topography on resulting neuronal morphology and by extension maturation. ANOVA analysis indicated that only the T*S interaction had a significant effect on neurite length ($p = 0.0002$). Topography and stiffness individually, were not significant ($p > 0.07$). However, ANOVA for branching indicated all three factors, stiffness, topography, and their interaction, were significant ($p < 0.005$). Of all the gels, the longest average neurite length was seen on the 6.1 kPa gel with 5uG pattern. However, it should be noted that the coverslip control had the second longest average neurite length. Of all the gels, the highest rate of branching was seen on the 6.1 kPa gel with 5uG pattern. The highest overall rate of branching was seen on the coverslip control. In general, on patterns, neurites tended to align with the topography and on blanks neurites spread in random directions (Figure 4.8). There tended to be more instances of neurites travelling perpendicularly to gratings on soft substrates with small patterns or on stiff substrates with larger patterns. Branches tended grow in random directions on blank gels regardless of stiffness (Figure 4.8). On patterned gels, branches would extend perpendicular to the grooves but eventually follow the grooves. The values of average neurite lengths and average number of branches per cell can be found in Table 4.3.

Topography had a low degree of correlation with neurite length ($r = +0.17$). However, it is likely this relation is not linear as a curvilinear relationship between neurite length and topography can be observed Figure 4.7B. A positive curvilinear relation can be seen for the 6.1 kPa gels but begins to invert with the 12.9 kPa gel and then become a negative curvilinear relation for the two stiffer. Within stiffness groups, the only group that a significant difference in length due to topography was the 6.1 kPa group (Figure 4.7A, Table 4.3). In this group the average neurite lengths of the 5uG and 2uG patterns were significantly higher than the 10uG pattern ($p < 0.0001$ and $p = 0.046$, respectively). Only the 5uG pattern had a significantly higher average length than the blank though ($p = 0.029$). The 10uG pattern had the shortest average length of all groups in the 6.1 kPa gel. There was no significant difference between the 5uG and 2uG pattern. In the other stiffness groups, the differences between average neurite length of patterns tended to decrease as stiffness increased, but these differences were not statistically significant.

Stiffness had a moderate negative linear correlation on neurite length ($r = -0.42$). For the 2uG and 5uG patterns, and the blank, as stiffness increased, their average neurite length fell. The average neurite length on 6.1 kPa gel with 5uG pattern was significantly longer than that of the 12.9 kPa gel and 22.9 kPa gel with the 5uG pattern ($p = 0.013$ and $p < 0.0001$, respectively). No significant differences in length were observed between stiffnesses for the 2uG pattern and the blank. For the 10uG pattern, between the 6.1 kPa gel and the 13.2 kPa gel neurite length significantly increased ($p = 0.035$). The average lengths on the 22.9 kPa and 92.6 kPa gels with 10uG pattern were also greater than that of the 6.1 kPa 10uG sample, though not statistically significant.

The T*S interaction had a moderate negative correlation with neurite length ($r = -0.39$). This indicates that increasing stiffness dampens the positive effect of topography on neurite length and its dampening power increases with topography size. Conversely this indicates topography

dampens the negative effect of increasing stiffness, and its dampening power increases as stiffness decreases.

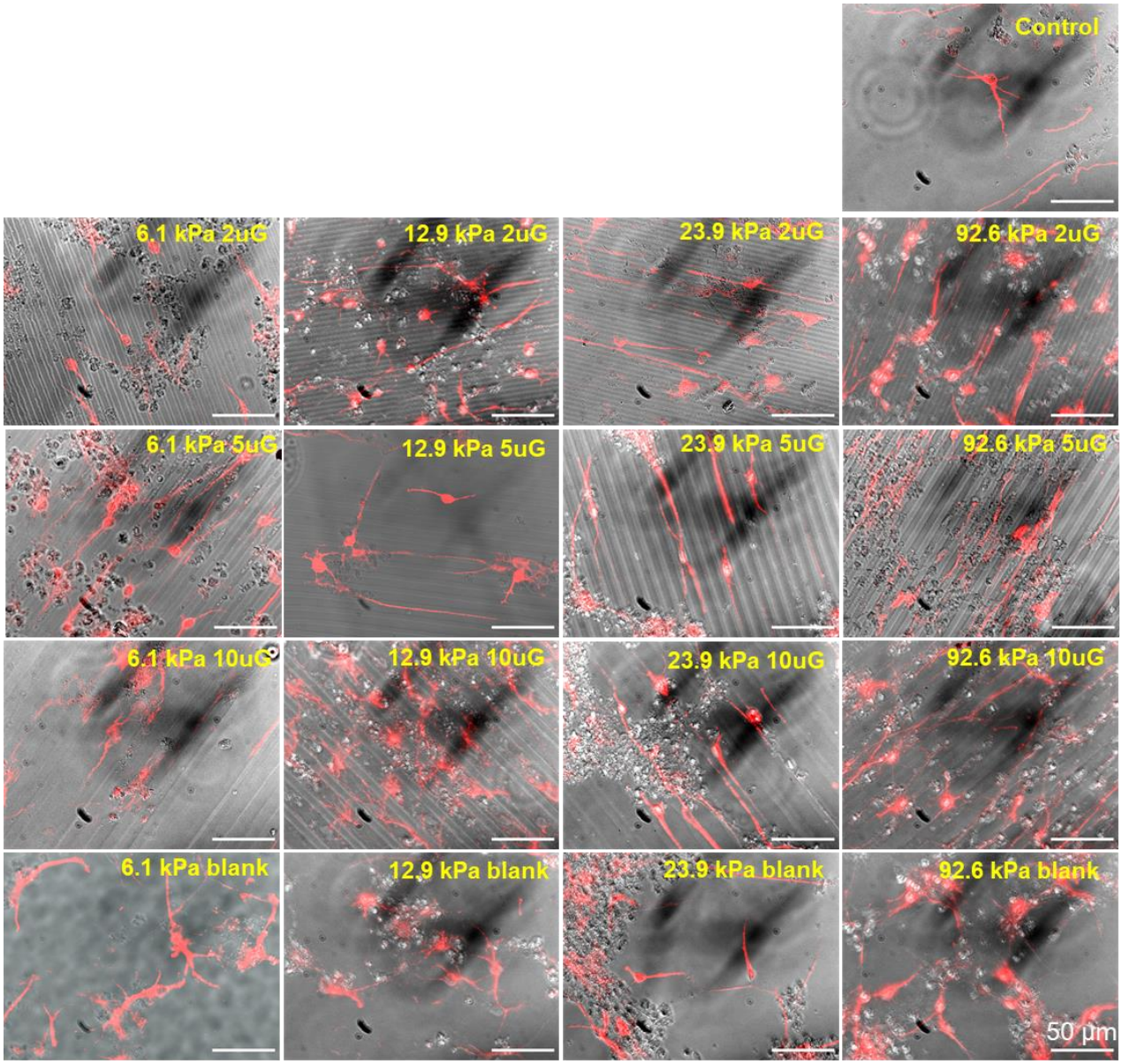

Figure 4.8 – Representative images of microtubule associated protein 2 (MAP2, red) positive neurites' length, branching and orientation on gels of various stiffnesses with topographies of various dimensions. Young's modulus and topography are labelled in the top right corner for each image. All scale bars represent 50 µm. Gratings dimensions (width x height x spacing) are 2 x 2 x 2 µm for 2uG, 5 x 5 x 5 µm for 5uG and 10 x 10 x 10 µm for 10uG. Blank refers to gels with no pattern. The control is a glass coverslip.

Table 4.3 – MAP2+ neurite length and MAP2+ branches per cell on the different stiffnesses and topographies. Data collected from N=3 replicates and shown as average ± 95% CI.

Stiffness	Topography	Average Neurite Length (μm)	Average No. Branches
Control		77.9 ± 12.1	5.1 ± 0.7
6.1 kPa	2uG	68.9 ± 8.0	4.1 ± 0.5
	5uG	80.0 ± 7.5	5.0 ± 0.5
	10uG	57.9 ± 5.2	3.4 ± 0.4
	Blank	67.3 ± 8.3	4.8 ± 0.7
12.9 kPa	2uG	68.2 ± 6.5	4.0 ± 0.3
	5uG	70.7 ± 5.7	3.5 ± 0.3
	10uG	68.8 ± 6.1	3.2 ± 0.3
	Blank	60.9 ± 4.9	3.5 ± 0.3
22.9 kPa	2uG	66.2 ± 6.6	3.9 ± 0.4
	5uG	61.3 ± 5.5	2.8 ± 0.2
	10uG	66.1 ± 5.8	3.6 ± 0.4
	Blank	62.7 ± 4.2	3.7 ± 0.3
92.6 kPa	2uG	64.4 ± 6.8	3.8 ± 0.5
	5uG	61.8 ± 7.5	4.0 ± 0.7
	10uG	66.7 ± 4.6	4.2 ± 0.3
	Blank	59.0 ± 7.2	4.4 ± 0.5

Topography had a moderate negative correlation with neurite branching ($r = -0.35$). Significant differences between patterns were seen in the 6.1 kPa, 12.9 kPa and 22.9 kPa stiffness groups but not in the 92.6 kPa group (Figure 4.9C, Table 4.3). In the 6.1 kPa group, the 5uG pattern had significantly higher branches per cell compared to the 2uG pattern ($p = 0.008$) and 10uG pattern ($p < 0.0001$) but not the blank. In the 12.9 kPa group, the highest average branching was observed on the 2uG pattern. On this stiffness, the average branching with the 2uG pattern was significantly greater than that of the 10uG pattern ($p = 0.04$) but was not significant compared to the blank. The 5uG pattern and the blank had the same average branching. On the 22.3 kPa gels, the 2uG pattern, 10uG pattern and the blank had significantly higher branching compared to the 5uG pattern ($p = 0.003$, $p = 0.025$, $p = 0.001$, respectively). On

the 92.6 kPa gel, there was no significant difference amongst the topographies however the blank had the highest branching.

Stiffness could not be correlated with neurite branching using the Spearman correlation coefficient ($r = 0$) despite ANOVA indicating it had a significant effect. Within the 2uG pattern group, average branching decreased with stiffness, but the change was very minimal and not statistically significant (Figure 4.7C, Table 4.3). The 5uG pattern group saw the most significant variation depending on stiffness. In this group, the 6.1 kPa gel with 5uG had significantly higher average branching than all other stiffnesses with 5uG ($p = 0.036$ for 12.9 kPa 5uG and $p < 0.0001$ for both 22.9 kPa and 92.6 kPa 5uG). In addition, for this pattern both the 12.9 kPa and 92.6 kPa gels had significantly higher average branching than the 22.9 kPa gel ($p = 0.047$ and $p = 0.006$, respectively). For the 10uG pattern, the highest average branching was seen on the 92.6 kPa gel and decreased as stiffness decreased. Between the 6.1 kPa and 92.6 kPa gel ($p = 0.007$) and the 12.9 kPa gel and 92.6 kPa gel ($p = 0.0007$) this decrease was significant. For the blank samples, the average branching peaked on the 6.1 kPa gel, reached a minimum on the 12.9 kPa gel then increased again as stiffness increased. The 6.1 kPa blank had significantly higher average branching compared to the 12.9 kPa gel ($p < 0.0001$) and the 22.9 kPa gel ($p = 0.0004$), and similar average branching compared to the 92.6 kPa gel.

The interaction of T*S was also not correlated with branching despite being noted as significant by ANOVA analysis. However, looking at Figure 4.9D, it is clear there is interaction between plots as they cross many times. Looking at the interaction plot, it can be seen that the 2uG pattern and 10uG pattern tend to perform consistently regardless of pattern but the performance of the 5uG pattern is notably more affected by stiffness.

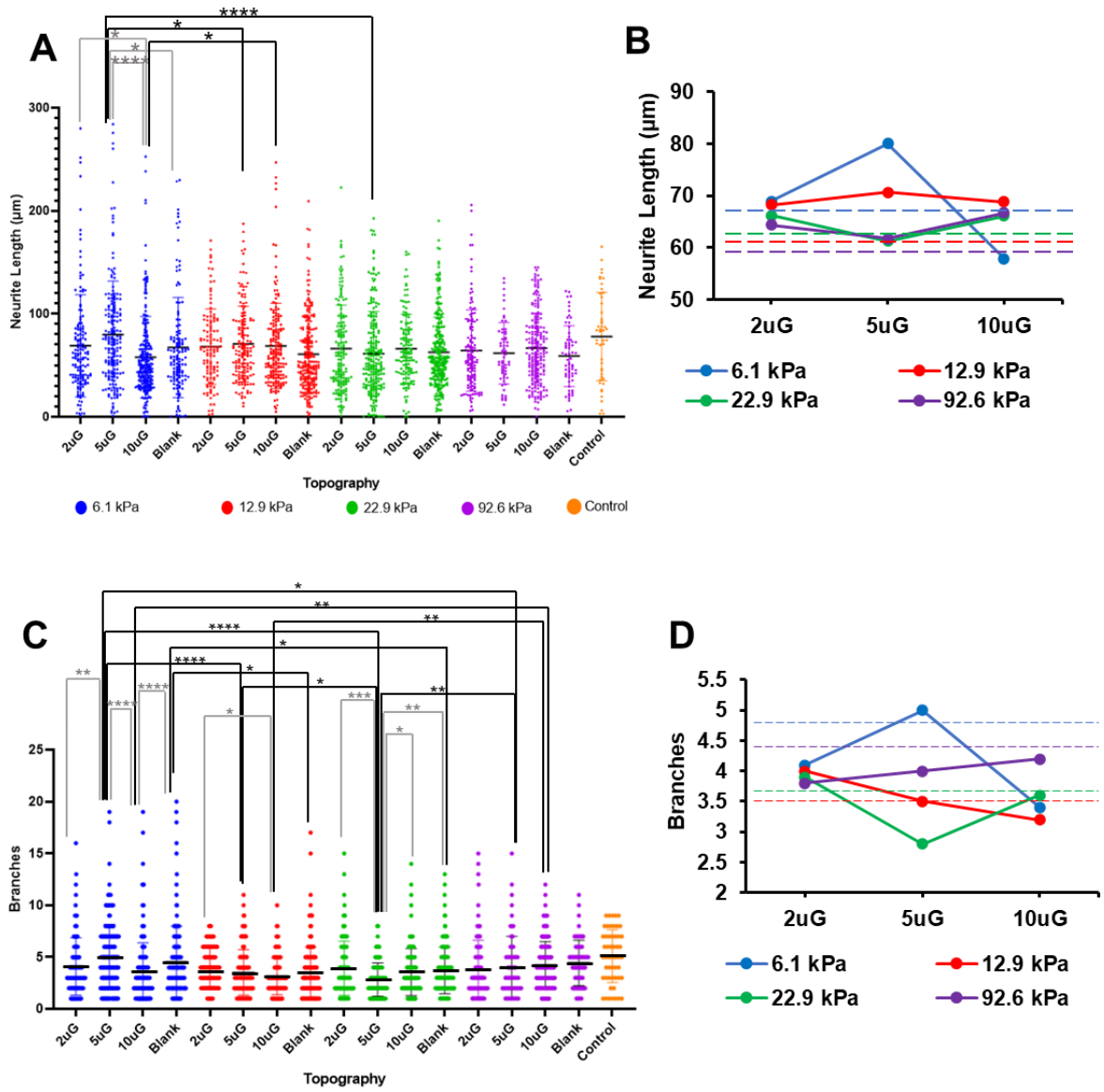

Figure 4.9 – Average neurite length and branching on gels of various stiffness and topographies. (A) Average neurite length. (B) Interaction of stiffness and topography on average neurite length with dashed lines indicating the blank for each stiffness. (C) Average branches per neurite per cell. (D) Interaction of stiffness and topography on average branches per neurite per cell with dashed lines indicating the blank for each stiffness. Approximately 50 to 200 cells were analyzed for each pattern and stiffness combination. The symbols *, **, ***, **** represent $p<0.05$, $p<0.01$, $p<0.001$, and $p<0.0001$, respectively. Blue = 6.1 kPa, red = 12.9 kPa, green = 22.9 kPa, purple = 92.6 kPa and orange = control.

4.4. Discussion

Topography and stiffness have independently been shown to have a significant effect on neuronal differentiation. They can enhance neuronal differentiation rate, neuronal lineage commitment and morphology of resulting neurons.[70, 75, 77, 145, 146, 149, 150] Further they are inexpensive tools that can be implemented into a variety of biomaterials for this purpose. However, there are few studies that have investigated them together. Combined interaction studies have been rarely performed due to technical difficulties in pattern soft hydrogels that allow for stable long-term conjugation of surface ECM. As outline in Chapter 3, the platform used here overcomes these obstacles and allows for studies of the combined interactions over a period of 14 days.

An understanding of the combined effects of topography and stiffness and their interaction is important for a few reasons. First, it is impossible to impart only the cue of topography as topography requires a substrate which will have some characteristic stiffness. Thus, when designing biomaterials with topography, it is important to consider how the effect of topography may differ with substrate stiffness. Second, it allows for the opportunity to tune multiple biophysical cues, so they act synergistically and further improve our control of neuronal differentiation. Lastly, it can help us to better understand the mechanotransduction pathways involved in responses to stiffness and topography and how these pathways may interact. To these ends, we investigated how the factors of topography, stiffness and their combined interaction T*S affects neuronal differentiation. Specifically, how they would affect two key parameters of neuronal differentiation: neuronal lineage commitment and maturation rate. We hypothesized that effects of stiffness and topography on neuronal differentiation would be dependent on one another for both parameters.

First, we looked at how stiffness, topography and their combined interaction may affect neuronal lineage commitment. A common challenge when using biomaterials to promote neuronal

differentiation of neural progenitor cells, is to ensure that they differentiate into the correct phenotype. NPC can become either neurons or glial cells however, they have a propensity to differentiate into astrocytes. [119, 231, 232] This is problematic because in lesions of the central nervous system reactive astrocytes create scar tissue that significantly impedes neuronal regeneration preventing rescue of proper tissue functioning. Further, when NPC are used *in vitro* as a neuronal cell source, this reduces the overall yield. Thus, it is of interest to see how simultaneous applications of topography and stiffness may affect neuronal lineage commitment versus astrocyte lineage commitment.

ANOVA indicated topography, stiffness and T*S had a significant effect on TUJ1 expression but only topography had a significant effect on GFAP expression. There was a moderate negative correlation between stiffness and percent TUJ1, though only a low correlation could be drawn between percent TUJ1+. Percent GFAP+ was not highly correlated with either stiffness or topography. Both percent TUJ1+ and percent GFAP+ were highly correlated with T*S, though in opposite directions. Comparing the propensity to select the neuronal lineage over the astrocyte lineage (TUJ1/GFAP) it was found that the interaction T*S had a high degree of negative correlation. This is the same correlation direction as T*S with percent TUJ1+ (negative) and the opposite correlation direction as T*S with percent GFAP (positive). This implies that the interaction effect helps to not only further promote neuronal lineage commitment but also suppress astrocyte lineage commitment, increasing the overall fraction of TUJ1+ cells compared to GFAP+ cells. However, it is important to note that this does not necessarily mean the smallest topography is automatically the optimal topography. Rather, the interaction seems to modify the maxima or of the curve between topography and percent TUJ1 or GFAP, for a given stiffness. While Figure 4.3B shows negative linear relations between topography size and percent TUJ1+ it is suspected that if smaller dimensions were included in this study, we may see curvilinear relations for the stiffest gels as well. Indeed, many studies of topography dimensions performed on substrate in

the high kPa range have indicated that nanotopographies are optimal for enhancing neuronal differentiation.[67] Thus, smaller topographies may be required to see a curvilinear relation and identify a maxima for the stiffer gels.

Taking this into account it seems the interaction term will amplify the effect of a given stiffness, and this amplification will increase as topography increases. In the opposite direction, the interaction term will suppress the effects of a given stiffness as topography decreases. In terms of its effect on topography, the interaction term will reduce the effect of a given topography as stiffness increases and enhance the effect of a given topography as stiffness decreases. Taking these interpretations together, the shift in peak of the curve between percent TUJ1+ and percent GFAP+ for the 6.1 kPa gel compared to the other stiffer gels can contextualized. It has been suggested that smaller patterns may better enhance neuronal differentiation lineage commitment as they better constrict cells, which limits activation of Rho GTPases reducing contractility and focal adhesion formation. [136, 149, 152, 233-235] However, many of the studies that suggest this have been polydimethylsiloxane [145, 146, 235-238], glass [233] or silicon wafers[69] which are very stiff (high kPa to GPa). Stiff substrates have been shown to active Rho GTPases.[70, 119, 120] Perhaps, as these are very stiff substrates, the more constrictive and forceful the topography, the less its effects will be reduced by the high stiffness, the less it will amplify the incompatible substrate stiffness, and the more it will suppress the effects of this high stiffness. Thus, the small patterns will be more effective relative to less constrictive patterns on these very stiff substrates. Future studies should compare the effects nanotopographies and microtopographies soft substrates, to determine which are optimal for soft substrates (1-10 kPa) and stiff substrates (> 10 kPa).

There have been very few studies of topography on soft substrates, but on unpatterened soft substrates, the neuronal lineage is favoured as stiffness decreases. This is attributed to the fact that soft substrates tend to reduce contractility and the formation of focal adhesions. Most

studies have indicated that optimal stiffnesses for enhancing neuronal lineage commitment over astrocyte lineage commitment are in the range of 1-10 kPa which is close to *in vivo* in brain tissue elasticity. [108, 113-119] Indeed, in this study, the blank 6.1 kPa gel performed the best of all the blank gels. More interesting though, is that this further support that the interaction T*S is responsible for the shift in the peak of the curve between percent TUJ1+ and percent GFAP+ for the 6.1 kPa gel compared to the other stiffer gels. According to the literature the 6.1 kPa gel should be soft enough to promote neuronal commitment alone, and the interaction term indicates that the effect of stiffness is dampened as topography dimensions decrease. Further the interaction term indicates that the effect of stiffness is amplified as topography increases. Thus, we find for the 6.1 kPa gel which is capable of enhancing neuronal lineage commitment alone, its effect is promoted by the 5uG pattern and suppressed by the 2uG pattern. The enhancement effect likely dips for the 10uG pattern as the 10uG pattern is already at the upper limit of dimensional size to interact with cell soma (12 ± 3 μm). [73, 75, 239] It likely already contributed little to the preventing the activation of Rho GTPases or other mechanotransduction pathways so the amplification from the gel was not enough for the 10uG's effects to become significant, as was seen with the 5uG pattern. Comparing the 10uG pattern across stiffnesses though, the percent TUJ1+ increased as stiffness decreased. On the 12.9 kPa gels and higher, which would tend towards enhancing the astrocyte lineage commitment over the neuronal lineage commitment (as seen on the blank), the 2uG pattern is the only one constrictive enough to counteract this tendency of the gels. Further the power of this constriction is enhanced as stiffnesses decreases, thus the 13.2 kPa gel with 2uG pattern has higher percent TUJ1+ compared to the two stiffer gels with 2uG pattern.

Next, looking at how topography, stiffness, and T*S affect maturation, it was found that the 5uG pattern also best promoted maturation on the softest substrate. On the 6.1 kPa gel, the 5uG pattern had the highest percent MAP2+, the longest average neurite length and the largest number of branches per cell. Similar to percent TUJ1+, percent MAP2+ was negatively correlated

with stiffness, positively correlated with topography and negatively correlated with the T*S interaction (Figure 4.5). Thus, the interaction term should amplify or suppress topography and stiffness as previously mentioned when discussing lineage commitment. However, rather than shifting the curve peaks in Figure 4.7B, it tended to flatten the curves as stiffness increased. However, a shift in peak maxima due to the interaction effect was seen for the two softer substrates. Taken together this implies that smaller patterns than those studied here are required for notable changes in percent MAP2+ on stiffer substrates, but topographies in the dimensions studied here are suitable for enhance percent MAP2+ on soft substrates. Again, similar to lineage commitment, it seems like the 2uG pattern reduces the inherently supportive nature of soft gels but compensates for the inherently unsupportive nature of stiff gels. The 5uG pattern enhances the supportive nature of the soft gel by not being overly constrictive but still allowing for some neurite guidance. Interestingly, some studies of topography have shown that the effect of topography is temporal and while initial lineage commitment (on stiff surfaces) is improved by constriction, maturation is improved by freedom for neurites to move and create complex interactions with their neighbor like on isotropic patterns.[75, 101, 237] This seems to support the findings and proposed interactions in this study as the 5uG pattern on the 6.1 kPa gel enhanced both neuronal lineage commitment and maturation, the most of any stiffness and topography combination. Essentially it is optimized such that is just small enough to enhance lineage commitment without impeding the effects of the substrate while also being wide enough to allow neurons the freedom to move during maturation which is further supported by soft substrate stiffness. In other words, topography, and stiffness work together to promote initial lineage commitment and maturation by balancing each other's effects.

Looking at neurite length and branching, only the T*S interaction significantly affected neurite length, but all three factors affected neurite branching. Like the interaction plots for percent MAP2+ (Figure 4.7B), as stiffness increased, the curves of neurite length versus topography

flattened. However, unlike the percent MAP2+ plots, this flattening started with the 12.9 kPa stiffness. This seems to imply that neurite extension is more sensitive to stiffness than percent MAP2+ and smaller gratings than those studied here are required for notable changes in neurite length. The trend of 5uG significantly enhancing neuronal differentiation on the 6.1 kPa gel compared to other patterns and the blank was again seen with neurite length though. As mentioned, when discussing percent MAP2+ previously, this is because the soft substrate supports neurite extension, and the gratings are wide enough to allow them to move in various directions without needing to bend at large angles. It has been shown that as depth increases neurites tend to avoid travelling perpendicular to gratings. However as noted in chapter 3, if there is something at the base of the gratings that can support them, they are more likely to cross deeper gratings. Perhaps in this case, because the gratings are farther apart the neurites' entrance angle is not as great as on narrower gratings, and the soft substrate at the bottom then further supports them. Additionally, the gratings are close enough that should a neurite find it energetically favourable to travel in the direction of the grating it can find a grating wall and travel parallel to it, using it for support. This notion is further support by the observation that the 6.1 kPa gel with 5uG pattern also had the highest rate of branching.

Overall, a balance between the effects of topography and stiffness due to their interaction has been demonstrated for lineage commitment and maturation. Further, because it is known that both topography and stiffness act through similar mechanotransduction pathways, it is likely that the interaction observed in this study is due to some balance of activation and suppression of these pathways. Future studies should investigate this interaction at the level of mechanotransduction proteins, which could allow for enhanced optimization of topography and stiffness pairings and better understanding of how in vivo cells respond to a multitude of cues simultaneously.

4.5. Conclusions

In conclusion, this chapter shows that while the effects of topography and stiffness independently can affect neuronal differentiation, they also significantly interact and modulate one another's ability to control neuronal differentiation. This is important to take into account as topography cannot be imparted independent of stiffness in biomaterials and as shown here certain topography and stiffness combinations work better than others. For topography there is no one size fits all. We found that the medium topography was optimal on the softest gel and the smallest topography was optimal on the stiffer gels, for enhancing neuronal lineage commitment and maturation. This may allow for highly effective biomaterials that are easier to fabricate as larger topographies are easier to impart than smaller topographies. The mechanotransduction pathways affected by topographical and stiffness cues have begun to be investigated, but this study shows that there is further needed to study how these pathways handle multiple cues at once. This can help to better optimize topography and stiffness pairings, and better understand how cells interact with their microenvironment *in vivo*. Overall, even if not optimizing stiffness and topography pairings, when designing biomaterials with topography, the combinatory effect of topography and stiffness should be taken into account.

CHAPTER

5 General Conclusions and Recommendations

5.1. General Conclusions

Biophysical cues such as topography and stiffness are powerful tools that can be used to enhance neuronal differentiation, making them particularly important in the field of tissue engineering and regenerative medicine. These enhancement techniques are important for the development of cell-based therapies for the treatment of neurological diseases, neuronal regeneration, and in vitro platforms for fundamental neurological studies, drug-screen platforms, disease modelling and precision medicine platforms Due to the successful application of topography and stiffness independently for enhancing neuronal lineage-directed differentiation, their use for other forms of neuronal generation, and their combined effect on lineage-directed differentiation is of great interest. It was hypothesized that biophysical cues, such as topography, could be able to enhance direct neuronal reprogramming. Further it was hypothesized, that when topography and stiffness are combined there would be an interaction effect, that would influence how these parameters affect neuronal regeneration. Indeed, both hypotheses have been addressed by the findings of this study.

The findings of this study indicate that topography can be used to enhance nonviral BAM factor direct neuronal reprogramming of embryonic mouse fibroblasts using a polyplex carrier. Hierarchical patterns showed a significant effect on increasing neuronal reprogramming efficiency. We speculated that the base pattern of microscale gratings could be responsible for improving initial expression of BAM factors and neuronal marker, TUJ1 and MAP2, expression in iN cells. The secondary pattern on the hierarchical pattern, the 250nG perpendicular to the base gratings, was speculated to be responsible for promoting subsequent maturation and development of iN cells. Using hierarchical patterns, we were able to increase efficiency with one dose to a level that was similar to previous studies using five doses. The combination of multiple doses and topography may have the potential to produce an even more efficient system.

To further investigate biophysical cues and how they could enhance biomaterials for neuronal generation, we developed a substrate that allowed for long-term, stable attachment of neural progenitor cells and subsequent neuronal and glial cells. This was done using a method of electrostatically coating ECM to polyacrylamide copolymers using a charged polypeptide intermediate conjugated to the gel with carbodiimide chemistry. The platform also had reliably modifiable stiffness and could be patterned with microscale topographies. Using this platform, we studied the combined effects of stiffness and topography on lineage-based differentiation and found a notable interaction effect. Not only does this help to better explain how cells respond to the multitude of biophysical cues they receive *in vivo*, but the findings may also help to create better biomaterials. Topography cannot be imparted independently of stiffness and thus it is important to understand how they affect one another. Here we found we found that the medium topography was optimal on the softest gel and the smallest topography was optimal on the stiffer gels, for enhancing neuronal lineage commitment and maturation. Thus, the effects of topography are affected by the stiffness they are on which is important to keep in mind when both studying and applying topography to control neuronal differentiation.

5.2. Recommendations

There is a variety of future work that can be done to expand on the novel findings of this thesis. First, for the application of topography for direct neuronal reprogramming, it is of interest to see if doses and topography could be optimized to further enhance reprogramming efficiency to levels that bring it closer to being clinically feasible investigate. Additionally, for clinical applications, it is important to investigate how direct neuronal reprogramming may be affected by topography in a 3D environment. This could be done using electro spun fiber scaffolds which are important tools for mimicking *in vivo* biophysical cues. As the goal of many direct neuronal

reprogramming endeavours is *in situ* neuronal repair, it is important to also investigate whether the enhancement effects from topography are also seen *in vivo*.

Further for methods of neuronal regeneration that are better understood, such as lineage-based differentiation or non-lineage-based differentiation, the combined effect of topography and stiffness should be further investigated. We were able to use our developed PAA-ACA copolymer platform to test the effect of stiffness and topography, however the platform itself still has room for improvement. It may be useful to see if PLO could be using in place of PLL as the polypeptide intermediate as it provokes less of an immune response *in vivo*. The suspected effects of PLO being unsuitable due to steric hinderance could be investigated with Fourier Transform Infrared Spectroscopy.

Between stiffness and topography and interesting interaction effect was observed here, but an in-depth understanding of this interaction on the scale of mechanotransduction pathways may be able to help better utilize and optimize this effect. For example, while it was speculated in Chapter 4 as to why optimal topography may change with stiffness, an analysis of mechanotransduction pathways may help to better explain it. While this analysis would be very helpful, it is tedious and time consuming so it would likely only be worthwhile if we can show that these interactions also affect human cells. Thus, as our platform has been shown to support long term adherence of human neural progenitor cells and their differentiated progeny, it is recommended that a combined effects study be done with human cells as well. This will allow for more in-depth analysis as to how this interaction affects maturation, such as electrophysiological functioning of neurons (which cannot be done with the mouse neural progenitor cell derived neurons). Further it will help to better translate the potential use of the interaction effect towards clinical applications

REFERENCES

1. D. Jain, S. Mattiassi, E. L. Goh and E. K. Yim, *Neural regeneration research*, 2020, **15**, 573.
2. K. Hoehn and E. N. Marieb, *Human anatomy & physiology*, Benjamin Cummings San Francisco, 2010.
3. N. Baumann and D. Pham-Dinh, *Physiological Reviews*, 2001, **81**, 871-927.
4. L. F. Eng, R. S. Ghirnikar and Y. L. Lee, *Neurochemical Research*, 2000, **25**, 1439-1451.
5. D. E. Korzhevskii and O. V. Kirik, *Neuroscience and Behavioral Physiology*, 2016, **46**, 284-290.
6. E. Draberova, Z. Lukás, D. Ivanyi, V. Viklický and P. Dráber, *Histochemistry and cell biology*, 1998, **109**, 231-239.
7. C. D. Katsetos, A. Frankfurter, S. Christakos, E. L. Mancall, I. N. Vlachos and H. Urich, *Journal of Neuropathology & Experimental Neurology*, 1993, **52**, 655-666.
8. K. Fenrich and T. Gordon, *Canadian Journal of Neurological Sciences / Journal Canadien des Sciences Neurologiques*, 2004, **31**, 142-156.
9. C. E. Schmidt and J. B. Leach, *Annual Review of Biomedical Engineering*, 2003, **5**, 293-347.
10. J. B. Hutchins and S. W. Barger, *The Anatomical Record*, 1998, **253**, 79-90.
11. K. Belanger, T. M. Dinis, S. Taourirt, G. Vidal, D. L. Kaplan and C. Egles, *Macromolecular Bioscience*, 2016, **16**, 472-481.
12. H. M. Kaplan, P. Mishra and J. Kohn, *Journal of Materials Science-Materials in Medicine*, 2015, **26**.
13. A. R. Nectow, K. G. Marra and D. L. Kaplan, *Tissue Engineering Part B: Reviews*, 2012, **18**, 40-50.
14. G. M F, M. M, H. S and W. S. Khan, *The open orthopaedics journal*, 2014, **8**, 199-203.
15. S. A. Busch and J. Silver, *Current Opinion in Neurobiology*, 2007, **17**, 120-127.
16. J. Silver and J. H. Miller, *Nature Reviews Neuroscience*, 2004, **5**, 146-156.
17. H. S. Kwon and S.-H. Koh, *Translational Neurodegeneration*, 2020, **9**, 42.
18. E. A. Huebner and S. M. Strittmatter, *Results and problems in cell differentiation*, 2009, **48**, 339-351.
19. K. Goncalves and S. Przyborski, *Brain and neuroscience advances*, 2018, **2**, 2398212818818071-2398212818818071.
20. Y. Shi, H. Inoue, J. C. Wu and S. Yamanaka, *Nature Reviews Drug Discovery*, 2016, **16**, 115.
21. D. Dutta, I. Heo and H. Clevers, *Trends in Molecular Medicine*, 2017, **23**, 393-410.
22. Y. Avior, I. Sagi and N. Benvenisty, *Nature Reviews Molecular Cell Biology*, 2016, **17**, 170.
23. G. Bain, D. Kitchens, M. Yao, J. E. Huettner and D. I. Gottlieb, *Developmental biology*, 1995, **168**, 342-357.
24. E. Abranches, M. Silva, L. Pradier, H. Schulz, O. Hummel, D. Henrique and E. Bekman, *PLOS ONE*, 2009, **4**, e6286.
25. Y. Shi, H. Inoue, J. C. Wu and S. Yamanaka, *Nature Reviews Drug Discovery*, 2017, **16**, 115-130.
26. K. Takahashi and S. Yamanaka, *Cell*, 2006, **126**, 663-676.

27. M. M. Steward, A. Sridhar and J. S. Meyer, in *New Perspectives in Regeneration*, eds. E. Heber-Katz and D. L. Stocum, Springer Berlin Heidelberg, Berlin, Heidelberg, 2013, pp. 163-191.
28. M. Ghaedi and L. E. Niklason, *Methods in molecular biology (Clifton, N.J.)*, 2019, **1576**, 55-92.
29. H. Nam, K.-H. Lee, D.-H. Nam and K. M. Joo, *World journal of stem cells*, 2015, **7**, 126-136.
30. M. Gao, H. Yao, Q. Dong, H. Zhang, Z. Yang, Y. Yang, J. Zhu, M. Xu and R. Xu, *Scientific Reports*, 2016, **6**, 29955.
31. Y. Tang, P. Yu and L. Cheng, *Cell Death & Disease*, 2017, **8**, e3108-e3108.
32. T. Gorba and L. Conti, *Expert Opinion on Drug Discovery*, 2013, **8**, 1083-1094.
33. N. Anh Tuan, S. Mattiassi, M. Loeblein, E. Chin, D. Ma, P. Coquet, V. Viasnoff, E. H. T. Teo, E. L. Goh and E. K. F. Yim, *Biomedical Materials*, 2018, **13**.
34. O. Heese, A. Disko, D. Zirkel, M. Westphal and K. Lamszus, *Neuro-Oncology*, 2005, **7**, 476-484.
35. D. Doi, H. Magotani, T. Kikuchi, M. Ikeda, S. Hiramatsu, K. Yoshida, N. Amano, M. Nomura, M. Umekage, A. Morizane and J. Takahashi, *Nature Communications*, 2020, **11**, 3369.
36. R. Hernández, C. Jiménez-Luna, J. Perales-Adán, G. Perazzoli, C. Melguizo and J. Prados, *Biomolecules & therapeutics*, 2020, **28**, 34-44.
37. I. Ullah, R. B. Subbarao and G. J. Rho, *Bioscience reports*, 2015, **35**, e00191.
38. T. Vierbuchen, A. Ostermeier, Z. P. Pang, Y. Kokubu, T. C. Südhof and M. Wernig, *Nature*, 2010, **463**, 1035-1041.
39. S. Marro, Z. P. P. Pang, N. Yang, M. C. Tsai, K. Qu, H. Y. Chang, T. C. Sudhof and M. Wernig, *Cell Stem Cell*, 2011, **9**, 374-382.
40. K. Tanabe, C. E. Ang, S. Chanda, V. H. Olmos, D. Haag, D. F. Levinson, T. C. Südhof and M. Wernig, *Proceedings of the National Academy of Sciences*, 2018, **115**, 6470-6475.
41. M.-H. Liu, W. Li, J.-J. Zheng, Y.-G. Xu, Q. He and G. Chen, *Neural regeneration research*, 2020, **15**, 342-351.
42. J.-C. Yin, L. Zhang, N.-X. Ma, Y. Wang, G. Lee, X.-Y. Hou, Z.-F. Lei, F.-Y. Zhang, F.-P. Dong, G.-Y. Wu and G. Chen, *Stem Cell Reports*, 2019, **12**, 488-501.
43. L. Gao, W. Guan, M. Wang, H. Wang, J. Yu, Q. Liu, B. Qiu, Y. Yu, Y. Ping, X. Bian, L. Shen and G. Pei, *Stem Cell Reports*, 2017, **8**, 538-547.
44. K. Aravantinou-Fatorou and D. Thomaidou, in *Stem Cells and Tissue Repair*, Springer US, 2020, pp. 41-61.
45. O. Torper, U. Pfisterer, D. A. Wolf, M. Pereira, S. Lau, J. Jakobsson, A. Björklund, S. Grealish and M. Parmar, *Proceedings of the National Academy of Sciences*, 2013, **110**, 7038.
46. H. Wang, Y. Yang, J. Liu and L. Qian, *Nature Reviews Molecular Cell Biology*, 2021.
47. J. Mertens, J. R. Herdy, L. Traxler, S. T. Schafer, J. C. M. Schlachetzki, L. Böhnke, D. A. Reid, H. Lee, D. Zangwill, D. P. Fernandes, R. K. Agarwal, R. Lucciola, L. Zhou-Yang, L. Karbacher, F. Edenhofer, S. Stern, S. Horvath, A. C. M. Paquola, C. K. Glass, S. H. Yuan, M. Ku, A. Szücs, L. S. B. Goldstein, D. Galasko and F. H. Gage, *Cell Stem Cell*, 2021.
48. J. Drouin-Ouellet, K. Pircs, R. A. Barker, J. Jakobsson and M. Parmar, *Frontiers in Neuroscience*, 2017, **11**, 530.
49. S. Gascón, G. Masserdotti, G. L. Russo and M. Götz, *Cell Stem Cell*, 2017, **21**, 18-34.
50. N. N. Tran, I. G. Ladran and K. J. Brennand, *Schizophrenia bulletin*, 2013, **39**, 4-10.
51. C. Y. Luo, Q. Y. Lee, O. Wapinski, R. Castanon, J. R. Nery, M. Malin, M. S. Kareta, S. M. Cullen, M. A. Goodell, H. Y. Chang, M. Wernig and J. R. Ecker, *Elife*, 2019, **8**.

52. N. Yang, Yi, Zhiping, Thomas and M. Wernig, *Cell Stem Cell*, 2011, **9**, 517-525.
53. M. Schuldiner, R. Eiges, A. Eden, O. Yanuka, J. Itskovitz-Eldor, R. S. Goldstein and N. Benvenisty, *Brain Research*, 2001, **913**, 201-205.
54. S. M. Chambers, C. A. Fasano, E. P. Papapetrou, M. Tomishima, M. Sadelain and L. Studer, *Nature Biotechnology*, 2009, **27**, 275.
55. B.-Y. Hu and S.-C. Zhang, *Nature Protocols*, 2009, **4**, 1295.
56. K. K. B. Tan, W. W. M. Lim, C. Chai, M. Kukumberg, K. L. Lim, E. L. K. Goh and E. K. F. Yim, *Scientific Reports*, 2018, **8**, 9567.
57. S. Ankam, C. K. Lim and E. K. F. Yim, *Biomaterials*, 2015, **47**, 20-28.
58. N. Anh Tuan, R. S. Sharvari and K. F. Y. Evelyn, *Journal of Physics: Condensed Matter*, 2016, **28**, 183001.
59. S. Ankam, B. K. K. Teo, M. Kukumberg and E. K. F. Yim, *Organogenesis*, 2013, **9**, 128-142.
60. A. T. Nguyen, S. Mattiassi, M. Loeblein, E. Chin, D. Ma, P. Coquet, V. Viasnoff, E. H. T. Teo, E. L. Goh and E. K. F. Yim, *Biomedical Materials*, 2018, **13**, 034111.
61. S. Ankam, M. Suryana, L. Y. Chan, A. A. K. Moe, B. K. K. Teo, J. B. K. Law, M. P. Sheetz, H. Y. Low and E. K. F. Yim, *Acta Biomaterialia*, 2013, **9**, 4535-4545.
62. M. Marcus, K. Baranes, M. Park, I. S. Choi, K. Kang and O. Shefi, *Advanced Healthcare Materials*, 2017, **6**, 1700267.
63. B. K. K. Teo, S. T. Wong, C. K. Lim, T. Y. S. Kung, C. H. Yap, Y. Ramagopal, L. H. Romer and E. K. F. Yim, *Acs Nano*, 2013, **7**, 4785-4798.
64. B. K. K. Teo, S. Ankam, L. Y. Chan and E. K. F. Yim, in *Methods in Cell Biology*, ed. G. V. Shivashankar, Academic Press, 2010, vol. 98, pp. 241-294.
65. A. K. Yip, A. T. Nguyen, M. Rizwan, S. T. Wong, K.-H. Chiam and E. K. F. Yim, *Biomaterials*, 2018, **181**, 103-112.
66. S. T. Wong, S.-K. Teo, S. Park, K.-H. Chiam and E. K. F. Yim, *Biomechanics and Modeling in Mechanobiology*, 2014, **13**, 27-39.
67. A. T. Nguyen, S. R. Sathe and E. K. F. Yim, *Journal of Physics: Condensed Matter*, 2016, **28**, 183001.
68. A. A. K. Moe, M. Suryana, G. Marcy, S. K. Lim, S. Ankam, J. Z. W. Goh, J. Jin, B. K. K. Teo, J. B. K. Law, H. Y. Low, E. L. K. Goh, M. P. Sheetz and E. K. F. Yim, *Small*, 2012, **8**, 3050-3061.
69. L. Qi, N. Li, R. Huang, Q. Song, L. Wang, Q. Zhang, R. Su, T. Kong, M. Tang and G. Cheng, *PLoS One*, 2013, **8**, e59022.
70. E. K. F. Yim and M. P. Sheetz, *Stem Cell Research & Therapy*, 2012, **3**, 41.
71. H. Jeon, C. G. Simon Jr and G. Kim, *Journal of Biomedical Materials Research Part B: Applied Biomaterials*, 2014, **102**, 1580-1594.
72. J. J. Norman and T. A. Desai, *Annals of Biomedical Engineering*, 2006, **34**, 89-101.
73. A. Béduer, C. Vieu, F. Arnauduc, J.-C. Sol, I. Loubinoux and L. Vaysse, *Biomaterials*, 2012, **33**, 504-514.
74. J. B. Recknor, D. S. Sakaguchi and S. K. Mallapragada, *Biomaterials*, 2006, **27**, 4098-4108.
75. L. Y. Chan, W. R. Birch, E. K. F. Yim and A. B. H. Choo, *Biomaterials*, 2013, **34**, 382-392.
76. M. R. Lee, K. W. Kwon, H. Jung, H. N. Kim, K. Y. Suh, K. Kim and K.-S. Kim, *Biomaterials*, 2010, **31**, 4360-4366.
77. E. K. F. Yim, S. W. Pang and K. W. Leong, *Experimental Cell Research*, 2007, **313**, 1820-1829.
78. B. K. K. Teo, G.-D. S. Tan and E. K. F. Yim, *Tissue Engineering Part A*, 2014, **20**, 2151-2161.

79. K. K. B. Tan, J. Y. Tann, S. R. Sathe, S. H. Goh, D. Ma, E. L. K. Goh and E. K. F. Yim, *Biomaterials*, 2015, **43**, 32-43.
80. F. Pan, M. Zhang, G. Wu, Y. Lai, B. Greber, H. R. Schöler and L. Chi, *Biomaterials*, 2013, **34**, 8131-8139.
81. L. Song, K. Wang, Y. Li and Y. Yang, *Colloids and Surfaces B: Biointerfaces*, 2016, **148**, 49-58.
82. K. Yang, K. Jung, E. Ko, J. Kim, K. I. Park, J. Kim and S.-W. Cho, *ACS Applied Materials & Interfaces*, 2013, **5**, 10529-10540.
83. E. K. F. Yim, E. M. Darling, K. Kulangara, F. Guilak and K. W. Leong, *Biomaterials*, 2010, **31**, 1299-1306.
84. S. Ankam, B. K. K. Teo, G. Pohan, S. W. L. Ho, C. K. Lim and E. K. F. Yim, 2018, **6**.
85. Y. Zeng, S. T. Wong, S. K. Teo, K. W. Leong, K.-H. Chiam and E. K. F. Yim, *Scientific Reports*, 2018, **8**, 6444.
86. J. S. Chua, C.-P. Chng, A. A. K. Moe, J. Y. Tann, E. L. K. Goh, K.-H. Chiam and E. K. F. Yim, *Biomaterials*, 2014, **35**, 7750-7761.
87. D. Jhala and R. Vasita, *Polymer Reviews*, 2015, **55**, 561-595.
88. N. Sultana, Hassan, Mohd Izzat, Lim, Mim Mim, *Cham: Springer International Publishing*, 2015.
89. G. T. Christopherson, H. Song and H.-Q. Mao, *Biomaterials*, 2009, **30**, 556-564.
90. J. Xie, S. M. Willerth, X. Li, M. R. Macewan, A. Rader, S. E. Sakiyama-Elbert and Y. Xia, *Biomaterials*, 2009, **30**, 354-362.
91. X. Jiang, H. Q. Cao, L. Y. Shi, S. Y. Ng, L. W. Stanton and S. Y. Chew, *Acta Biomaterialia*, 2012, **8**, 1290-1302.
92. S. H. Lim, X. Y. Liu, H. Song, K. J. Yarema and H.-Q. Mao, *Biomaterials*, 2010, **31**, 9031-9039.
93. F. Yang, R. Murugan, S. Wang and S. Ramakrishna, *Biomaterials*, 2005, **26**, 2603-2610.
94. N. K. Mohtaram, J. Ko, C. King, L. Sun, N. Muller, M. B.-G. Jun and S. M. Willerth, *Journal of Biomedical Materials Research Part A*, 2015, **103**, 2591-2601.
95. N. Abbasi, S. M. Hashemi, M. Salehi, H. Jahani, S. J. Mowla, M. Soleimani and H. Hosseinkhani, *Journal of Biomedical Materials Research Part A*, 2016, **104**, 155-164.
96. L. C. Lins, F. Wianny, S. Livi, C. Dehay, J. Duchet-Rumeau and J.-F. Gérard, *Journal of Biomedical Materials Research Part B: Applied Biomaterials*, 2017, **105**, 2376-2393.
97. S. Bakhru, A. S. Nain, C. Highley, J. Wang, P. Campbell, C. Amon and S. Zappe, *Integrative Biology*, 2011, **3**, 1207-1214.
98. Y. I. Cho, J. S. Choi, S. Y. Jeong and H. S. Yoo, *Acta Biomaterialia*, 2010, **6**, 4725-4733.
99. J. Wang, R. Ye, Y. Wei, H. Wang, X. Xu, F. Zhang, J. Qu, B. Zuo and H. Zhang, *Journal of Biomedical Materials Research Part A*, 2012, **100A**, 632-645.
100. V. Mahairaki, S. H. Lim, G. T. Christopherson, L. Xu, I. Nasonkin, C. Yu, H.-Q. Mao and V. E. Koliatsos, *Tissue Engineering Part A*, 2010, **17**, 855-863.
101. K. Yang, H. Jung, H.-R. Lee, J. S. Lee, S. R. Kim, K. Y. Song, E. Cheong, J. Bang, S. G. Im and S.-W. Cho, *ACS Nano*, 2014, **8**, 7809-7822.
102. C. Yang, M. W. Tibbitt, L. Basta and K. S. Anseth, *Nature Materials*, 2014, **13**, 645.
103. R. Muhammad, G. S. L. Peh, K. Adnan, J. B. K. Law, J. S. Mehta and E. K. F. Yim, *Acta Biomaterialia*, 2015, **19**, 138-148.
104. S. Sathe, Q. X. Chan, J. Jin, E. Bernitt, H.-G. Döbereiner and K. E. Yim, *Journal of Functional Biomaterials*, 2017, **8**.
105. J. Wang, R. Ye, Y. Wei, H. Wang, X. Xu, F. Zhang, J. Qu, B. Zuo and H. Zhang, *J Biomed Mater Res A*, 2012, **100**, 632-645.
106. M. C. Murphy, D. T. Jones, C. R. Jack Jr, K. J. Glaser, M. L. Senjem, A. Manduca, J. P. Felmlee, R. E. Carter, R. L. Ehman and J. Huston Iii, *NeuroImage: Clinical*, 2016, **10**, 283-290.

107. J. Weickenmeier, R. de Rooij, S. Budday, P. Steinmann, T. C. Ovaert and E. Kuhl, *Acta biomaterialia*, 2016, **42**, 265-272.
108. N. D. Leipzig and M. S. Shoichet, *Biomaterials*, 2009, **30**, 6867-6878.
109. M. C. Murphy, J. Huston, III, C. R. Jack, Jr., K. J. Glaser, M. L. Senjem, J. Chen, A. Manduca, J. P. Felmlee and R. L. Ehman, *PLOS ONE*, 2013, **8**, e81668.
110. M. Iwashita, N. Kataoka, K. Toida and Y. Kosodo, *Development*, 2014, **141**, 3793-3798.
111. T. Takamura, U. Motosugi, Y. Sasaki, T. Kakegawa, K. Sato, K. J. Glaser, R. L. Ehman and H. Onishi, *J Magn Reson Imaging*, 2020, **51**, 727-733.
112. M. C. Murphy, J. Huston Iii, C. R. Jack Jr, K. J. Glaser, A. Manduca, J. P. Felmlee and R. L. Ehman, *Journal of Magnetic Resonance Imaging*, 2011, **34**, 494-498.
113. K. Saha, A. J. Keung, E. F. Irwin, Y. Li, L. Little, D. V. Schaffer and K. E. Healy, *Biophys J*, 2008, **95**, 4426-4438.
114. J. M. Stukel and R. K. Willits, *Tissue Eng Part B Rev*, 2016, **22**, 173-182.
115. A. Banerjee, M. Arha, S. Choudhary, R. S. Ashton, S. R. Bhatia, D. V. Schaffer and R. S. Kane, *Biomaterials*, 2009, **30**, 4695-4699.
116. S. Ali, I. B. Wall, C. Mason, A. E. Pelling and F. S. Veraitch, *Acta Biomaterialia*, 2015, **25**, 253-267.
117. G. J. Her, H.-C. Wu, M.-H. Chen, M.-Y. Chen, S.-C. Chang and T.-W. Wang, *Acta Biomaterialia*, 2013, **9**, 5170-5180.
118. A. I. Teixeira, S. Ilkhanizadeh, J. A. Wigenius, J. K. Duckworth, O. Inganäs and O. Hermanson, *Biomaterials*, 2009, **30**, 4567-4572.
119. A. J. Keung, E. M. de Juan-Pardo, D. V. Schaffer and S. Kumar, *STEM CELLS*, 2011, **29**, 1886-1897.
120. J. L. Hoon, M. H. Tan and C.-G. Koh, *Cells*, 2016, **5**.
121. N. Huebsch, P. R. Arany, A. S. Mao, D. Shvartsman, O. A. Ali, S. A. Bencherif, J. Rivera-Feliciano and D. J. Mooney, *Nat Mater*, 2010, **9**, 518-526.
122. M. L. Previtera, C. G. Langhammer, N. A. Langrana and B. L. Firestein, *Annals of biomedical engineering*, 2010, **38**, 3733-3743.
123. Y. Sun, K. M. A. Yong, L. G. Villa-Diaz, X. Zhang, W. Chen, R. Philson, S. Weng, H. Xu, P. H. Krebsbach and J. Fu, *Nature Materials*, 2014, **13**, 599-604.
124. M. Yasodharababu and A. K. Nair, *Cellular and Molecular Bioengineering*, 2020, **13**, 229-245.
125. D. Srivastava and N. DeWitt, *Cell*, 2016, **166**, 1386-1396.
126. A. McCaughey-Chapman and B. Connor, *Stem cells and development*, 2018, **27**, 1674-1692.
127. C. E. Ang and M. Wernig, *Journal of Comparative Neurology*, 2014, **522**, 2877-2886.
128. J. Long, H. Kim, D. Kim, J. B. Lee and D.-H. Kim, *Journal of Materials Chemistry B*, 2017, **5**, 2375-2389.
129. J. Fang, Y.-Y. Hsueh, J. Soto, W. Sun, J. Wang, Z. Gu, A. Khademhosseini and S. Li, *ACS nano*, 2020, **14**, 1296-1318.
130. D. Gallego-Perez, J. J. Otero, C. Czeisler, J. Ma, C. Ortiz, P. Gygli, F. P. Catacutan, H. N. Gokozan, A. Cowgill, T. Sherwood, S. Ghatak, V. Malkoc, X. Zhao, W.-C. Liao, S. Gnyawali, X. Wang, A. F. Adler, K. Leong, B. Wulff, T. A. Wilgus, C. Askwith, S. Khanna, C. Rink, C. K. Sen and L. J. Lee, *Nanomedicine: Nanotechnology, Biology and Medicine*, 2016, **12**, 399-409.
131. A. F. Adler, C. L. Grigsby, K. Kulangara, H. Wang, R. Yasuda and K. W. Leong, *Molecular therapy. Nucleic acids*, 2012, **1**, e32-e32.
132. C. Lin, Z. Zhong, M. C. Lok, X. Jiang, W. E. Hennink, J. Feijen and J. F. J. Engbersen, *Bioconjugate Chemistry*, 2007, **18**, 138-145.
133. R. H. Liou, T. L. Edwards, K. R. Martin and R. C. Wong, *International Journal of Molecular Sciences*, 2020, **21**.

134. D. Jain, S. Mattiassi, E. L. Goh and E. K. F. Yim, *Neural regeneration research*, 2020, **15**, 573-585.
135. S. Ding, P. Kingshott, H. Thissen, M. Pera and P. Y. Wang, *Biotechnol Bioeng*, 2017, **114**, 260-280.
136. H. K. Kim, E. Kim, H. Jang, Y.-K. Kim and K. Kang, *ChemNanoMat*, 2017, **3**, 278-287.
137. C. Simitzi, K. Karali, A. Ranella and E. Stratakis, *Chemphyschem*, 2018, **19**, 1143-1163.
138. M. Poudineh, Z. Wang, M. Labib, M. Ahmadi, L. Zhang, J. Das, S. Ahmed, S. Angers and S. O. Kelley, *Nano Lett*, 2018, **18**, 7188-7193.
139. B. S. Eftekhari, M. Eskandari, P. A. Janmey, A. Samadikuchaksaraei and M. Gholipourmalekabadi, *Advanced Functional Materials*, 2020, **30**, 1907792.
140. R. L. Youngblood, N. F. Truong, T. Segura and L. D. Shea, *Molecular Therapy*, 2018, **26**, 2087-2106.
141. R. K. Singh, J. C. Knowles and H.-W. Kim, *Journal of tissue engineering*, 2019, **10**, 2041731419877528.
142. L. Larsson, S. P. Pilipchuk, W. V. Giannobile and R. M. Castilho, *Journal of Biomedical Materials Research Part B: Applied Biomaterials*, 2018, **106**, 2065-2071.
143. K. Kulangara, A. F. Adler, H. Wang, M. Chellappan, E. Hammett, R. Yasuda and K. W. Leong, *Biomaterials*, 2014, **35**, 5327-5336.
144. C. Lin, Z. Zhong, M. C. Lok, X. Jiang, W. E. Hennink, J. Feijen and J. F. Engbersen, *Bioconjug Chem*, 2007, **18**, 138-145.
145. A. A. Moe, M. Suryana, G. Marcy, S. K. Lim, S. Ankam, J. Z. Goh, J. Jin, B. K. Teo, J. B. Law, H. Y. Low, E. L. Goh, M. P. Sheetz and E. K. Yim, *Small*, 2012, **8**, 3050-3061.
146. S. Ankam, M. Suryana, L. Y. Chan, A. A. Moe, B. K. Teo, J. B. Law, M. P. Sheetz, H. Y. Low and E. K. Yim, *Acta Biomater*, 2013, **9**, 4535-4545.
147. A. Torres-Espín, D. Santos, F. González-Pérez, J. del Valle and X. Navarro, *J Neurosci Methods*, 2014, **236**, 26-39.
148. A. Caceres, G. Banker and L. Binder, *The Journal of Neuroscience*, 1986, **6**, 714-722.
149. S. Ankam, C. K. Lim and E. K. Yim, *Biomaterials*, 2015, **47**, 20-28.
150. S. Ankam, B. K. K. Teo, G. Pohan, S. W. L. Ho, C. K. Lim and E. K. F. Yim, *Frontiers in Bioengineering and Biotechnology*, 2018, **6**.
151. K. Wang, A. Bruce, R. Mezan, A. Kadiyala, L. Wang, J. Dawson, Y. Rojanasakul and Y. Yang, *ACS Applied Materials & Interfaces*, 2016, **8**, 5082-5092.
152. K. Yang, K. Jung, E. Ko, J. Kim, K. I. Park, J. Kim and S. W. Cho, *ACS Appl Mater Interfaces*, 2013, **5**, 10529-10540.
153. K. K. B. Tan, W. W. M. Lim, C. Chai, M. Kukumberg, K. L. Lim, E. L. K. Goh and E. K. F. Yim, *Sci Rep*, 2018, **8**, 9567.
154. J. S. Chua, C. P. Chng, A. A. Moe, J. Y. Tann, E. L. Goh, K. H. Chiam and E. K. Yim, *Biomaterials*, 2014, **35**, 7750-7761.
155. L. Yang, K. M. Jurczak, L. Ge and P. Rijn, *Advanced Healthcare Materials*, 2020, **9**, 2000117.
156. J. J. Norman and T. A. Desai, *Ann Biomed Eng*, 2006, **34**, 89-101.
157. H. Jeon, C. G. Simon, Jr. and G. Kim, *J Biomed Mater Res B Appl Biomater*, 2014, **102**, 1580-1594.
158. K. T. M. Tran and T. D. Nguyen, *Journal of Science: Advanced Materials and Devices*, 2017, **2**, 1-14.
159. M. Rizwan, G. S. L. Peh, H.-P. Ang, N. C. Lwin, K. Adnan, J. S. Mehta, W. S. Tan and E. K. F. Yim, *Biomaterials*, 2017, **120**, 139-154.
160. D. Hoffman-Kim, J. A. Mitchel and R. V. Bellamkonda, *Annu Rev Biomed Eng*, 2010, **12**, 203-231.

161. J. I. Kim, C. S. Kim and C. H. Park, in *Cutting-Edge Enabling Technologies for Regenerative Medicine*, eds. H. J. Chun, C. H. Park, I. K. Kwon and G. Khang, Springer Singapore, Singapore, 2018, pp. 395-408.
162. S. Vijayavenkataraman, *Acta Biomaterialia*, 2020, **106**, 54-69.
163. J. Eyckmans, T. Boudou, X. Yu and S. Chen, Christopher, *Developmental Cell*, 2011, **21**, 35-47.
164. Y. Zhang, *Multi-scale Extracellular Matrix Mechanics and Mechanobiology*, Springer, 2020.
165. C. R. Jacobs, H. Huang and R. Y. Kwon, *Introduction to cell mechanics and mechanobiology*, Garland Science, 2012.
166. C. F. Guimarães, L. Gasperini, A. P. Marques and R. L. Reis, *Nature Reviews Materials*, 2020, **5**, 351-370.
167. Y. Li, Y. Xiao and C. Liu, *Chemical Reviews*, 2017, **117**, 4376-4421.
168. S. Kim, M. Uroz, J. L. Bays and C. S. Chen, *Developmental Cell*, 2021, **56**, 180-191.
169. F. Guilak, D. L. Butler, S. A. Goldstein and F. P. T. Baaijens, *Journal of Biomechanics*, 2014, **47**, 1933-1940.
170. D. P. Byrne, D. Lacroix, J. A. Planell, D. J. Kelly and P. J. Prendergast, *Biomaterials*, 2007, **28**, 5544-5554.
171. F. D. Benedetto, A. Biasco, D. Pisignano and R. Cingolani, *Nanotechnology*, 2005, **16**, S165-S170.
172. J. Qu, X. Hou, W. Fan, G. Xi, H. Diao and X. Liu, *Scientific Reports*, 2015, **5**, 17872.
173. J. Moeller, A. K. Denisin, J. Y. Sim, R. E. Wilson, A. J. S. Ribeiro and B. L. Pruitt, *PLOS ONE*, 2018, **13**, e0189901.
174. A. Díaz Lantada, N. Mazarío Picazo, M. Guttmann, M. Wissmann, M. Schneider, M. Worgull, S. Hengsbach, F. Rupp, K. Bade and G. R. Plaza, *Materials*, 2020, **13**, 1586.
175. A. K. Yip, A. T. Nguyen, M. Rizwan, S. T. Wong, K.-H. Chiam and E. K. Yim, *Biomaterials*, 2018, **181**, 103-112.
176. A. K. Denisin and B. L. Pruitt, *ACS applied materials & interfaces*, 2016, **8**, 21893-21902.
177. R. S. Fischer, K. A. Myers, M. L. Gardel and C. M. Waterman, *Nature protocols*, 2012, **7**, 2056-2066.
178. S. Syed, A. Karadaghy and S. Zustiak, *Journal of visualized experiments: JoVE*, 2015.
179. B. Díaz-Bello, A. X. Monroy-Romero, D. Pérez-Calixto, D. Zamarrón-Hernández, N. Serna-Marquez, G. Vázquez-Victorio and M. Hautefeuille, *ACS Biomaterials Science & Engineering*, 2019, **5**, 4219-4227.
180. A. K. Yip, K. Iwasaki, C. Ursekar, H. Machiyama, M. Saxena, H. Chen, I. Harada, K.-H. Chiam and Y. Sawada, *Biophysical journal*, 2013, **104**, 19-29.
181. A. Farrukh, J. I. Paez, M. Salierno, W. Fan, B. Berninger and A. Del Campo, *Biomacromolecules*, 2017, **18**, 906-913.
182. M. J. Poellmann and A. J. Wagoner Johnson, *Cellular and Molecular Bioengineering*, 2013, **6**, 299-309.
183. C. A. Reinhart-King, M. Dembo and D. A. Hammer, *Langmuir*, 2003, **19**, 1573-1579.
184. J. P. Califano and C. A. Reinhart-King, *Cellular and Molecular Bioengineering*, 2008, **1**, 122-132.
185. J. B. Leach, X. Q. Brown, J. G. Jacot, P. A. Dimilla and J. Y. Wong, *Journal of Neural Engineering*, 2007, **4**, 26-34.
186. J. Lantoine, T. Grevesse, A. Villers, G. Delhaye, C. Mestdagh, M. Versaevel, D. Mohammed, C. Bruyère, L. Alaimo, S. P. Lacour, L. Ris and S. Gabriele, *Biomaterials*, 2016, **89**, 14-24.
187. D. D. Pless, Y. C. Lee, S. Roseman and R. L. Schnaar, *Journal of Biological Chemistry*, 1983, **258**, 2340-2349.

188. D. Poburko, *Journal*, 2020.
189. M. Shivaraj, G. Marcy, G. Low, J. Ryu, X. Zhao, F. Rosales and E. Goh, *PloS one*, 2012, **7**, e42935.
190. G. Sitterley, S. Karmiol, E. Manaster and J. Ryn, *Biofiles (Sigma-Aldrich)*, 2008, **3**, 1-28.
191. D. Li and Y.-l. Wang, in *Principles of Tissue Engineering (Fifth Edition)*, eds. R. Lanza, R. Langer, J. P. Vacanti and A. Atala, Academic Press, 2020, pp. 237-256.
192. C. E. Kandow, P. C. Georges, P. A. Janmey and K. A. Beningo, in *Methods in Cell Biology*, Academic Press, 2007, vol. 83, pp. 29-46.
193. Y.-L. Wang and R. J. Pelham Jr, *Methods in enzymology*, 1998, **298**, 489-496.
194. S. Sen, A. J. Engler and D. E. Discher, *Cellular and Molecular Bioengineering*, 2009, **2**, 39-48.
195. A. Buxboim, K. Rajagopal, A. E. X. Brown and D. E. Discher, *Journal of physics. Condensed matter : an Institute of Physics journal*, 2010, **22**, 194116-194116.
196. A. K. Yip, K.-H. Chiam and P. Matsudaira, *Integrative Biology*, 2015, **7**, 1196-1211.
197. A. Domogatskaya, S. Rodin, A. Boutaud and K. Tryggvason, *Stem cells*, 2008, **26**, 2800-2809.
198. S. Rodin, A. Domogatskaya, S. Ström, E. M. Hansson, K. R. Chien, J. Inzunza, O. Hovatta and K. Tryggvason, *Nature biotechnology*, 2010, **28**, 611.
199. C. Chang, H. L. Goel, H. Gao, B. Pursell, L. D. Shultz, D. L. Greiner, S. Ingerpuu, M. Patarroyo, S. Cao and E. Lim, *Genes & development*, 2015, **29**, 1-6.
200. S. Shibata, R. Hayashi, T. Okubo, Y. Kudo, T. Katayama, Y. Ishikawa, J. Toga, E. Yagi, Y. Honma and A. J. Quantock, *Cell reports*, 2018, **25**, 1668-1679. e1665.
201. J. Graf, Y. Iwamoto, M. Sasaki, G. R. Martin, H. K. Kleinman, F. A. Robey and Y. Yamada, *Cell*, 1987, **48**, 989-996.
202. B. F. Liu, J. Ma, Q. Y. Xu and F. Z. Cui, *Colloids and Surfaces B: Biointerfaces*, 2006, **53**, 175-178.
203. E. Ramsay, J. Hadgraft, J. Birchall and M. Gumbleton, *International Journal of Pharmaceutics*, 2000, **210**, 97-107.
204. G. Blauer and Z. B. Alfassi, *Biochimica et Biophysica Acta (BBA) - Protein Structure*, 1967, **133**, 206-218.
205. X. Xu and Y. Dai, *Journal of cellular and molecular medicine*, 2010, **14**, 175-180.
206. D. Edgar, R. Timpl and H. Thoenen, *The EMBO journal*, 1984, **3**, 1463-1468.
207. Y. Ikegami and H. Ijima, *Journal of Bioscience and Bioengineering*, 2020, **129**, 354-362.
208. R. Linhardt, S. Murugesan and J. Xie, *Current Topics in Medicinal Chemistry*, 2008, **8**, 80-100.
209. Y. Ding, M. Yang, Z. Yang, R. Luo, X. Lu, N. Huang, P. Huang and Y. Leng, *Acta Biomaterialia*, 2015, **15**, 150-163.
210. X. H. Wang, D. P. Li, W. J. Wang, Q. L. Feng, F. Z. Cui, Y. X. Xu and X. H. Song, *International Journal of Biological Macromolecules*, 2003, **33**, 95-100.
211. S. P. Massia and J. A. Hubbell, *Journal of Biological Chemistry*, 1992, **267**, 10133-10141.
212. U. Sung, J. J. O'Rear and P. D. Yurchenco, *European Journal of Biochemistry*, 1997, **250**, 138-143.
213. K. Watanabe, M. Ueno, D. Kamiya, A. Nishiyama, M. Matsumura, T. Wataya, J. B. Takahashi, S. Nishikawa, S.-I. Nishikawa, K. Muguruma and Y. Sasai, *Nature Biotechnology*, 2007, **25**, 681-686.
214. H. Kurosawa, *Journal of Bioscience and Bioengineering*, 2012, **114**, 577-581.
215. R. Rungsiwiwut, C. Manolertthewan, P. Numchaisrika, V. Ahnonkitpanit, P. Virutamasen, M. Techakumphu and K. Pruksananonda, *Cells Tissues Organs*, 2013, **198**, 127-138.
216. T. Ishizaki, M. Uehata, I. Tamechika, J. Keel, K. Nonomura, M. Maekawa and S. Narumiya, *Molecular pharmacology*, 2000, **57**, 976-983.

217. N. Anh Tuan, S. R. Sathe and E. K. F. Yim, *Journal of Physics-Condensed Matter*, 2016, **28**.
218. C. J. Bettinger, R. Langer and J. T. Borenstein, *Angewandte Chemie International Edition*, 2009, **48**, 5406-5415.
219. G. T. Christopherson, H. Song and H. Q. Mao, *Biomaterials*, 2009, **30**, 556-564.
220. X. Cun and L. Hosta-Rigau, *Nanomaterials (Basel)*, 2020, **10**.
221. F. Pan, M. Zhang, G. Wu, Y. Lai, B. Greber, H. R. Schoeler and L. Chi, *Biomaterials*, 2013, **34**, 8131-8139.
222. L. Qi, N. Li, R. Huang, Q. Song, L. Wang, Q. Zhang, R. Su, T. Kong, M. Tang and G. Cheng, *Plos One*, 2013, **8**.
223. C. Simitzi, A. Ranella and E. Stratakis, *Acta Biomaterialia*, 2017, **51**, 21-52.
224. K. K. B. Tan, W. W. M. Lim, C. Chai, M. Kukumberg, K. L. Lim, E. L. K. Goh and E. K. F. Yim, *Scientific Reports*, 2018, **8**.
225. A. R. Nectow, K. G. Marra and D. L. Kaplan, *Tissue Engineering Part B: Reviews*, 2011, **18**, 40-50.
226. E. C. Spivey, Z. Z. Khaing, J. B. Shear and C. E. Schmidt, *Biomaterials*, 2012, **33**, 4264-4276.
227. T. A. Valente, D. M. Silva, P. S. Gomes, M. H. Fernandes, J. D. Santos and V. Sencadas, *ACS Appl Mater Interfaces*, 2016, **8**, 3241-3249.
228. F. Yang, R. Murugan, S. Wang and S. Ramakrishna, *Biomaterials*, 2005, **26**, 2603-2610.
229. D. R. Zimmermann and M. T. Dours-Zimmermann, *Histochemistry and Cell Biology*, 2008, **130**, 635-653.
230. E. K. F. Yim and M. P. Sheetz, *Stem Cell Research & Therapy*, 2012, **3**.
231. P. C. Georges, W. J. Miller, D. F. Meaney, E. S. Sawyer and P. A. Janmey, *Biophysical Journal*, 2006, **90**, 3012-3018.
232. G. Zhu, M. F. Mehler, P. C. Mabie and J. A. Kessler, *Journal of Neuroscience Research*, 2000, **59**, 312-320.
233. W. Chen, S. Han, W. Qian, S. Weng, H. Yang, Y. Sun, L. G. Villa-Diaz, P. H. Krebsbach and J. Fu, *Nanoscale*, 2018, **10**, 3556-3565.
234. E. Migliorini, G. Grenci, J. Ban, A. Pozzato, M. Tormen, M. Lazzarino, V. Torre and M. E. Ruaro, *Biotechnol Bioeng*, 2011, **108**, 2736-2746.
235. L. Song, K. Wang, Y. Li and Y. Yang, *Colloids Surf B Biointerfaces*, 2016, **148**, 49-58.
236. F. Pan, M. Zhang, G. Wu, Y. Lai, B. Greber, H. R. Scholer and L. Chi, *Biomaterials*, 2013, **34**, 8131-8139.
237. K. K. Tan, J. Y. Tann, S. R. Sathe, S. H. Goh, D. Ma, E. L. Goh and E. K. Yim, *Biomaterials*, 2015, **43**, 32-43.
238. J. Baek, S.-Y. Cho, H. Kang, H. Ahn, W.-B. Jung, Y. Cho, E. Lee, S.-W. Cho, H.-T. Jung and S. G. Im, *ACS Applied Materials & Interfaces*, 2018, **10**, 33891-33900.
239. J. B. Recknor, D. S. Sakaguchi and S. K. Mallapragada, *Biomaterials*, 2006, **27**, 4098-4108.